UNIVERSITY OF LEEDS

The Hydrodynamic stripping of spheroids and disks

Jacob Louis Close

School of Physics and Astronomy

University of Leeds

Submitted in accordance with
the requirements for the degree of

Doctor of Philosophy

September 2016

The candidate confirms that the work submitted is his own, except where work which has formed part of jointly authored publications has been included. The contribution of the candidate and the other authors of this work has been explicitly indicated. The candidate confirms that appropriate credit has been given within this thesis where reference has been made to the work of others.

Preface

With this thesis, some of the chapters contain work presented in the jointly authored publications:

I "Ram pressure stripping of the hot gaseous haloes of galaxies using the k-ϵ sub-grid turbulence model" – **J. L. Close**, J. M. Pittard, T. W. Hartquist, S. A. E. G. Falle, 2013, MNRAS, 436, 3021.

II "Hydrodynamic ablation of protoplanetary disks via supernovae" – **J. L. Close**, J. M. Pittard, MNRAS, submitted

Paper I forms the basis of Chapter 3. Paper II forms the basis of Chapter 5. In both papers the hydrodynamical code used to perform the simulations was written originally by S.A.E.G. Falle. The primary author (J. L. Close) is responsible for the initial conditions, running of the simulation and the analysis of the results. The primary author wrote the first draft of the publication after which comments from the co-authors were incorporated for the final draft. The simulations presented in Chapter 4 uses the same hydrodynamical code.

Acknowledgements

First I would like to thank my supervisor, Julian Pittard, for his guidance, encouragement and constant optimism. Thanks are also due to Tom Hartquist, for his sagely advice, and Sam Falle for his code.

My time during my PhD was greatly enriched by my fellow PhD students, and for that I owe much thanks. In particular, Harry Steggles for constantly pushing me to learn more about coding, Karim Ababakr for being a constant source of entertainment, and John Fairlamb for forcing me to enjoy life, especially during the last few months of my PhD.

Finally, I am eternally grateful for my parents' unwavering support, not only during my PhD but throughout my life, and also for supplying me with mixed bhajis.

Thank you all.

Abstract

This thesis presents numerical simulations of the ablation of galaxies and stellar disks. A sub-grid turbulence model is used to improve the accuracy of the results. Firstly simulations of galactic ram pressure stripping are presented. A spherically symmetric galactic halo is subjected to a wind of a number of different Mach numbers, both with and without the turbulence model. The initial, instantaneous stripping is unaffected by the use of the turbulence model. The turbulence model leads to significantly greater levels of long term ablation, which is more consistent with what simple analytic calculations indicate, showing that the continual Kelvin-Helmholtz stripping plays a significant role in the ram pressure stripping and this is hidden by the finite resolution of simulations without turbulence models.

Secondly the turbulence model is applied to galactic disk simulations. In high Mach number (~ 15) rotating disks the turbulence generated from the internal stresses in the disk causes it to become unstable and erroneously expand in the z direction. This is not the case for lower Mach number disks, such as dwarf disk galaxies. Further developments are needed in turbulence modelling if disk galaxies are to be simulated in this way.

Finally inviscid simulations of the interaction of a supernova remnant on a stellar disk are presented. The supernova remnant is simulated hydrodynamically as opposed to using analytical approximations which represents an improvement on previous models. A number of inclination angles of the disk are considered which is not possible with previous two dimensional simulations. Mass loss rates are calculated and compared to other competing processes. Similarly to disk galaxies, the inclination angle only has a large effect on the evolution when the disk is close to edge on. Edge on disks develop an asymmetry when the ablation period is less than the rotation period of the disk. Contamination of the disk with supernova material is also investigate and is found to be low (about one part in $200,000$ in the highest case), consistent with previous results.

Abbreviations

AMR	Adaptive Mesh Refinement
CTU	Corner Transport Upwind
HLL	Harten-Lax-van Leer
HLLC	HLL with Contact discontinuity
HLLE	HLL with Einfeld fix
ICM	Intracluster Medium
ISM	Interstellar Medium
LimO3	3rd Order Limiter
LLF	Local Lax-Friedrichs
MH	MUSCL-Hancock
MTL	Maximum Turbulence Lengthscale
MUSCL	Monotone Upstream-Centred Scheme for Conservation Laws
PC	Predictor-Corrector
PCM	Piecewise Constant Method
PLM	Piecewise Linear Method
PPM	Piecewise Parabolic Method
RK2/3	Runge-Kutta 2nd/3rd Order
SDSS	Sloan Digital Sky Survey
SFR	Star Formation Rate
SLR	Short-Lived Radionuclides
SNR	Supernova remnant

SPH	Smooth Particle Hydrodynamics
TVDLF	Total Variation Diminishing Lax-Friedrichs
WENO3/5	Weighted Essentially Non-Oscillatory 3rd/5th Order
WR	Wolf-Rayet

Contents

List of Figures

LIST OF FIGURES

LIST OF FIGURES

List of Tables

LIST OF TABLES

Chapter 1

Introduction

The evolution of almost all astrophysical objects is influenced in some way by the environment in which it lives. Objects that are otherwise identical can follow very different evolutionary paths depending on how it interacts with the medium around it and so it is important to understand these interactions in order to create a full picture of the evolution of the object itself. Many objects (e.g. molecular clouds, filaments, circumstellar disks, galaxies) are comprised largely of gas or have gas as a significant component and are thus susceptible to erosion/ablation from the relative motion between them and their surrounding medium. Relative motion can arise from movement of the object though the medium or due to the presence of strong shocks and winds which are driven though the medium (e.g. jets, stellar winds and supernovae).

This chapter outlines some examples of ablation in astrophysics, and forms the background to this thesis. In Section 1.1 observational evidence for the ram pressure stripping of gas from galaxies is noted as well as numerical simulations of the process. Section 1.2 notes the processes by which protoplanetary disks are

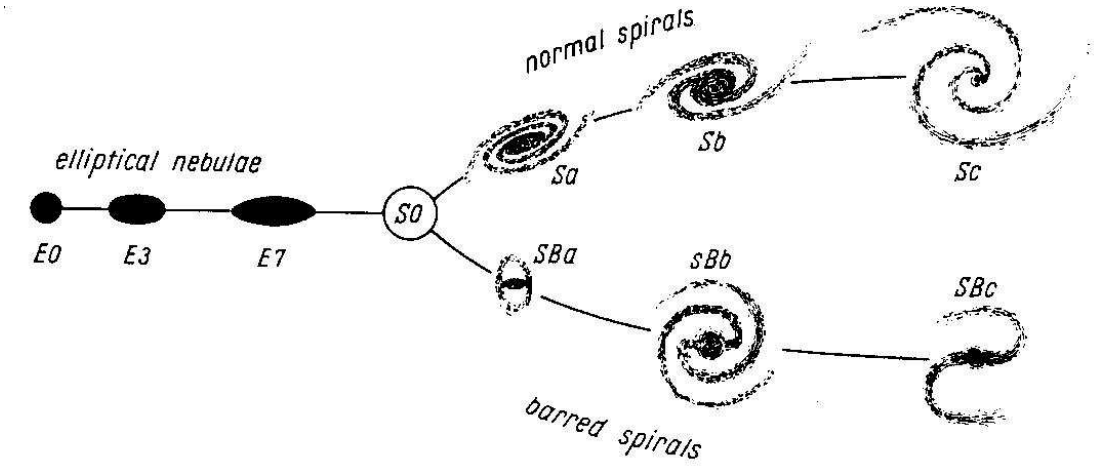

Figure 1.1: The original Hubble sequence of galaxies (from Hubble (1936)).

dispersed and how external factors, such as stellar winds and supernova remnants (SNRs) can play a role.

1.1 Galactic Ram Pressure Stripping

1.1.1 Galaxy Morphology

Galaxies can be classified into a surprisingly small number of types. First introduced by Hubble (1926), galaxies can be classified into ellipticals, spirals and irregulars simply by shape. Hubble (1926) also introduced the concept of "early", "intermediate" and "late" types, referring not to their chronology but outlining a sequence of increasing complexity. This system has since been extended (de Vaucouleurs 1959) to include spirals beyond Sc.

As the body of knowledge grew it became apparent that these galaxy types are distinguished by more than just morphology. Ellipticals are typically redder (Holmberg 1958), and have less gas (Haynes *et al.* 1984) and lower rates of star

formation (Blanton *et al.* 2003; Lee *et al.* 2013) than spiral galaxies. This paints the picture that they really are distinct species. The fact that they can be put into a clear sequence suggests galaxies may evolve along the sequence (Roberts & Haynes 1994).

1.1.2 Density - Morphology Relation

Galaxies reside in a wide range of environments, from small groups to large clusters (such as the Virgo cluster, which contains the Milky Way), or even in relative isolation. These environments effect the orbital speeds of the galaxies, the properties of the intracluster medium (ICM) and the frequency of interactions between galaxies.

It has been observed that there exists a relationship between galaxy type and local galaxy density (Melnick & Sargent 1977; Dressler 1980). Goto *et al.* (2003) use a sample of galaxies from the Sloan Digital Sky Survey (SDSS). By classifying the galaxies into one of four types, it can be seen (as shown in Figure 1.2) that the number of "Late Disc" galaxies drops off and the number of "Early-type" galaxies increases as the local galaxy density increases. In other words, galaxies that are more strongly clustered are less likely to be late-type galaxies than weakly clustered or isolated galaxies. Another analysis of the SDSS by Gómez *et al.* (2003) correlates star formation rate (SFR) with galaxy density, showing strongly clustered galaxies have reduced rates of star formation (see Figure 1.3). These observational results strongly suggest that a cluster environment shapes the evolution of the galaxies within it.

One possible way to explain the morphology-density relation is ram pressure

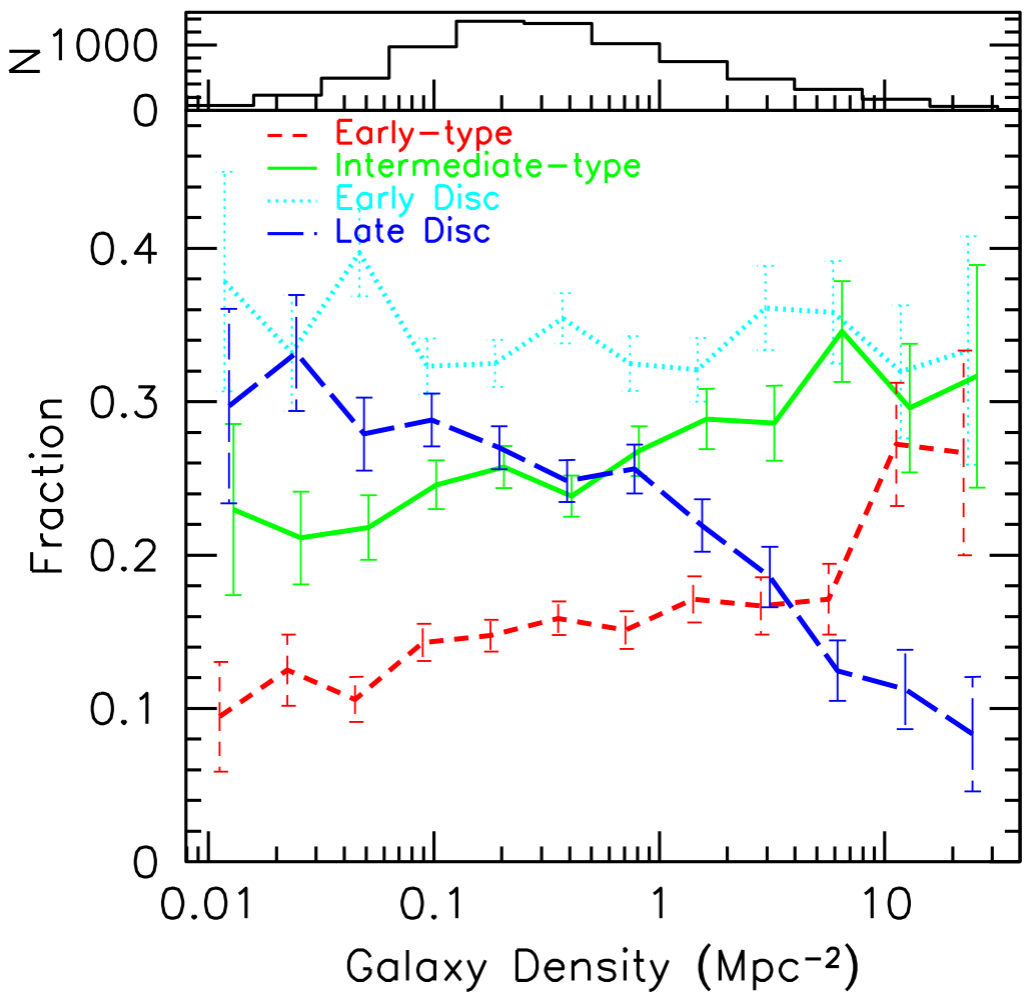

Figure 1.2: Galaxy type fraction as a function of local galaxy density. The upper panel shows the number of galaxies in each bin of galaxy density. (Figure from Goto *et al.* (2003).)

stripping. This was first explored analytically for a disk shaped gas distribution by Gunn & Gott (1972). As a galaxy orbits within a cluster it moves though the inter-cluster medium (ICM) which exerts a ram pressure on the gas in the galaxy. Ram pressure stripping can be separated into two distinct processes: instantaneous stripping and Kelvin-Helmholtz stripping. The instantaneous stripping occurs when the ram pressure is higher than the gravitational force per area on

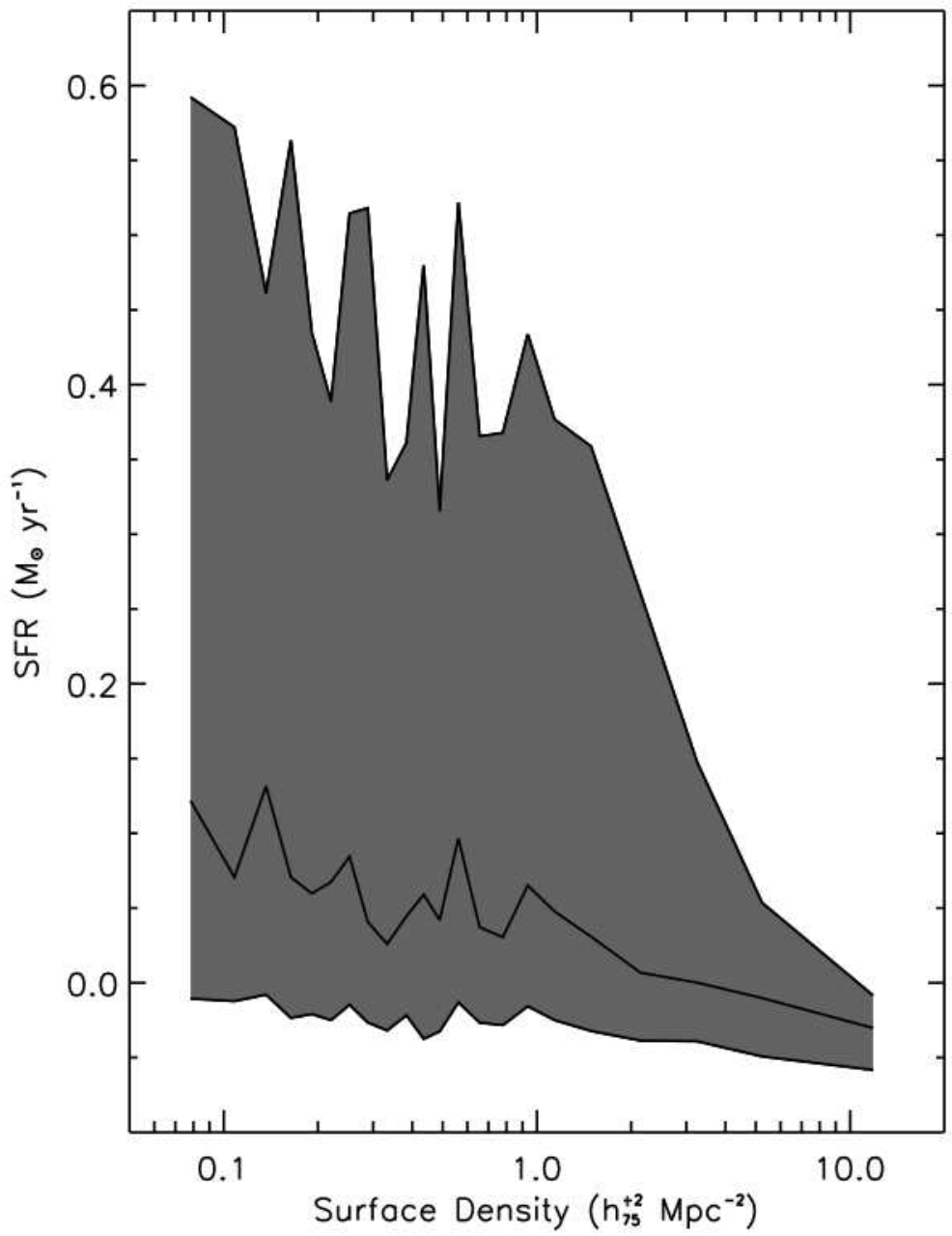

Figure 1.3: Star formation rate (SFR) as a function of local galactic surface density. The grey area shows the 25th-75th percentile of galaxies, with the median shown as a black line. (Figure from Gómez *et al.* (2003).)

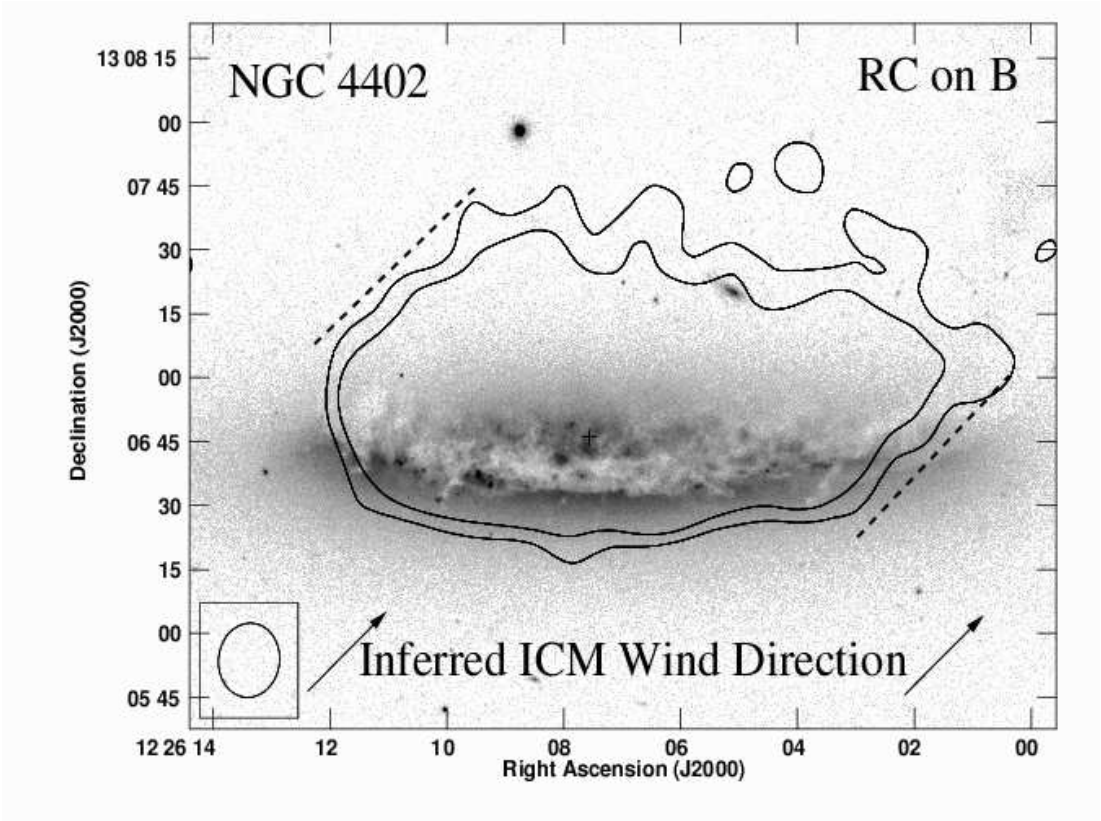

Figure 1.4: Observational evidence of ram pressure stripping in NGC 4402. Radio continuum contours show the tail structure over a B band image. (Figure from Crowl *et al.* (2005).)

a column of gas and occurs on short time-scales (less than 1 Gyr in most cases). Kelvin-Helmholtz stripping is due to the shear force created as the ICM flows past the edge of the galaxy. This induces the Kelvin-Helmholtz instability and allows material to be continually stripped from the galaxy and occurs on longer time scales. Ram pressure stripping has led to observable tails in a number of galaxies in the Virgo cluster (Crowl *et al.* 2005; Abramson *et al.* 2011) and is also visible as X-ray wakes and bow shocks. Figures 1.4 and 1.5 show the observable effect of ram pressure stripping in galaxy NGC 4402.

A number of studies have been done to try to quantify different aspects of this

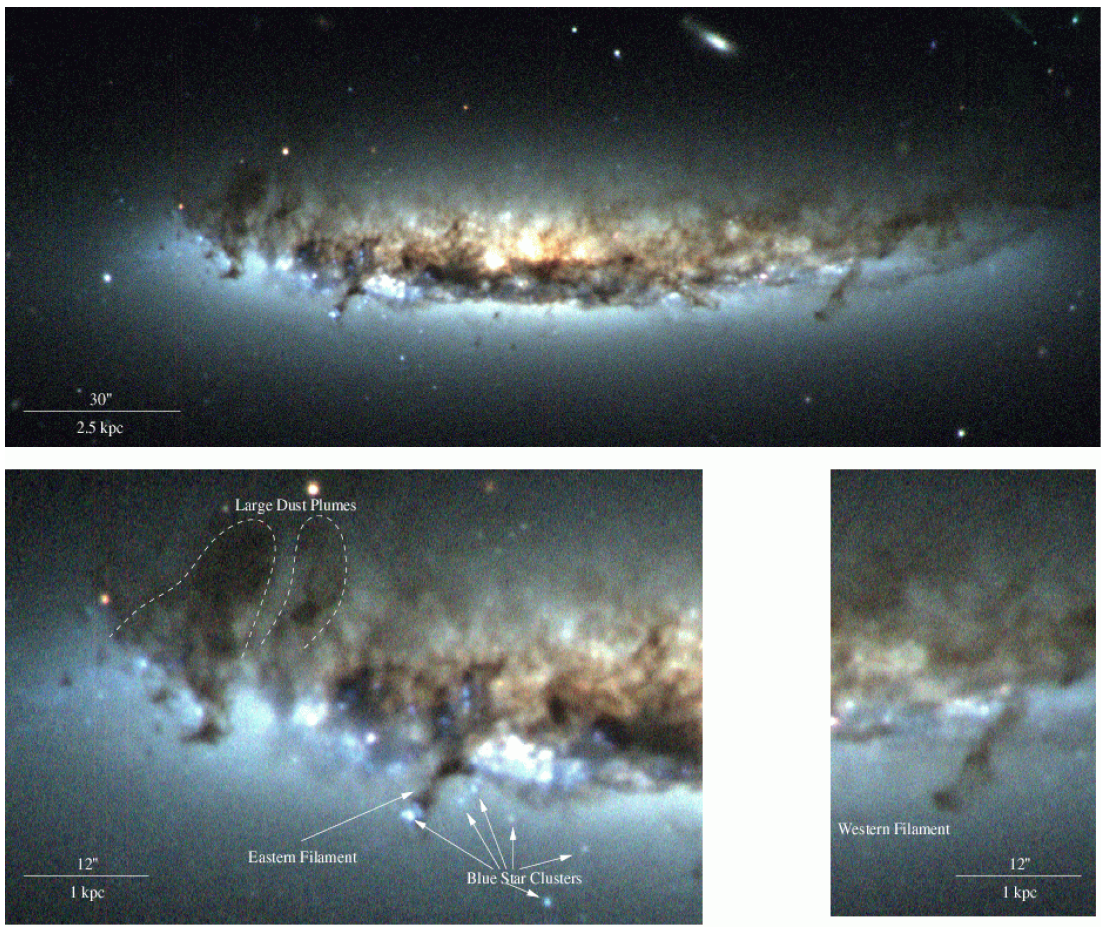

Figure 1.5: Observational evidence of ram pressure stripping in NGC 4402. BVR colour image. Many features associated with ram pressure can be seen, such as the bow shape, dust plumes and exposed star clusters. (Figure from Crowl *et al.* (2005).)

effect. In general, the effect of ram pressure stripping is simulated in two ways. Firstly one can perform a "wind tunnel" test. Here the galaxy is placed in a constant wind to simulate the effect of the galaxy moving though the ICM. This allows parameters, like the relative speed of the ICM and galaxy, to be precisely controlled. The other method is to allow the galaxy to orbit within a cluster potential. This gives a more realistic representation of ram pressure stripping and includes tidal effects (which may or may not be desirable).

Many studies have been performed to investigate the effect of ram pressure stripping on spiral galaxies. Abadi, Moore & Bower (1999) used a smoothed particle hydrodynamics (SPH) code to simulate a three-dimensional spiral galaxy undergoing ram pressure stripping. Although their results match those of the analytic approach of Gunn & Gott, their simulations could not account fully for the observations. Roediger & Brüggen (2006) looked specifically at the role of the inclination angle of the disk and its effect on the morphology of the galaxy, using a grid based code. They found that the mass loss of the galaxy is relatively insensitive to the inclination angle for angles $\lesssim 60°$. They also noted that the tail does not necessarily point in the same direction as the motion of the galaxy. Jáchym *et al.* (2009) also looked at the role of inclination angle but used a SPH code. They find much the same dependence on inclination angle as Roediger & Brüggen (2006) although they saw no Kelvin-Helmholtz stripping[1]. Tonnesen & Bryan (2009) allowed the gas in the disk of the spiral galaxy to radiatively cool before being hit by the wind to allow areas of low and high density to develop. They found that gas is stripped more rapidly in the case with cooling as areas of lower density allow gas to also be stripped from the inner regions of the galaxy.

A number of studies have instead been focused on dwarf galaxies. Mori & Burkert (2000) looked at the stripping of the extended hot gas component using a two-dimensional grid based code. They found that the gas is totally stripped in a typical galactic cluster. Mayer *et al.* (2002) simulated a dwarf galaxy orbiting the Milky Way with an N-body code to probe the tidal effects on the dwarf galaxy and found a significant mass loss over a period of 7 Gyr. Mayer *et al.* (2006) used a

[1]This is likely due to the "negative pressure" which arises at interfaces in SPH models. Agertz *et al.* (2007) provide a detailed analysis of this effect.

combination of SPH and N-body simulations to study the combined effects of ram pressure and tidal stripping on dwarf galaxies. They pointed out that tidal effects can alter the morphology of the dwarf galaxy and change the effectiveness of ram pressure stripping. In general this increases effectiveness but tidally induced bar formation can funnel gas towards the centre of the galaxy, making it harder to strip.

In addition to these works a few papers contain results of work specifically on the effect of ram pressure stripping on the hot extended component of the gas. McCarthy *et al.* (2008) simulated a massive galaxy with a hot halo of gas undergoing ram pressure stripping. They performed both wind tunnel tests and simulations allowing the galaxy to orbit within a cluster to include tidal effects. They extended the analytic model of Gunn & Gott (1972) to the case of a spherical gas distribution and found that their formula fits simulations well when the galaxy represents less than 10% of the cluster mass. They suggested that at this point tidal effects and gravitational shock heating become important, which their model does not take into account. Bekki (2009) included both a hot halo and a disc in their model and suggested that the presence of the disk can suppress ram pressure stripping. Shin & Ruszkowski (2013) used a grid based code to look at the effects of turbulence within the ISM. They found that this increases mass loss and allows the ICM to penetrate further into a galaxy.

1.2 Protoplanetary disks and Stellar Feedback

Disks are a common feature around young stars, from high mass (Wang *et al.* 2012) to low mass brown dwarfs (Ricci *et al.* 2014). Stars are formed from the

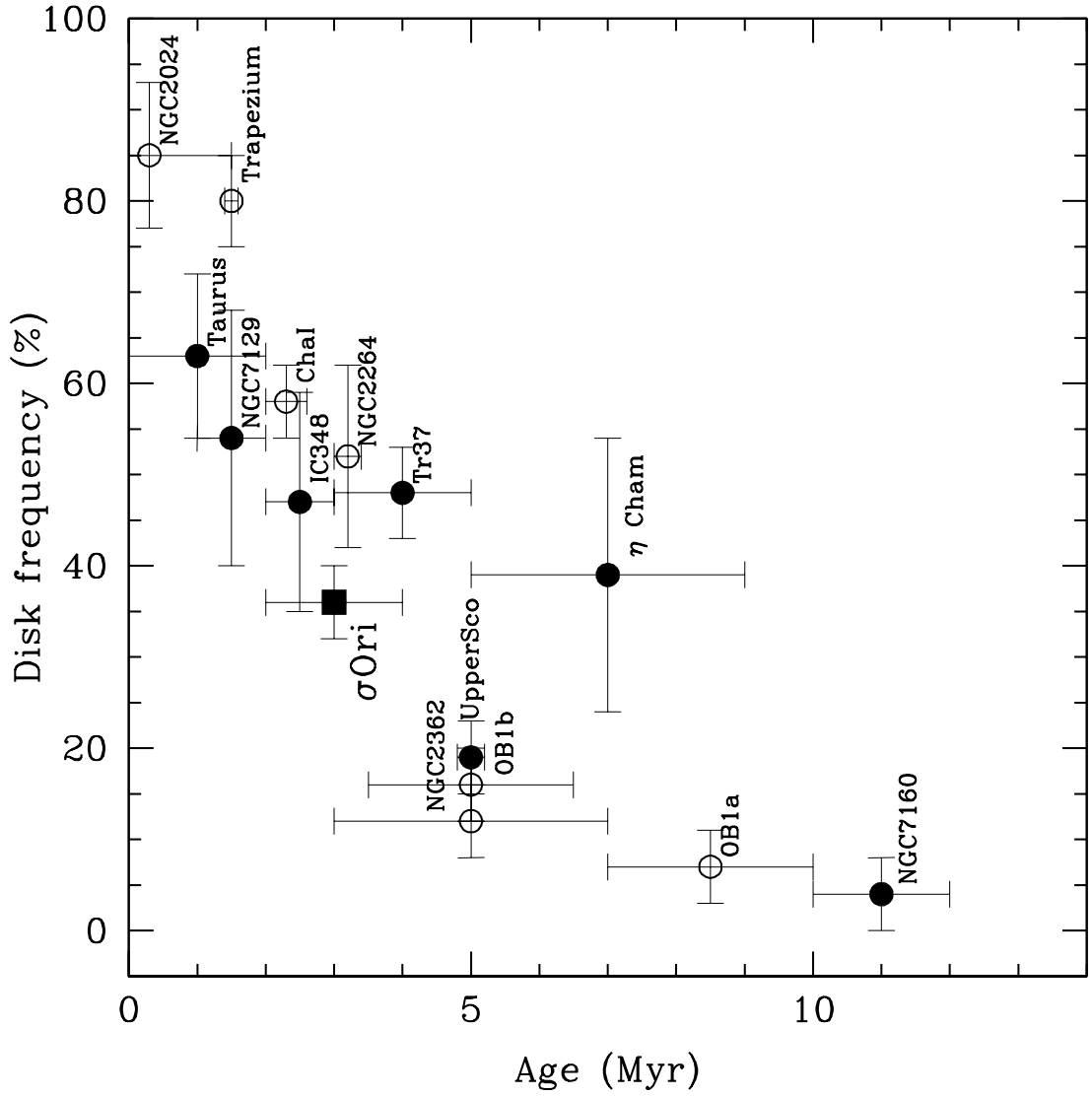

Figure 1.6: Disk frequency as a function of age for 15 different stellar populations. Disk frequency is measured as the ratio of stars with excess near-infrared disk emission to the total number of stars in the population. (Figure from Hernández *et al.* (2007))

gravitational collapse of dense gas clouds. Due to the angular momentum in the system, any left over gas that did not become part of the star forms a disk around it.

1.2.1 Disk dispersion

The disk has a finite lifetime, and do not occur around older stars. Figure 1.6 shows that stars older than $\sim 10\,\mathrm{Myr}$ are unlikely to have associated disks. The disk can be removed by a number of different processes. Possible mechanisms include accretion onto the central star, coalescence into planets, photoevaporation by the central star or external forces (radiation from a massive star, SNRs, tidal interactions etc.).

The time-scale for accretion to consume the disk depends primarily on the disk mass and the accretion rate of the star. For the entire disk to be consumed by accretion some mechanism is needed to redistribute the angular momentum in the disk, such that the outer material can fall into the star. This is generally attributed to some form of viscosity, arising due to instabilities in the disk. The accretion time-scale can be estimated as $M_{disk}/\dot{M}_{acc}$. Taking $M_{disk} = 0.5\,\mathrm{M}_{\odot}$ and $\dot{M}_{acc} = 10^{-8}\,\mathrm{M}_{\odot}\mathrm{yr}^{-1}$ (Garcia 2011; Williams & Cieza 2011) gives an accretion lifetime of 50 Myr. In practice $\dot{M}_{acc}$ decreases as the disk evolves (Hartmann *et al.* 1998) which has the effect of increasing the expected accretion lifetime significantly. It is clear there must be other mechanisms that remove the disk in order to match the observed lifetimes.

The picture of planet formation is a little more uncertain, and depends on complex dynamics (planet migration (Alibert *et al.* 2005) or gravitational instabilities (Durisen *et al.* 2007), for example) which can not be easily predicted from observables such as stellar mass, accretion rate or disk size. Theoretical models typically predict planet formation time-scales of $1 - 10\,\mathrm{Myr}$ (Guillot & Hueso 2006; Lissauer & Stevenson 2007; Lambrechts & Johansen 2012). However, in

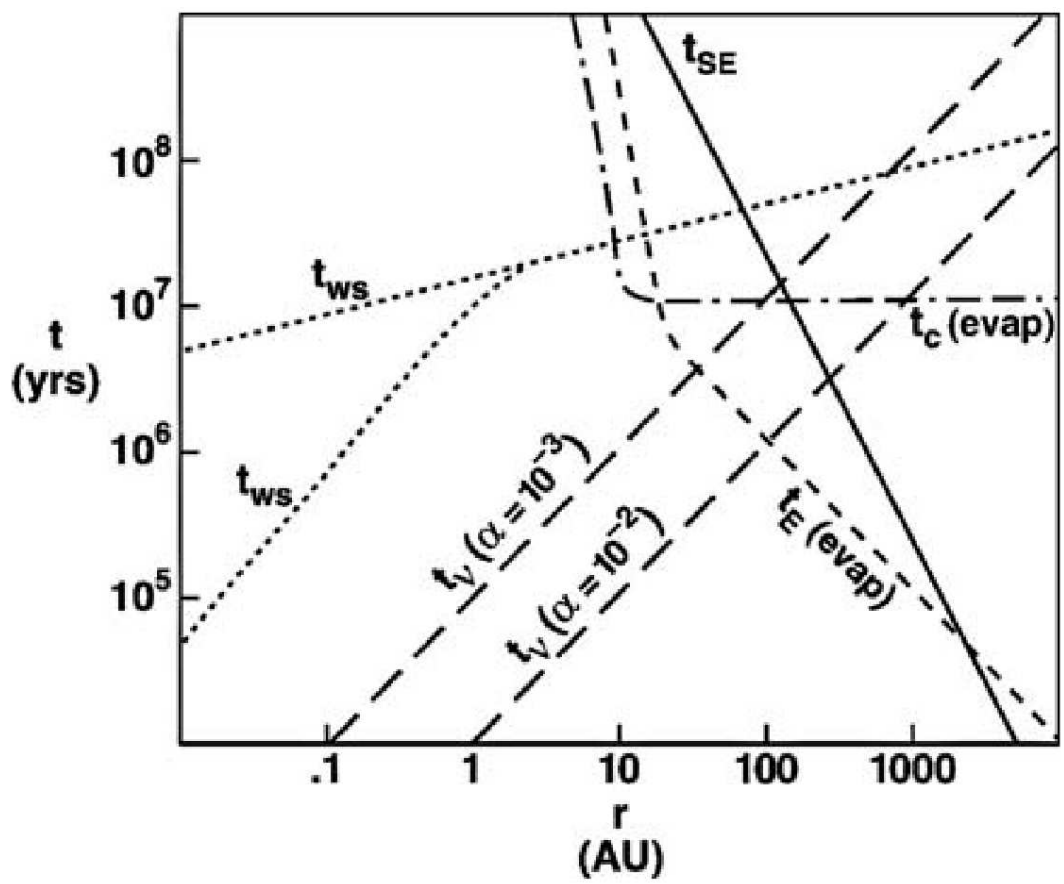

Figure 1.7: Various timescales for disk dispersal as a function of distance from the star for a minimum mass disk ($M_d = 0.01\,\mathrm{M}_\odot$). The different timescales are as follows. t_ν - accretion with viscous angular momentum transport, for two different disk viscosities. t_{SE} - stellar encounter (tidal stripping). t_{ws}, t'_{ws} - stellar wind assuming constant and decreasing mass loss rates respectively. $t_c(evap)$ - photoevaporation by the central star. $t_E(evap)$ - photoevaporation by an external star. (Figure from Hollenbach *et al.* (2000))

order for the planets to form in a reasonable time frame the initial disk mass must be 5-10 times larger than ends up contained within planets (Lissauer 1987, 1993), so planets can only play a small role in the overall dispersion of the proto-planetary disk. Given its minor role, it is likely that disk lifetimes mediate planet formation, rather than vice-versa.

Hollenbach *et al.* (2000) provides a summary of the timescales of different

disk dispersal mechanisms, as shown in Figure 1.7. Note that these timescales are given for a minimum mass disk. Timescales for a realistic disk are likely to be several times longer. Generally speaking, accretion dominates at small radii and photoevaporation at large radii. These two processes in combination with viscous spreading of disk material across radii can remove the entire disk within a few Myr (Richling & Yorke 1997).

1.2.1.1 External forces

From Figure 1.7 it is clear that internal effects are sufficient in removing the disk on the desired timescales. This should not come as a surprise as diskless stars can be observed in relatively quiescent regions (e.g. Armitage *et al.* (2003)). As massive stars are often the source of strong winds and eventually supernova, these regions are potentially hostile to protoplanetary disks and the subsistent formation of planets. There are $\sim$ 2000 low-mass stars within 2pc of the centre of the Trapezium cluster (Hillenbrand & Hartmann 1998), and stars with circumstellar disks (O'dell *et al.* 1993; McCaughrean & O'dell 1996; Bally *et al.* 1998) within a few tenths of a parsec of the central star,
$theta^1$ Ori C. The interactions massive stars have on other stars and their disks can be broadly categorised into the effects of gravitational, radiation or ablation.

When two stars pass one another, the associated disks become perturbed by the gravitational interaction. If this interaction is strong enough, material from the disk can become unbound (Clarke & Pringle 1993). Scally & Clarke (2001) use N-boby simulations to model the dynamics of the stars in the Orion Nebula. They find that only a small fraction of the stars interact closely on the expected disk dispersal timescales. Thus it seems that although these sort of interactions

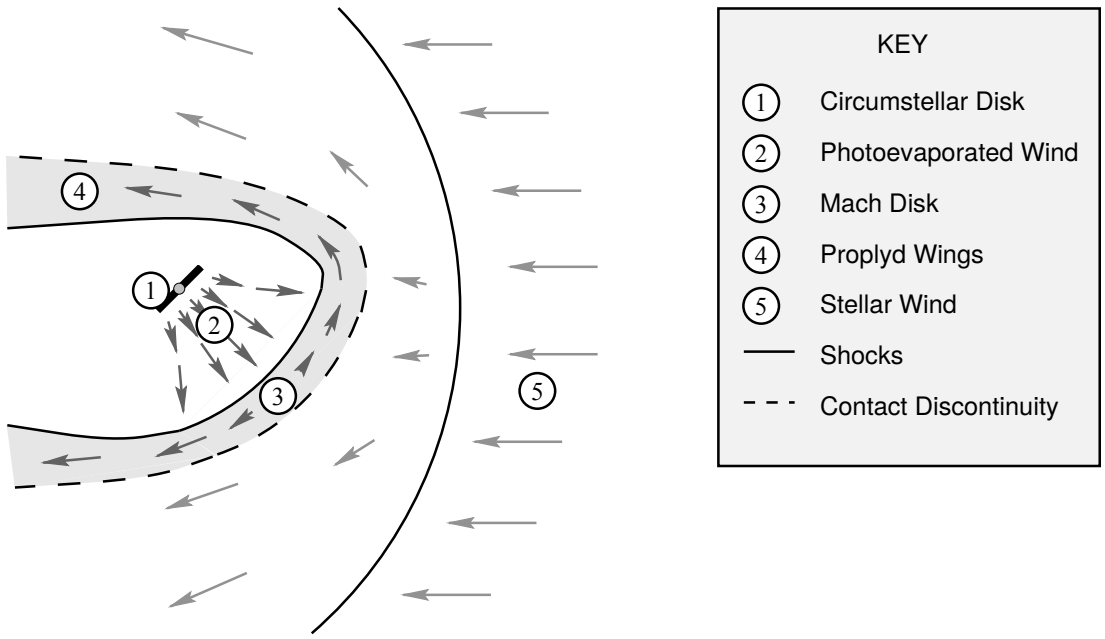

Figure 1.8: The proplyd two wind interaction model. The ionising photons from a nearby massive star drive a photoevaporation flow which interacts with the oncoming stellar wind. (Figure from Henney & Arthur (1997))

do occur they are not a major contributor to protoplanetary disk dispersal.

Direct observational evidence of the effects of radiation on disks is seen in the form of the proplyds in the Orion Nebula (e.g. O'dell & Wen (1994); McCaughrean (2001)). The radiation from θ^1 Ori C causes a photoevaporation flow from the disks which collides with the oncoming stellar wind. This results in a number of cometary-shaped ionization fronts associated with stars around θ^1 Ori C. Estimates put the mass-loss rate of the proplyds at $\sim 4 \times 10^{-7}\,\mathrm{M}_\odot\,\mathrm{yr}^{-1}$ (Henney & O'Dell 1999). If sustained over the lifetime of the cluster this would mean that the stars would have had unrealistically massive disks (greater than the star's mass) at some point in the past. However, θ^1 Ori C may have switched on only $\sim 10^5$ years ago (Scally & Clarke 2001). Hence, it is unlikely that in a few $\times 10^5$ years the combination of photoevaporation and viscous accretion will

have depleted the disks (Garcia 2011). This suggests that the Origin Nebula is in a relativity short-lived stage of it's evolution, which is consistent with the lack of proplyd-like objects in other clusters (e.g. Stapelfeldt *et al.* (1997); Balog *et al.* (2006)).

While there is a lot of evidence, both from theory and observations, that massive stars influence the disks of neighbouring stars, observational surveys show little difference in the disk frequency near massive stars (Hillenbrand *et al.* 1998; Richert *et al.* 2015). It is unclear how much of an effect massive stars have on disk lifetimes, although it seems that if disks are affected they are only partially destroyed.

Supernova remnants (SNRs) provide another source of agitation for proto-planetary disks. There is evidence in π Sco of circumstellar disks similar to those in the Origin nebula (Bertoldi & Jenkins 1992) and that a supernova occurred nearby $\sim 10^6$ yrs ago (de Geus 1992). Lada & Lada (2003) compiled a catalog of embedded clusters and find that the vast majority (70 - 90%) of stars form in clusters of > 100 members, and the majority of those ($\sim 75\%$) are in clusters containing stars massive enough to give rise to supernovae (Hester & Desch 2005).

Analytic estimates for the ablation of protoplanetary disks due to a SNR were presented by (Chevalier 2000). He found that for typical disk and supernova parameters, partial stripping of the disk can occur, but typically not its complete disruption. This suggests that although the disks are affected, they can survive such events.

1.2.2 Short-lived radionuclides

The interaction of a SNR with a protoplanetary disk is also of interest from the point of view of injecting short-lived radionuclides (SLRs) into the early solar system (e.g. Jacobsen (2005); Looney *et al.* (2006)). Analyses of meteorites suggest that the early solar system had a $^{60}Fe/^{56}Fe$ ratio of $\sim 3 - 7 \times 10^{-7}$, far above the average interstellar medium (ISM) value (Quitté *et al.* 2005; Tachibana *et al.* 2006). The short half-life of ^{60}Fe (1.5 Myr) constrains the timing of it's injection into the solar system to a relativity recent event. Other SLRs can be explained by production internal to the solar system (Lee *et al.* 1998; Gounelle *et al.* 2006) although the yields of ^{60}Fe are much too low to explain the abundances derived from meteorites.

The amount of ^{60}Fe produced by supernovae varies depending on the mass and metallicity of the exploding star. Calculations by Woosley & Weaver (1995) put the $^{60}Fe/^{56}Fe$ ratio at typically $1 - 3 \times 10^{-3}$. In order to reach the ratio $^{60}Fe/^{56} \sim 3{-}7{\times}10^{-7}$ needed for the young solar nebula, the supernova ejecta must contribute a fractional mass of $\sim 3 - 7 \times 10^{-4}$ to the disk. Given that supernovae are abundant sources of nucleosynthesis and they are often in close proximity to young, low mass stars the consensus is that they are a likely candidate for the source of ^{60}Fe in the early solar system[1].

[1] One problem with this model is that supernova produce different ratios of specific SLRs (i.e. $^{60}Fe/^{26}Al$ is too low in supernova ejecta) compared with what is inferred from meteorite analysis, though perhaps different sized dust grains offer a solution.

1.2.3 Hydrodynamical simulations

Hydrodynamical simulations of the interaction of a SNR with a circumstellar disk were performed by Ouellette *et al.* (2007). They found that only a small fraction ($\sim 1\%$) of the disk mass is removed, in contrast to the $\sim 13\%$ expected from the analytical prediction of Chevalier (2000). They attribute this to the cushioning and deflecting effect of the bow shock in addition to the compression of the disk further into the gravitational well of the central star. However their simulations are limited to two dimensions and face-on impacts. While an inclined disk might be expected to be disadvantageous for ablation, the geometry of the bowshock that shields the disk is likely to be substantially different and the impacting flow acts with the rotation of the disk on one side, reducing the threshold for ablation. They also found that only $\sim 1\%$ of the passing ejecta is captured by the disk. This is not enough to explain the observed abundances, although they suggest that dust grains might be a more efficient mechanism for injecting SLRs into the disk.

To investigate this possibility, Ouellette *et al.* (2010) incorporated dust grains into their simulations. They found that about 70% of dust grains larger than $0.4\,\mu$m are injected into the disk. This could potentially be enough to explain the observed abundances, although it relies on higher than observed dust condensation in the ejecta and the ejecta to be clumpy with the disk being hit by a high density clump of ejecta. They estimate the probability of these conditions being met at $0.1 - 1\%$ and that the solar system may be atypical in this respect.

The mixing effects of clumpy supernova ejecta interacting with a molecular cloud were investigated by Pan *et al.* (2012). When the mixing is efficient the

ejecta contamination is $\sim 10^{-4}$. This is approximately the correct level, although as the SLRs are injected into the molecular cloud, and it takes of order a Myr to form stars and disks, the abundance of ^{60}Fe could be significantly reduced in this time.

The formation and subsequent evolution of a star-disk system under the effects of a supersonic wind were investigated by Li *et al.* (2014). They found that a disk can indeed form and survive in these conditions: a $10^{-3}\,M_\odot$ disk remains after being exposed to the wind for 0.7 Myr. However, their disk radius after formation is ~ 1000 au, whereas disks near massive stars are typically photoevaporated down to tens of au (Johnstone *et al.* 1998). The flow speed is also much slower than that adopted by Ouellette *et al.* (2007), which in turn reduces the ram pressure significantly. Therefore, while their work was useful for investigating triggered star formation, the region of parameter space that they explored is unrealistic for disk ablation via nearby supernova.

Recently Goodson *et al.* (2016) performed three dimensional simulations of the interaction of a SNR with a large (8.8 pc), clumpy molecular cloud, including dust grains. They found that the majority of large dust grains are injected into the molecular cloud, and within 0.1 Myr of the supernova explosion. They note that if ^{60}Fe and ^{26}Al preferentially condense onto different sized grains this could explain the discrepancy in the ratio between the two SLRs.

1.3 Turbulence limited simulations

One of the principle ways in which the above phenomenon are studied is though the use of numerical simulations. Due to the limited nature of computational

resources and the desire to include additional physics[1], it is always desirable to keep resolution to the minimum required to simulation the problem correctly. One of the things that limits the necessary resolution is turbulence. Turbulence is generated by instabilities in the fluid, which lead to the formation of smaller and smaller eddies. This increases the diffusivity of the flow, accelerating the mixing of fluids and increases dissipation, converting kinetic energy into internal energy via viscous shear stresses.

Fig 1.9 shows the generation of turbulence by the Kelvin-Helmholtz instability. This is of particular interest in the context of ablation, as these instabilities are generated along the side of the object being ablated by the shear between the object and the wind. When the resolution of a simulation is too low, it is unable to resolve the small eddies, limiting the diffusive and dissipative effects of the turbulence.

This problem can be overcome by using a statistical model to account for the effects of turbulence. This is a common practice in terrestrial applications of fluid dynamics but is still relatively unexplored in an astrophysical context. One turbulence model is the k-ϵ model, described in more detail in Section 2.2.

1.4 Thesis Outline

This chapter has detailed how ablation is an important topic in astrophysics and why turbulence plays a crucial role. Chapter 2 details the numerical methods that will be used in this thesis. Chapter 3 presents numerical simulations of galactic ram pressure stripping and how the k-ϵ model can be used to improve accuracy.

[1]Such as magnetic fields, self-gravity, heating/cooling, chemistry, etc.

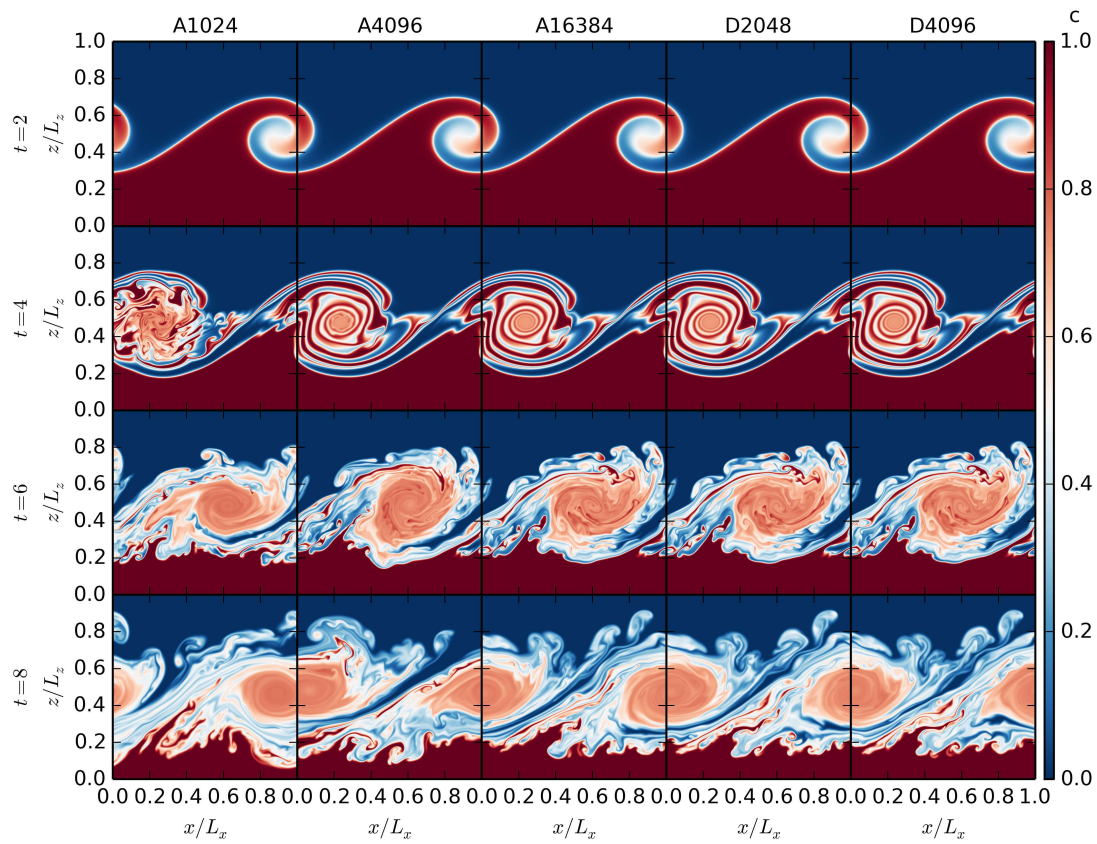

Figure 1.9: The evolution of the Kelvin-Helmholtz instability. The red and blue fluids have opposing velocities in the x direction. Any small perturbations in the boundary are enhanced and mixing occurs between the two layers. Each row corresponds to a different time, each column is a different code/resolution. (Figure from Lecoanet *et al.* (2016))

Chapter 4 shows the limits of the k-ϵ model when used to simulate disks. Chapter 5 presents simulations of the interaction of circumstellar disks and SNRs. Finally Chapter 6 provides a summery of the conclusions draw in this thesis and how they can be build upon in future research.

Chapter 2

Numerical Methods

The simulations presented in Chapters 3, 4 and 5 were calculated using the hydrodynamics code `MG`. This chapter outlines the numerical methods and theory employed by `MG` in order to produce accurate and reliable fluid dynamics data.

2.1 The Governing equations

The aim of any fluid dynamics code is to find a solution to a set of equations know as the Navier-Stokes equations. In the case of zero viscosity and zero thermal conductivity (which will be assumed in this thesis), the equations reduce to the Euler equations.

The Euler equations are supplemented by the k-ϵ model which aims to model highly turbulent flows. The details and reasons for using such a model are noted in Section 2.2.

The Euler equations in Cartesian coordinates, with the k-ϵ model, consist of

six equations. These are: the continuity equation,

$$\frac{\partial \rho}{\partial t} + \nabla \cdot (\rho \boldsymbol{u}) = 0, \tag{2.1}$$

momentum conservation,

$$\frac{\partial \rho \boldsymbol{u}}{\partial t} + \nabla \cdot (\rho \boldsymbol{u}\boldsymbol{u}) + \nabla P - \nabla \cdot \boldsymbol{\tau} = \rho \boldsymbol{g}, \tag{2.2}$$

energy conservation,

$$\frac{\partial E}{\partial t} + \nabla \cdot [(E + P)\boldsymbol{u} - \boldsymbol{u} \cdot \boldsymbol{\tau}] - \frac{\gamma}{\gamma - 1} \nabla \cdot (\mu_T \nabla T) = \rho \boldsymbol{u} \cdot \boldsymbol{g} - P_t + \rho \epsilon, \tag{2.3}$$

an equation for advected scalars,

$$\frac{\partial \rho C}{\partial t} + \nabla \cdot (\rho C \boldsymbol{u}) - \nabla \cdot (\mu_T \nabla C) = 0, \tag{2.4}$$

turbulent energy,

$$\frac{\partial \rho k}{\partial t} + \nabla \cdot (\rho k \boldsymbol{u}) - \nabla \cdot (\mu_T \nabla k) = P_t - \rho \epsilon, \tag{2.5}$$

and the turbulent energy dissipation rate

$$\frac{\partial \rho \epsilon}{\partial t} + \nabla \cdot (\rho \epsilon \boldsymbol{u}) - \nabla \cdot (\mu_\epsilon \nabla \epsilon) = \frac{\epsilon}{k}(C_1 P_t - C_2 \rho \epsilon). \tag{2.6}$$

Here ρ is the mass density, $\boldsymbol{u}$ is the velocity and P is the thermal pressure. E is the total energy density (thermal and kinetic) and is given by the equation of

state:

$$E = \frac{p}{\gamma - 1} + \frac{\rho \boldsymbol{u}.\boldsymbol{u}}{2}, \tag{2.7}$$

where γ is the adiabatic index of the gas. C represents any advected scalar. An advected scalar has no physical meaning or impact on the other fluid variables but is used to mark regions of fluid so that they can be traced as the simulation evolves. $\boldsymbol{g}$ is the local acceleration due to gravity. The k-ϵ model adds the variables, k, the turbulent energy per unit mass and ϵ, the turbulent dissipation rate per unit mass. $C_1 = 1.4$ and $C_2 = 1.94$ are both constants of the k-ϵ model. The effect of k and ϵ on the other fluid variables is characterised by

$$\mu_T = \rho C_\mu \frac{k^2}{\epsilon}, \tag{2.8}$$

and

$$\mu_\epsilon = \frac{\mu_T}{1.3}, \tag{2.9}$$

where $C_\mu = 0.09$. P_t is the turbulent production term. Using the summation convention,

$$P_t = \mu_T \left[\frac{\partial u_i}{\partial x_j} \left(\frac{\partial u_i}{\partial x_j} + \frac{\partial u_j}{\partial x_i} \right) \right] - \frac{2}{3} \nabla \cdot \boldsymbol{u} (\rho k + \mu_T \nabla \cdot \boldsymbol{u}). \tag{2.10}$$

$\boldsymbol{\tau}$ is the turbulent stress tensor and is defined as

$$\tau_{ij} = \mu_T \left(\frac{\partial u_i}{\partial x_j} + \frac{\partial u_j}{\partial x_i} \right) - \frac{2}{3} \delta_{ij} (\rho k + \mu_T \nabla \cdot \boldsymbol{u}). \tag{2.11}$$

The equations simplify to the Euler equations for $k = 0$.

2.2 The k-ϵ sub-grid turbulence model

The turbulent behaviour of a flow is characterised by its Reynolds number, which can be used to relate the sizes of the smallest and largest eddies,

$$\eta \sim R_e^{-3/4} l, \tag{2.12}$$

where η and l are the scales of the smallest and largest eddies, respectively. l is typically of the scale of the turbulent region. Astrophysical flows can have Reynolds numbers of 10^5 or higher. To simulate such a flow using pure hydrodynamics $\sim$ 5000 cells would be needed across the turbulent region in order to start to resolve the smallest scale eddies. This is far beyond the capabilities of modern hardware, and in order to simulate such flows accurately a statistical approach is required.

The Euler equations are already a statistical model in many ways. Any fluid worth simulating contains many more particles than can simulated individually. The fluid can be thought of being the sum of two components, the bulk motion of the particles and their motions relative to one another. So density and velocity become spatial-averaged terms, and the information of the individual particles is represented in the internal energy term. This allows the fluid to be simulated without having to worry about the details of the individual particles.

In a similar way, the turbulent motion of a fluid can be separated from the time-averaged flow. One widely used method of achieving this goal is the k-ϵ model. This model introduces two additional fluid variables to represent the

turbulent motions of the flow, k and ϵ, governed by equations 2.5 and 2.6 respectively. The earliest development efforts on this model were by Chou (1945). The closure coefficients were subsequently adjusted by Launder & Sharma (1974) to create the accepted "standard" model, and its popularity has led to it featuring extensively in textbooks (e.g., Pope 2000; Davidson 2004; Wilcox 2006). Turbulence is modelled through the use of k and ϵ to calculate a turbulent viscosity which increases the transport coefficients in regions of high turbulence.

The equations that determine k and ϵ are largely empirical, but have been used to great success in engineering and also in some astrophysical problems (Falle 1994, Pittard *et al.* 2009, Pittard, Hartquist & Falle 2010). For instance, Pittard *et al.* (2009) found that k-ϵ simulations of the turbulent ablation of clouds showed much better convergence in resolution tests than inviscid simulations, and that the converged solution in the k-ϵ models was in good agreement with the highest resolution inviscid models. Of course, other possibilities and variations also exist for modelling turbulent flows. For instance, Scannapieco & Brüggen (2008) use a model similar to the k-ϵ model to capture the Rayleigh-Taylor and Richtmyer-Meshkov instabilities and buoyancy-driven turbulence in active galactic nuclei, and Schmidt & Federrath (2011) recently developed a subgrid model for highly compressible astrophysical turbulence.

The k-ϵ model works well for shear flows, but can fail for non-anisotropic flows or when boundary layers contain large pressure gradients (Hanjalic 1994; Davidson 2004). The advantage of the k-ϵ model over other models is its ease of implementation, low dependence on initial turbulent energy (as typically the amount of turbulence in a problem is not known prior to simulation) and the cases where it fails are well documented.

The implementation of the k-ϵ model is described in more detail in Falle (1994). Thought out this thesis, the term "inviscid" is used to refer to simulations performed without the use of the k-ϵ model. The following sections detail how the equations of hydrodynamics can be solved, and omit the turbulent terms for simplicity.

2.3 The Finite volume method

As the Euler equations have no general analytical solution, a numerical method must be used to find an approximate solution. In order to do so, they must first be discretised. The domain is divided into finite volumes (which will be referred to as cells) such that the Euler equations can be integrated over that volume, e.g., for Equation 2.1:

$$\iiint_V \frac{\partial \rho}{\partial t} dV + \iiint_V \nabla \cdot (\rho \boldsymbol{u}) dV = 0, \tag{2.13}$$

using the divergence theorem becomes

$$\frac{\partial \rho V}{\partial t} + \oint_A \rho(\boldsymbol{u} \cdot \hat{\boldsymbol{n}}) dA = 0. \tag{2.14}$$

This equation states that the rate of change of mass contained with a volume V, is equal to the mass flux though the surface, A, that bounds it. Meaning that mass can move from one volume to another, but the total mass is conserved.

The equations must also be discretised in time. The change from one discrete

time to the next is given by integrating the flux over the time between them,

$$\rho_{\boldsymbol{i}}^{n+1} = \rho_{\boldsymbol{i}}^{n} - \int_{t_n}^{t_{n+1}} F_{\boldsymbol{i}}(\rho) dt \tag{2.15}$$

where $F_{\boldsymbol{i}}$ is the total flux across the surface bounding the cell indexed by $\boldsymbol{i}$.

Consider a one-dimensional flow, across cubic cells with side length, l. The total flux in the x direction is the difference between the fluxes of the left and right faces,

$$F_i(\rho) = F_{i-1/2}(\rho) - F_{i+1/2}(\rho) \tag{2.16}$$

To fully discretise the equation, F needs to be replaced with its average value,

$$\int_{t_n}^{t_{n+1}} F_i(\rho) dt = \Delta t \bar{F}_i(\rho). \tag{2.17}$$

Combining equations 2.14, 2.16 and 2.17 gives the mass advection step in the x direction,

$$\rho_{i,j,k}^{n+1} = \rho_{i,j,k}^{n} + \Delta t \bar{F}_{i-1/2,j,k}(\rho) - \Delta t \bar{F}_{i+1/2,j,k}(\rho), \tag{2.18}$$

where the index $\boldsymbol{i}$ has become i, j, k to represent the three dimension index of the cubic grid. This procedure is repeated for the momentum and energy equations to obtain

$$(\rho u)_{i,j,k}^{n+1} = (\rho u)_{i,j,k}^{n} + \Delta t \bar{F}_{i-1/2,j,k}(\rho u) - \Delta t \bar{F}_{i+1/2,j,k}(\rho u), \tag{2.19}$$

and

$$E^{n+1}_{i,j,k} = E^{n}_{i,j,k} + \Delta t \bar{F}_{i-1/2,j,k}(e+P) - \Delta t \bar{F}_{i+1/2,j,k}(e+P). \tag{2.20}$$

The final step is to determine the average fluxes, $\bar{F}$. This is done by solving the Riemann problem.

2.4 The Riemann problem

The Riemann problem starts with two regions, each with constant density, pressure and velocity. If $\boldsymbol{W}$ represents the vector of primitive values,

$$\boldsymbol{W} = \begin{bmatrix} \rho \\ u \\ p \end{bmatrix}, \tag{2.21}$$

then the initial values of the Riemann problem are,

$$\boldsymbol{W}(x,0) = \begin{cases} \boldsymbol{W}_L & \text{if } x < 0 \\ \boldsymbol{W}_R & \text{if } x > 0. \end{cases} \tag{2.22}$$

By solving the Riemann problem, the fluxes for each fluid variable between the two regions can be calculated, and the cell values updated via equations 2.18 - 2.20. Treating each cell-cell interface as a Riemann problem is only valid if the waves emanating from one interface cannot interact with another. This imposes the so called Courant-Friedrichs-Lewy condition, $\Delta t \leq Cl/u$, where C is the Courant number, which depends on a number of factors, notably the dimensionality of the problem and the precise nature of the Riemann solver. For the work

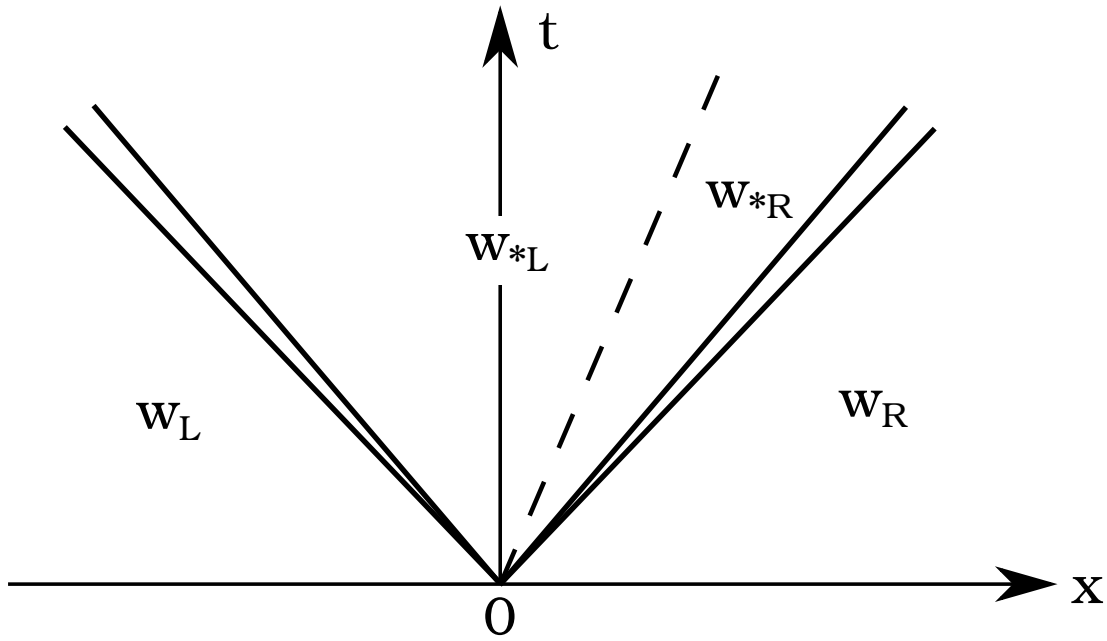

Figure 2.1: Space-time diagram showing the solution to the Riemann problem. The dashed line represents a contact discontinuity, the pairs of lines to the left and right represent the unknown waves.

presented in this thesis, $C = 0.2$, which gives good numerical stability for three dimensional problems.

The solution to the Riemann problem has three distinct waves, splitting the flow into four regions, W_L, W_{*L}, W_{*R} and W_R, as show in fig 2.1. The inner two regions are separated by a contact discontinuity, meaning that the pressure and velocity of these two regions are the same, i.e., $P_{*L} = P_{*R} = p_*$ and $u_{*L} = u_{*R} = u_*$. This leaves four unknown quantities, p_*, u_*, ρ_{*L} and ρ_{*R}.

The pressure, p_* is found by solving the equation Toro (2009),

$$f(p_*, \boldsymbol{W}_L, \boldsymbol{W}_R) = f_{L/R}(p_*, \boldsymbol{W}_L) + f_{L/R}(p_*, \boldsymbol{W}_R) + u_R - u_L = 0, \qquad (2.23)$$

where

$$f_{L/R}(p_*, \boldsymbol{W}) = \begin{cases} (p_* - p)\left[\frac{2}{((\gamma+1)p_* + (\gamma-1)p)\rho}\right]^{1/2} & \text{if } p_* > p \text{ (shock)}, \\ \frac{2}{\gamma-1}\sqrt{\frac{\gamma p}{\rho}}\left[\left(\frac{p_*}{p}\right)^{\frac{\gamma-1}{2\gamma}} - 1\right] & \text{if } p_* \leq p \text{ (rarefaction)}. \end{cases} \tag{2.24}$$

In the case where both left and right waves are rarefactions, the equation is solvable directly. In the case of a shock, the equation is solved by a Newton-Raphson iterative method, i.e.,

$$p_{*i+1} = p_{*i} - \frac{f(p_{*i}, \boldsymbol{W}_L, \boldsymbol{W}_R)}{f'(p_{*i}, \boldsymbol{W}_L, \boldsymbol{W}_R)}. \tag{2.25}$$

The initial guess is given a linear solver,

$$p_0 = \frac{\rho_R a_R p_L + \rho_L a_L p_R - \rho_R \rho_L a_R a_L (u_R - u_L)}{\rho_R a_R + \rho_L a_L}. \tag{2.26}$$

This can be iterated arbitrarily many times to achieve the desired precision, at the expense of CPU time. `MG` iterates until p_{*i+1} and p_{*i} differ by less than 0.01%. In the case that the initial guess from the linear solver differs by less than 10% from either p_L or p_R, p_0 is taken as the final value and the iterative method is not used. This initial guess is also used to determine whether each wave is a rarefaction or a shock for Equation 2.24.

Once the pressure is known, the velocity, u_* can be calculated simply from,

$$u_* = \frac{1}{2}(u_L + u_R) + \frac{1}{2}[f_{R/L}(p_*, \boldsymbol{W}_R) - f_{R/L}(p_*, \boldsymbol{W}_L)]. \tag{2.27}$$

The density in regions W_{*L} and W_{*R} can now be found. In the case of a shock,

the Rankine-Hugoniot conditions can be used. As the speed of the shock is not known explicitly at this point, the three Rankine-Hugoniot conditions (for mass, momentum and energy) must be combined, giving,

$$\rho_{*K} = \rho_K \left[\frac{\frac{p_*}{p_K} + \frac{\gamma-1}{\gamma+1}}{\frac{\gamma-1}{\gamma+1}\frac{p_*}{p_K} + 1} \right], \tag{2.28}$$

where K is either L or R for the left and right waves respectively. In the case of a rarefaction, assuming isentropic expansion,

$$\rho_{*K} = \rho_K \left(\frac{p_*}{p_K} \right). \tag{2.29}$$

By calculating the speed of each wave, the cell boundary (at $x = 0$) can be placed within one of the four regions (or possibly within the rarefaction fan if one exists). If the wave speed is positive it falls to the right of the boundary, and to the left if it is negative. A rarefaction has two wave speeds, one for the head, and one for the tail. The wave speeds for all possible waves are:

$$S_{cd} = u_*, \tag{2.30}$$

$$S_{shock,K} = u_K \mp a_K \left[\frac{\gamma+1}{2\gamma}\frac{p_*}{p_K} + \frac{\gamma-1}{2\gamma} \right]^{1/2}, \tag{2.31}$$

$$S_{rf,head,K} = u_K \mp a_K, \tag{2.32}$$

$$S_{rf,tail,K} = u_{*K} \mp a_{*K}, \tag{2.33}$$

where $\mp$ takes the upper sign for the left wave and the lower sign for the right wave. If $S_{rf,head,K}$ and $S_{rf,tail,K}$ have opposing signs the cell boundary falls inside the rarefaction fan. Unlike the other regions, the values within the fan are not uniform, and are given by,

$$\boldsymbol{W}_{rf,K}(x,t) = \begin{cases} \rho_{rf,K}(x,t) = \rho_K \left[\frac{2}{\gamma+1} \pm \frac{\gamma-1}{(\gamma+1)a_K}\left(u_K - \frac{x}{t}\right)\right]^{\frac{2}{\gamma-1}}, \\ u_{rf,K}(x,t) = \frac{2}{\gamma+1}\left[\frac{\gamma-1}{2}u_K \pm a_K + \frac{x}{t}\right], \\ p_{rf,K}(x,t) = p_K \left[\frac{2}{\gamma+1} \pm \frac{\gamma-1}{(\gamma+1)a_K}\left(u_K - \frac{x}{t}\right)\right]^{\frac{2\gamma}{\gamma-1}}, \end{cases} \tag{2.34}$$

where $\pm$ takes the upper sign for the left wave and the lower sign for the right wave. At the cell boundary ($x = 0$) $\boldsymbol{W}_{rf,K}$ is constant over time. It follows that the flux over the boundary is also constant. By knowing which region the cell boundary is in the average flux can be calculated. This procedure is done for all six faces of the cell and summed together to get the total flux for that cell. The fluid variables can then be updated via equations 2.18, 2.19 and 2.20.

2.5 Other details

While the above methods are sufficient for numerical calculations, there are a number of other methods employed by `MG` in order to ensure accurate results at low computational cost.

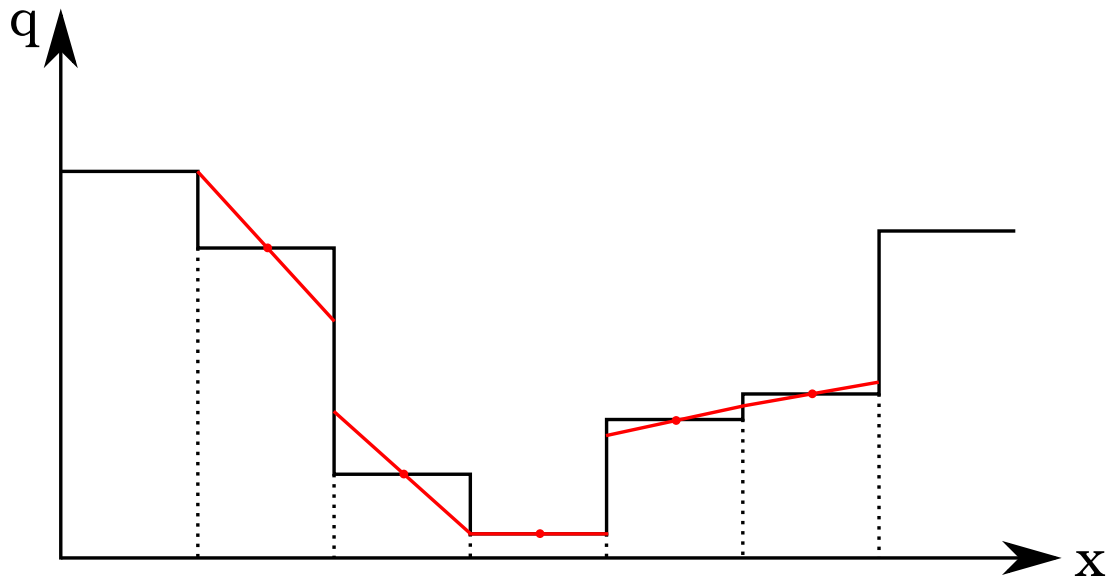

Figure 2.2: An example of the piecewise linear interpolation of some fluid variable, q. Black lines show the constant value in each cell, red lines show the interpolated values, red dots are the mid-points of each cell and dash lines show the boundary between cells.

2.5.1 Second order accuracy

2.5.1.1 Space - Piecewise linear interpolation

The scheme outlined above is accurate to first order in space and time. The first order accuracy in space comes from assuming fluid variables do not vary within cells (piecewise constant method, PCM). This can be improved by interpolating between cell values using the piecewise linear method (PLM). Higher orders of interpolation give less diffusive results but at a higher computational cost. `MG` achieves second order accuracy in space using piecewise linear interpolation. The steepest slope is used under the condition that values at the cell boundaries lie between the constant cell values. An example of the resulting construction is shown in Figure 2.2.

2.5.1.2 Time - Predictor-corrector method

If $\boldsymbol{W}_i$ represents the state of a cell at step i, and $\text{step}_{PCM/PLM}(\boldsymbol{W}, dt)$ represents a function that advances the solution $\boldsymbol{W}$ by dt using either PCM or PLM. The above methods describe the scheme,

$$\boldsymbol{W}_{i+1} = \text{step}_{PLM}(\boldsymbol{W}_i, dt), \tag{2.35}$$

which is accurate to second order in space and first order in time. Second order accuracy can also be achieved in time using a predictor-corrector method,

$$\begin{aligned} \boldsymbol{W}_{i+1/2} &= \text{step}_{PCM}(\boldsymbol{W}_i, dt/2) \\ \boldsymbol{W}_{i+1} &= \text{step}_{PLM}(\boldsymbol{W}_{i+1/2}, dt). \end{aligned} \tag{2.36}$$

This can, in principle, be extended to higher orders[1] however this comes with a higher computational cost (which might be better spent on higher resolution or shorter timesteps, for example). The second order method provides a good balance between accuracy and computational cost.

2.5.2 Adaptive Mesh Refinement

Often the spatial resolution needed to perform a simulation accurately is determined by a small fraction of the region. For example, many cells are needed to resolve the sharp features of a shock, however the pre- and post-shock material can be smooth in comparison and require much lower resolution. By using multiple different sized cells across the grid, the sharp features can be resolved while

[1]The fourth order Runge-kutta method for example, often considered the standard for solving ordinary differential equations.

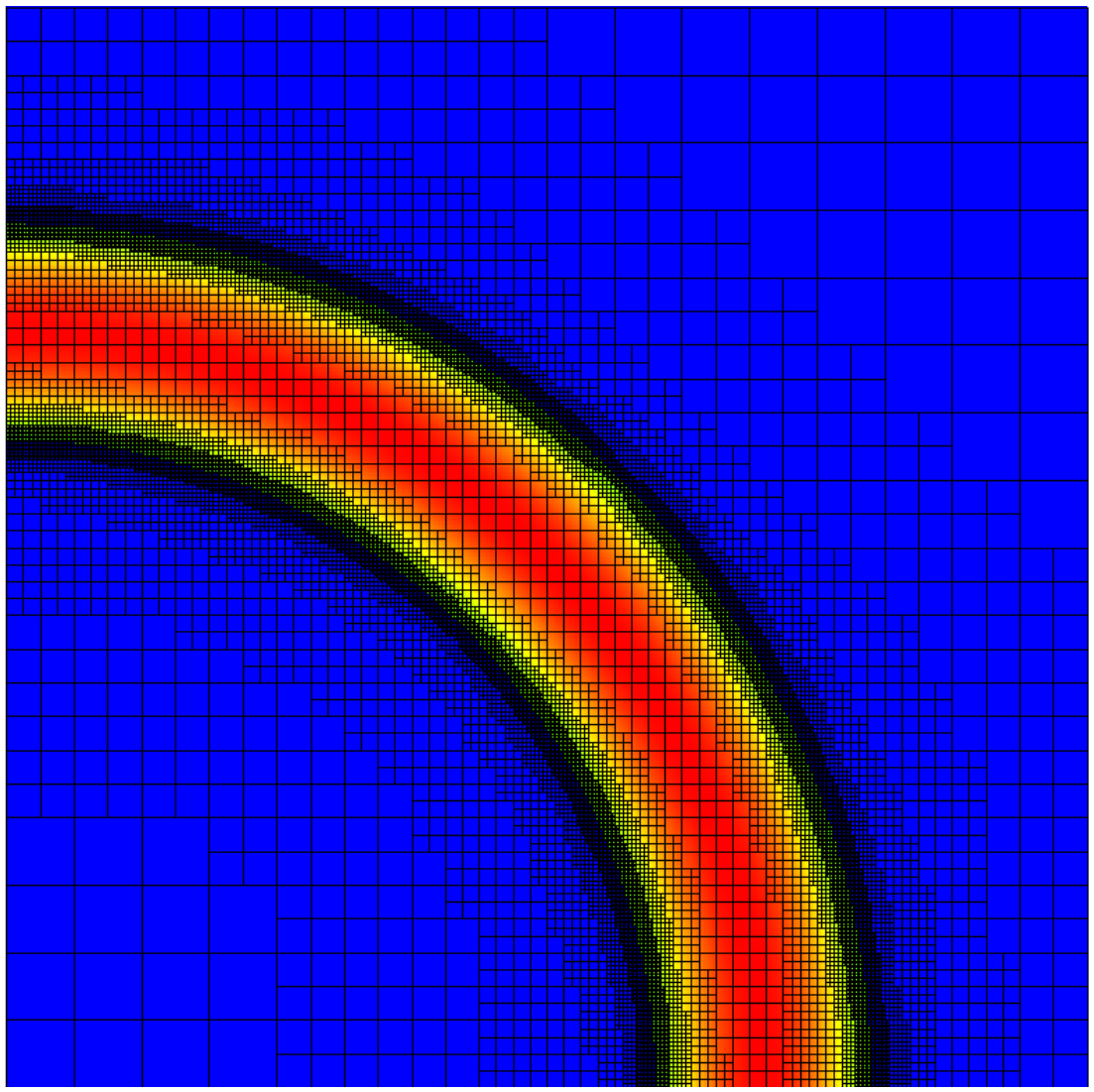

Figure 2.3: An AMR grid with seven levels of refinement. Regions where the density (shown as the colour map) changes quickly are given more cells and therefore higher spatial resolution.

keeping the computational cost low.

MG does this dynamically using a technique known as Adaptive Mesh Refinement (AMR). A number of different grid levels are used, each containing cells half the size in each dimension. The two lowest grid levels cover the entire region of interest. Each level solves the Riemann problem, calculates fluxes and updates fluid variables independently. The values are compared and in regions where the results differ by more than a user defined tolerance (with a default of 1%) finer cells are added. This highlights regions where the fluid has steep gradients that the coarser cells can not resolve. Cells can be removed if the solutions of the levels below agree to within the specified tolerance. Refinement is done on a cell by cell basis (as opposed to in patches which is common in other hydrocodes), although the code will try to refine neighbouring cells in order to ensure accuracy in the surrounding region and prevent neighbouring cells being more than one level apart.

When cells are refined, the coarse cell still exists and must be updated along with the fine cells in order to provide a comparison to test for potential refinement or derefinement. This adds a certain amount of overhead to the computations, making AMR unsuitable to situations where a high resolution is needed across the entire computational domain. However when this is not the case, the overhead is outweighed significantly by the overall reduction in the number of cells on the grid.

2.5.2.1 Coarse-fine boundaries

The boundaries between cells on different levels of refinement (shown in red in Figure 2.4a) must be treated with some care to maintain consistency across levels

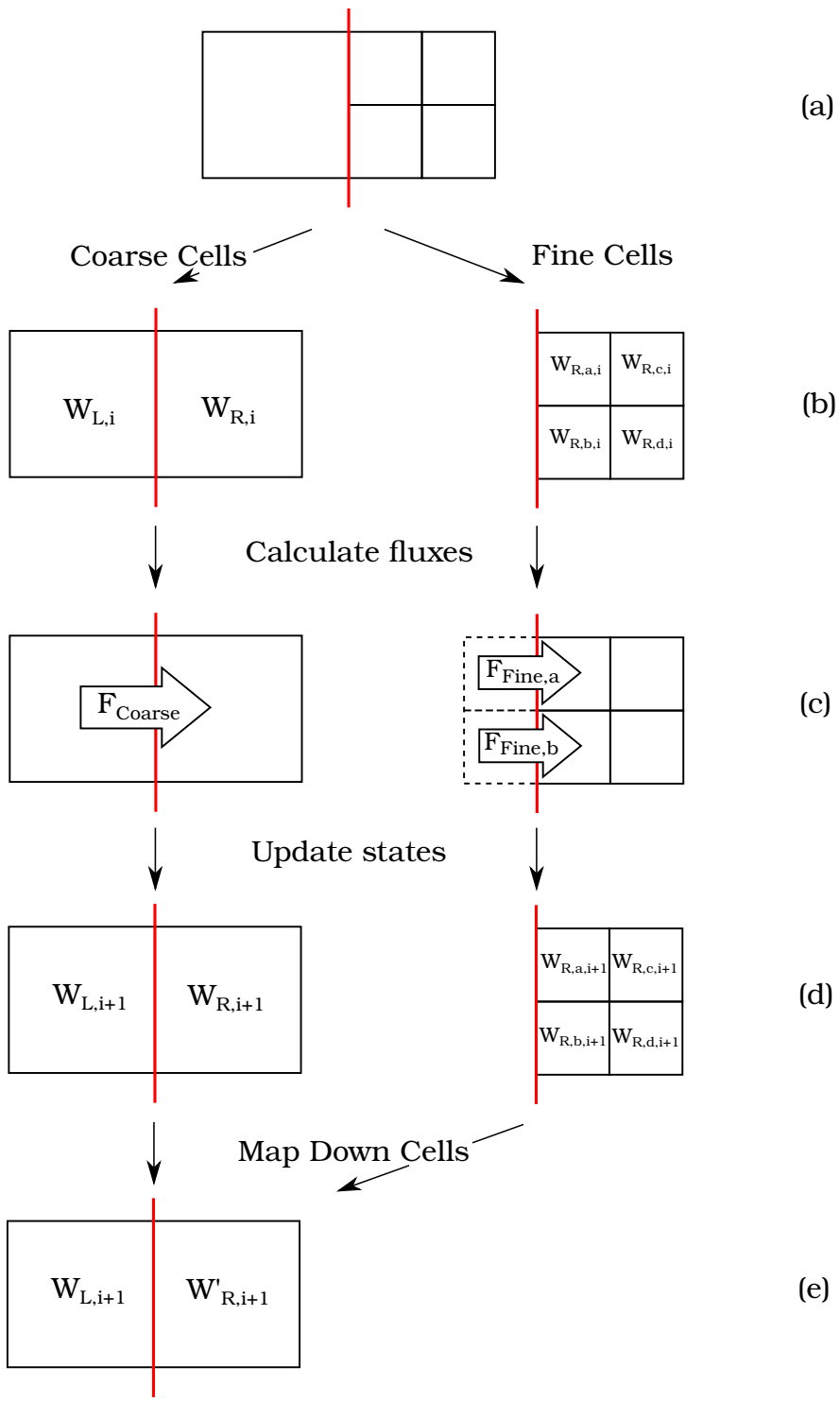

Figure 2.4: Scheme for updating coarse-fine boundaries in 2D. Red line shows the boundary of interest. The dashed cells are the temporary cells created from $W_{L,i}$ using PLM.

and to ensure mass, energy, etc. are conserved across the grid. The general scheme for calculating the flux across the coarse-fine boundary in 2D is as follows (shown in Figure 2.4). The boundary is bordered by two coarse cells and two fine cells (Figure 2.4b). The flux across coarse cells ($\boldsymbol{F}_{coarse}$) is calculated as normal (described in detail in Sec. 2.4). For the fine cells, the left state is temporarily split into two using PLM, giving two fluxes, one for each fine cell adjacent to the coarse fine boundary. As the fine cells are likely to have different results than the corresponding coarse cell this will ultimately lead to divergence of the solution across levels. To correct this, solutions of fine cells are mapped down to their parent cells, i.e,

$$\boldsymbol{W}'_{R,i+1} = \frac{1}{V_{coarse}} \sum_{n=a,b,c,d} \boldsymbol{W}_{R,n,i+1} V_{fine}, \tag{2.37}$$

where V_{coarse} and V_{fine} are the volumes of the coarse and fine cells respectively. As, in general, $\boldsymbol{F}_{coarse} \neq \boldsymbol{F}_{Fine,a} + \boldsymbol{F}_{Fine,b}$, the flux leaving $\boldsymbol{W}_{L,i+1}$ is not necessarily equal to the flux entering $\boldsymbol{W}'_{R,i+1}$. This can be fixed by correcting the flux,

$$\boldsymbol{W}'_{L,i+1} = \boldsymbol{W}_{L,i+1} + \Delta t(A_{Fine}\boldsymbol{F}_{Fine,a} + A_{Fine}\boldsymbol{F}_{Fine,b} - A_{Coarse}\boldsymbol{F}_{coarse}), \tag{2.38}$$

where Δt is the timestep and A_{Fine} and A_{Coarse} are the areas of the fine and coarse boundaries respectively. $\boldsymbol{W}'_{L,i+1}$ is then used in place of $\boldsymbol{W}_{L,i+1}$. This ensures that the flux is consistent across all levels and that conservation laws are not violated.

2.6 Grid initialisation

In order to actually run the hydrodynamic simulations presented in this thesis, a number of other ancillary tasks must be performed, including grid initialisation and data processing. These are achieved using custom code that I have written and exist independently of the main `MG` hydrocode.

For simple problems (such as the supernova presented in Chapter 5) only a simple analytic function is required to describe the initial conditions and so this can be simply embedded into the hydrocode's initialisation routine. For more complex initial conditions, where hydrostatic equilibrium has to be calculated numerically, this is not possible. The solution is to perform the integrations on a fixed grid first. As this only has to be performed once for each problem, and often can be done in axisymmetry, a far higher resolution than the main hydrodynamic simulation can be used. The result of this calculation is then stored in a data file, which can then be read by the hydrocode to initialise the grid. This ensures that the initial conditions are calculated accurately and consistently regardless of the resolution of the hydrodynamic simulation and provides a certain amount of flexibility if a different hydrocode needed to be used.

Table 2.1: Summary of features of major grid-based hydrocodes. Some features are omitted here (magnetic fields, self gravity etc.) as they are beyond the scope of this thesis. Note that some features may not be used in conjunction with one another. See individual method papers for specific implementation details.

Code	AMR	Spatial Reconstruction[7]	Time Integrator[8]	Riemann Solver[9]	Turbulence Model	Corner Transport	Language
`MG`	Cell Based	PLM	PC	Exact	k-ϵ	N	C++
`ATHENA`[1]	n/a[6]	PCM, PLM, PPM	CTU, MH	Exact, Force, Two-shock, HLLE, HLLC, Roe	N	Y	C
`ENZO`[2]	Patch Based	PPM	RK2	Exact, HLLC, HLL, LLF	N	N	C++
`FLASH`[3]	Paramesh, CHOMBO	PPM, WENO5	Explicit, MH	Roe, LLF, HLL, HLLC, Hybrid, Marquina	N	Y	Fortran
`PLUTO`[4]	CHOMBO	PCM, PLM, PPM, WENO5, LimO3	Explicit, RK2, RK3, MH	Exact, Roe, AUSM+, HLLC, HLL, TVDLF	N	Y	C, C++, Fortran
`RAMSES`[5]	Cell Based	PCM, PLM	Explicit	Exact, Acoustic, LLF, HLL, HLLC	N	N	Fortran

[1]Stone *et al.* (2008)
[2]Stone *et al.* (2008)
[3]Fryxell *et al.* (2000)
[4]Mignone *et al.* (2007), AMR Mignone *et al.* (2012)
[5]Teyssier (2002)
[6]Static refinement available
[7]PCM - Piecewise Constant Method, PLM - Piecewise Linear Method, PPM - Piecewise Parabolic Method (Colella & Woodward 1984), WENO3/WENO5 (Yamaleev & Carpenter 2009), LimO3 (Cada & Torrilhon 2009)
[8]PC - Predictor corrector, CTU - Corner Transport Upwind, MH - MUSCL-Hancock, RK2/3 - Runge Kutta 2nd/3rd order
[9]HLL - Harten-Lax-van Leer, HLLC - HLL with contact discontinuity, HLLE - HLL with Einfeldt fix, LLF - Local Lax-Friedrichs, TVDLF - Total Variation Diminishing Lax-Friedrichs

Chapter 3

Ram pressure stripping of galactic haloes

3.1 Introduction

As discussed in Section 1.1, galaxies can be ablated by the medium that they pass through, significantly affecting their evolution. The majority of studies on ram pressure stripping have been performed with SPH codes. While these can model the effect of instantaneous stripping, they are known to have difficulty resolving Kelvin-Helmholtz instabilities (KHIs) correctly (Agertz *et al.* 2007). Typically studies done with SPH codes show little to no Kelvin-Helmholtz stripping, whereas it is seen in studies done with grid based codes. However, grid based codes are also currently unable to reproduce the turbulence actually involved in ram pressure stripping. This chapter presents three-dimensional numerical simulations of the ram pressure stripping of the hot extended gaseous halo of a massive galaxy using the k-ϵ sub-grid turbulence model at Mach numbers 0.9, 1.1 and 1.9.

3.1.1 Turbulence model

The turbulent behaviour of a flow depends on its Reynolds number, $Re = ur/\nu$, where u is the velocity of the flow, r is the typical length scale of the flow and ν is the kinematic viscosity. For a fully ionized, non-magnetic gas of density ρ and temperature T, the kinematic viscosity

$$\nu = 2.21 \times 10^{-15} \frac{T^{5/2} A^{1/2}}{Z^4 \rho \ln\Lambda} \,\mathrm{cm^2\,s^{-1}}, \tag{3.1}$$

where A and Z are the atomic weight and charge of the positive ions and $\ln\Lambda$ is the coulomb logarithm (Spitzer 1956).

The Reynolds number of the ICM can be estimated using the above equations. Taking $v = 580\,\mathrm{km\,s^{-1}}$ as the flow speed past the galaxy, $r = 79\,\mathrm{kpc}$ as the characteristic size of the galaxy after instantaneous stripping, $\rho = 1.7 \times 10^{-28}\,\mathrm{g\,cm^{-3}}$ and $T = 10^7\,\mathrm{K}$ as the ICM density and temperature, $A \approx 1.0$, $Z \approx 1.0$ and $\ln\Lambda \approx 30$, gives $\nu \approx 1.35\,\mathrm{cm^2\,s^{-1}}$ and $Re \approx 100$ for the ICM gas for pure hydrodynamics.

However, the ICM contains a magnetic field, which is typically of order $1\,\mu$G (see, e.g., Carilli & Taylor 2002). If the thermal velocity is $\approx 5 \times 10^7\,\mathrm{cm\,s^{-1}}$ (appropriate for $10^7\,\mathrm{K}$ plasma), then the particle gyroradius $\approx 2.5 \times 10^{10}\,\mathrm{cm}$. Since this is small compared to the size of the largest turbulent eddies, the ions are constrained to move along the field. For the tangled fields that one would expect, this leads to a considerable reduction in the viscosity, which means that it can be safely assumed that the Reynolds number is high, certainly too large for direct numerical simulation.

The only tractable method to describe such flows is a statistical approach. I therefore use a subgrid turbulent viscosity model in an attempt to calculate the

properties of the turbulence and the resulting increase in the transport coefficients. The k-ϵ model used has been shown to give reasonable agreement with experiment for turbulent underexpanded jets with Mach numbers in the range $1-2$ and density contrasts ≈ 2 (Fairweather & Ranson 2006). This gives us some confidence in the the present simulations since both problems involve the growth of turbulent shear layers and the dimensionless parameters are not very different: the Mach numbers are similar, the density contrast in the galactic shear layer is ≈ 10 and the Reynolds numbers are large in both cases.

3.1.2 Numerical parameters

The numerical methods used in these simulations are detailed in Chapter 2. The maximum turbulent length scale (MTL) must be chosen on a case-by-case basis, which limits the size of the largest eddies. The predicted radius of the galaxy after instantaneous stripping, 120 kpc, is used as the appropriate value. Figure 3.1 shows the effect changing the MTL has on the rate of stripping of the galaxy. Halving the MTL has only a small effect, and doubling the MTL has almost no effect, therefore the rate of stripping within the model is robust. In these calculations the lowest level grid had 50 cells per side and spans a cubic region with sides of length 9.6 Mpc. There were 5 additional levels of refinement, giving a maximum resolution of 1600 cells per side, corresponding to a minimum mesh spacing of 6 kpc.

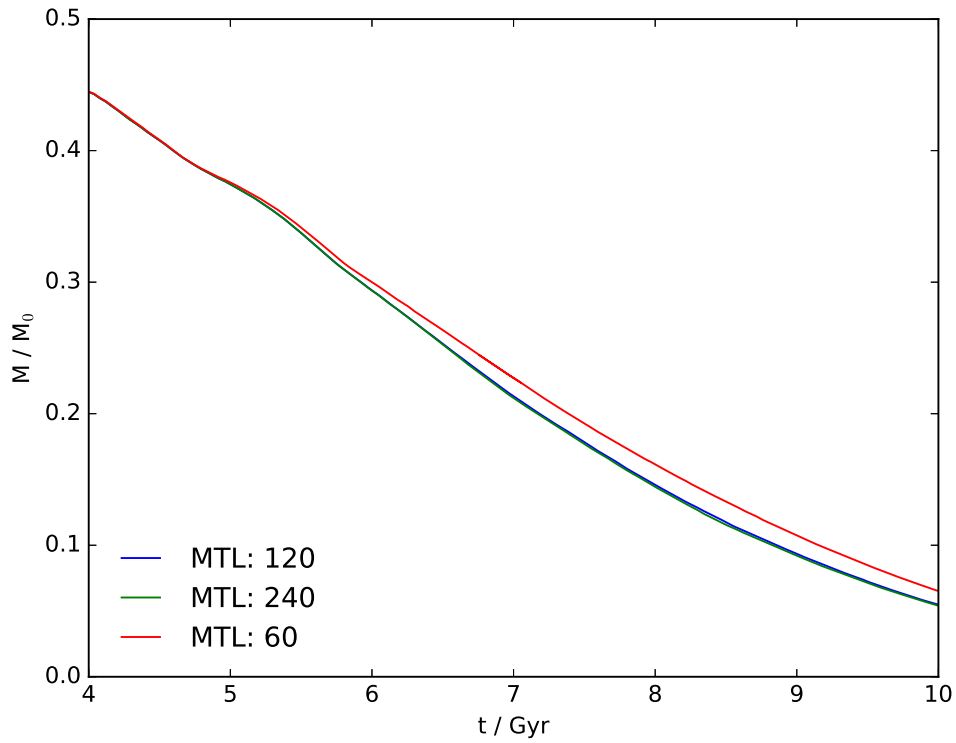

Figure 3.1: $M_{\mathrm{g,bound}}$ as a function of time for a Mach number of 1.9, showing the late-time behaviour of different values of MTL. The bound mass is identical for all values of MTL at times earlier than 4 Gyr.

Table 3.1: Galaxy model parameters

Variable	Value
M_{200}	$2 \times 10^{12}\,\mathrm{M}_{\odot}$
c_{200}	4
f_b	0.141
r_s	79kpc

Table 3.2: ICM parameters

Variable	Value
n_0	10^{-4} cm^{-3}
T_0	10^7 K
Mach number	0.9, 1.1, 1.9

Table 3.3: Parameters for the simulations. U_1 is the speed of the ICM relative to the galaxy. a_1 and a_2 are the sound speeds in the ICM and in the galaxy at the stripping radius, respectively. The temperature and sound speed of the hot halo increases with radius. ρ_2 is the gas mass density of the galaxy at the stripping radius, and ρ_1 is the density of the ICM. U_c is the predicted convective velocity of the gas in the shear-layer (Eq. 3.9). δ'_0 is the incompressible growth rate of the mixing layer (Eq. 3.8), π_c is a compressibility parameter (Eq. 3.10), $\delta'(\pi_c)/\delta'_0$ is the normalized growth rate (Eq. 3.11), and $\theta'(\pi_c)$ is the opening angle (Eq. 3.12). For the Mach 1.1 and 1.9 models, the ICM first passes through a bowshock upstream of the galaxy. The second line for each of these models therefore contains values computed with the free-streaming ICM conditions replaced by the conditions of the immediate post-shock flow on the symmetry axis. The stripping radius is assumed to be unchanged and therefore the values of a_2 and ρ_2 are not adjusted.

Model Mach No.	U_1 ($\mathrm{km\,s^{-1}}$)	Stripping radius (kpc)	a_1 ($\mathrm{km\,s^{-1}}$)	a_2 ($\mathrm{km\,s^{-1}}$)	ρ_2 ($\mathrm{g\,cm^{-3}}$)	ρ_2/ρ_1	U_c ($\mathrm{km\,s^{-1}}$)	δ'_0	π_c	$\frac{\delta'(\pi_c)}{\delta'_0}$	$\theta'(\pi_c)$ (°)
1.9	1000	120	526	320	4.6×10^{-28}	5.5	298	0.57	2.55	0.19	6.2
	460		733			2.5	346	0.44	1.17	0.39	9.8
1.1	580	202	526	380	1.4×10^{-28}	1.65	254	0.39	1.25	0.37	8.2
	504		550			1.44	232	0.37	1.08	0.42	8.9
0.9	470	236	526	425	0.9×10^{-28}	1.13	228	0.35	0.90	0.49	9.8

3.1.3 Initial conditions

The galaxy is taken to be comprised of a dark matter halo and a hot extended gas component. McCarthy *et al.* (2008) is followed for the dark matter and gas density distributions. A NFW distribution (Navarro, Frenk & White 1996) is used for the dark matter:

$$\rho(r)_{dm} = \frac{\rho_s}{(r/r_s)(1+r/r_s)^2}. \tag{3.2}$$

The characteristic density of the dark matter halo is

$$\rho_s = \frac{M_s}{4\pi r_s^3}, \tag{3.3}$$

where

$$M_s = \frac{M_{200}}{ln(1+c_{200}) - c_{200}/1+c_{200}}, \tag{3.4}$$

$c_{200} = r_{200}/r_s$ is the concentration parameter and $c_{200} = 4$ in accordance with McCarthy *et al.* (2007). r_{200} is the radius at which the average density is 200 times the critical density, $\rho_{crit} = 3H_0^2/8\pi G$. M_{200} is the mass within r_{200}. The dark matter is assumed to cause a static gravitational field. In the absence of tidal forces the dark matter distribution is not expected to be significantly altered; so a static field is justified. The dark matter extends to a radius of $r_{25} \approx 2.44\, r_{200}$.

The initial hot gas component was assumed to follow the dark matter distribution, such that

$$\rho_g(r) = f_b \rho_t(r), \tag{3.5}$$

where ρ_b is the gas density, ρ_t is the total density and $f_b = 0.022h^{-2}/0.3 = 0.141$ is the universal fraction of baryonic matter. The gas distribution of the galaxy is truncated at r_{200}. The temperature and density of the ICM were set to 10^7 K and $10^{-4}\,\mathrm{cm}^{-3}$. Hydrostatic equilibrium of the halo gas was assumed and determines the temperature and pressure distributions. The gas contained within r_{200} was given an advected scalar so that mass from the galaxy could be identified at later times. The total initial mass of the hot gaseous halo is 5.64×10^{11} $\mathrm{M}_\odot$. The galaxy was allowed to evolve in isolation with and without the k-ϵ model implemented and is stable for many Gyr.

The initial values of k and ϵ were set to $3\times10^{10}\,\mathrm{erg\,g^{-1}}$ and to $3\times10^{10}\,\mathrm{erg\,g^{-1}\,s^{-1}}$ respectively. As these values are several orders of magnitude lower than those subsequently generated during the interaction, the effect of the turbulent viscosity is dominated by the real turbulence at all times. Note that a positive feature of the k-ϵ model is its relative insensitivity to the initial conditions for k and ϵ (see e.g. Section 5.4.3 of Wilcox (2006)).

The ICM was given an initial velocity U_1 in the positive x direction to simulate the effects of the galaxy moving though it. The lower x boundary is set to drive the wind at the same speed throughout the simulation. In reality a galaxy falling into a cluster will see a gradual increase in wind speed. This will cause the instantaneous stripping phase to be drawn out over a longer period of time. By the onset of continual stripping however, enough time has passed ($\sim 2\,\mathrm{Gyr}$) that any shocks caused by the initial impact have dissipated. Three different velocities were used, corresponding to Mach numbers of 0.9, 1.1 and 1.9 ($U_1 = 470\,\mathrm{km\,s^{-1}}$, $580\,\mathrm{km\,s^{-1}}$ and $1000\,\mathrm{km\,s^{-1}}$ respectively). These values are typical of those in the literature and representative of the orbital speeds of a cluster galaxy. Simulations

for each different Mach number were performed with and without the k-ϵ model. Tables 3.1 and 3.2 summarise the setup parameters.

3.1.4 Parametrization of Galaxy Mass

In order to measure the mass of the gaseous component of the galaxy as a function of time, and hence the effectiveness of ram pressure stripping, the mass is tracked in four ways. $M_{\mathrm{g,r200}}$ is the mass of gas that was initially part of the galaxy and is within a distance of r_{200} of the galactic centre. $M_{\mathrm{g,unmixed}}$ is the mass of gas that was initially in the galaxy and that is in cells in which as least half of the gaseous material started the simulation in the galaxy. $M_{\mathrm{g,bound,gal}}$ is the mass of gas that was initially in the galaxy that is gravitationally bound to the dark matter potential. $M_{\mathrm{g,bound}}$ is the total mass of gas that is bound to the dark matter potential.

3.1.5 Effects of Resolution

In order to investigate the effects of resolution, the highest Mach number simulation is ran with one extra refinement level. The bound mass for these tests is shown in Figure 3.2. At early times both methods give similar results, which is not surprising since the instantaneous stripping is unaffected by turbulence. At later time the k-ϵ model converges, whereas there is no evidence of convergence in the inviscid runs. The inviscid calculations can be regarded as Implicit Large Eddy Simulations since the numerical algorithm has the required properties (Aspden *et al.* 2008), but such calculations are clearly not reliable unless one can achieve convergence. This has not been achieved although the resolution is

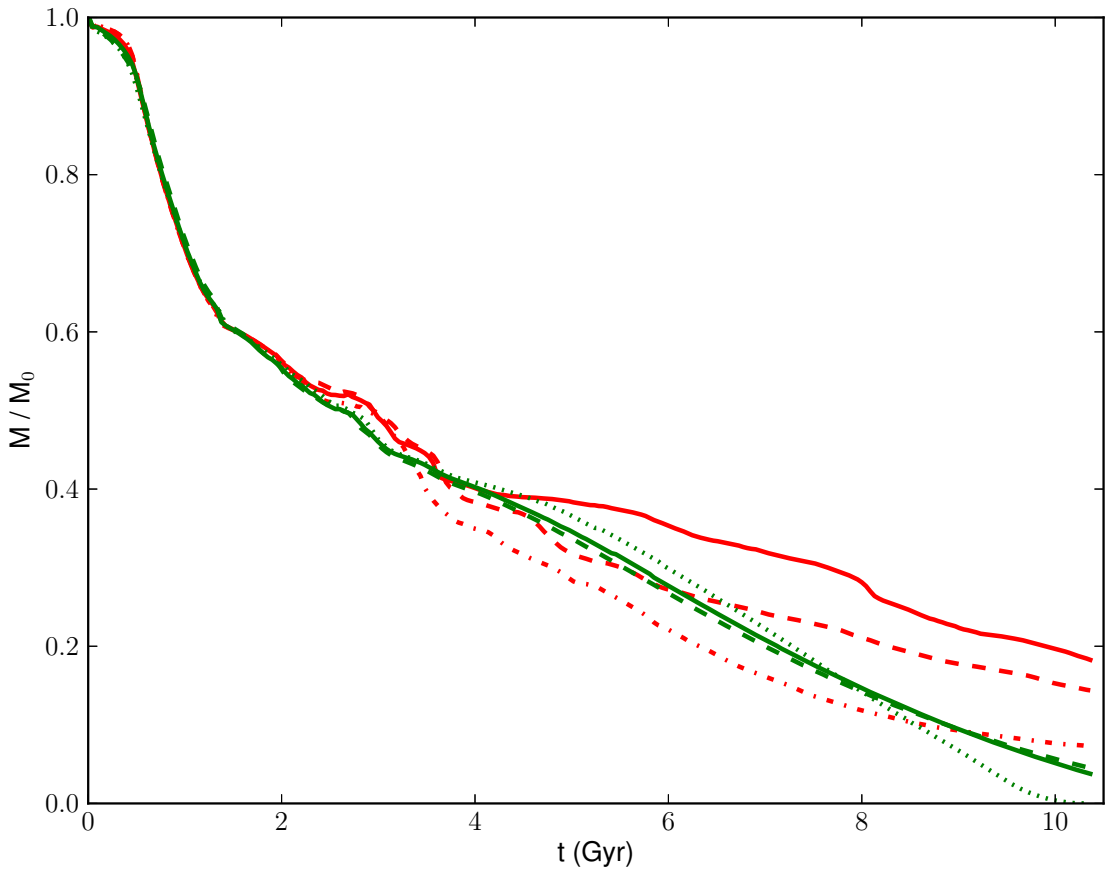

Figure 3.2: $M_{\rm g,bound}$ as a function of time for a Mach number of 1.9. The results for the model incorporating the k-ϵ model are shown in green. Those for the inviscid model are in red. The solid lines are for the standard resolution used throughout the rest of this study, the dashed lines are for the runs with an extra level of refinement, which allowed twice the maximum resolution and the dotted line uses one less refinement level, halving the maximum resolution. The dash-dotted line has two extra refinement levels, increasing the maximum resolution by a factor of 4 to 1.5kpc.

higher than in previous calculations such as Shin & Ruszkowski (2013).

The advantage of the k-ϵ model is that it converges at a resolution that can be used in practical calculations. Figure 3.2 also shows results for a run with one less refinement level using the k-ϵ model. At this resolution the results begin to diverge from the higher resolution runs.

3.2 Analytical Approximations

3.2.1 Instantaneous Stripping

Instantaneous stripping occurs when the ram pressure exceeds the gravitational force per unit area on a column of material. In McCarthy *et al.* (2008) an analytical prediction for the instantaneous ram pressure stripping of a spherically symmetric galaxy was derived, which extended work done by Gunn & Gott (1972). The condition for ram pressure stripping at a given radius, R, is,

$$\rho_{icm}\nu_{gal}^2 > \alpha\frac{GM_{gal}(R)\rho_{gas}(R)}{R}, \tag{3.6}$$

where α is a constant dependent on the dark matter and gas profiles. McCarthy *et al.* (2008) found that for their wind tunnel tests $\alpha \approx 2$ best fits their results. The stripping radius for each model is noted in Table 3.1.3. Note also the mass density and the sound speed of the hot gaseous galactic halo at this radius (ρ_2 and a_2 in Table 3.1.3, respectively).

3.2.2 Kelvin-Helmholtz Stripping

The rate at which mass is lost due to the Kelvin-Helmholtz instability was estimated by Nulsen (1982) to be

$$\dot{M}_{kh} = \pi r^2 \rho_{icm}\nu_{gal}. \tag{3.7}$$

Taking r as the radius after instantaneous stripping from equation (3.6) and using $1000\,\mathrm{km\,s^{-1}}$ as the velocity of the galaxy gives a mass loss rate of 49 $\mathrm{M_\odot\,yr^{-1}}$ for the assumed galaxy. At this rate the hot halo would be completely stripped in

4.4 Gyr. It might be expected that this is the rate at which mass is lost initially, but as mass is stripped the radius will decrease. One can assume that the mass-radius relation remains constant in order to calculate how the radius changes as mass is removed from the galaxy.

3.2.3 Compressible Turbulent Shear Layers

Turbulent shear layers are also of wide interest to the fluid-mechanics community and much study has been devoted to them. Brown & Roshko (1974) determined that the visual thickness of the shear layer spread as

$$\delta'_{\rm vis,0} = \frac{\delta(x)}{x - x_0} \approx 0.17 \, \frac{\Delta U}{U_{\rm c}}, \tag{3.8}$$

where $\delta(x)$ is the thickness of the mixing layer at a downstream distance of $x - x_0$ from the point where the streams initially interact, $\Delta U = U_1 - U_2$ is the velocity difference between the two free streams and $U_{\rm c}$ is the "convective velocity" at which large-scale eddies within the mixing layer are transported downstream. The constant 0.17 was empirically determined. When stream "2" is stationary,

$$U_{\rm c} = \frac{U_1}{1 + \left(\frac{\rho_2}{\rho_1}\right)^{1/2}}, \tag{3.9}$$

where the densities of the free streams are ρ_1 and ρ_2 (e.g., Papamoschou & Roshko 1988). A slightly more complicated form of Eq. 3.8 is noted in Soteriou & Ghoniem (1995).

It has long been recognized that the growth rate of compressible mixing layers is lower than predicted by Eq. 3.8 when the convective velocity is high. This

is attributed to compressibility effects. Papamoschou & Roshko (1988) showed that experimental measurements of the growth rate normalized by its incompressible value, δ'/δ'_0, was largely a function of the "convective Mach number", $M_{c,1} = (U_1 - U_c)/a_1$, where a_1 is the sound speed of free stream "1". More recently, Slessor *et al.* (2000) argue that the convective Mach number underrepresents compressibility effects for free streams with a significant density ratio, and show that a better characterisation is achieved through the use of an alternative compressibility parameter,

$$\pi_c = \max_i \left[\frac{\sqrt{\gamma_i - 1}}{a_i} \right] \Delta U, \tag{3.10}$$

where γ_i and a_i are the ratio of specific heats and the sound speed of free stream i. For $\pi_c \lesssim 3$, the normalized growth rate

$$\frac{\delta'(\pi_c)}{\delta'_0} \approx \left(1 + \alpha \pi_c^2\right)^{-1/2}. \tag{3.11}$$

The opening angle of the mixing layer is then

$$\theta'(\pi_c) = 2 \arctan\left(\frac{\delta'(\pi_c)}{2}\right). \tag{3.12}$$

3.3 Results

3.3.1 Wind tunnel tests

Figure 3.3 shows snapshots of the mass density distribution at a number of times for each of the runs. The k-ϵ runs agree relatively closely with their inviscid counterparts during the instantaneous stripping phase, but become increasingly

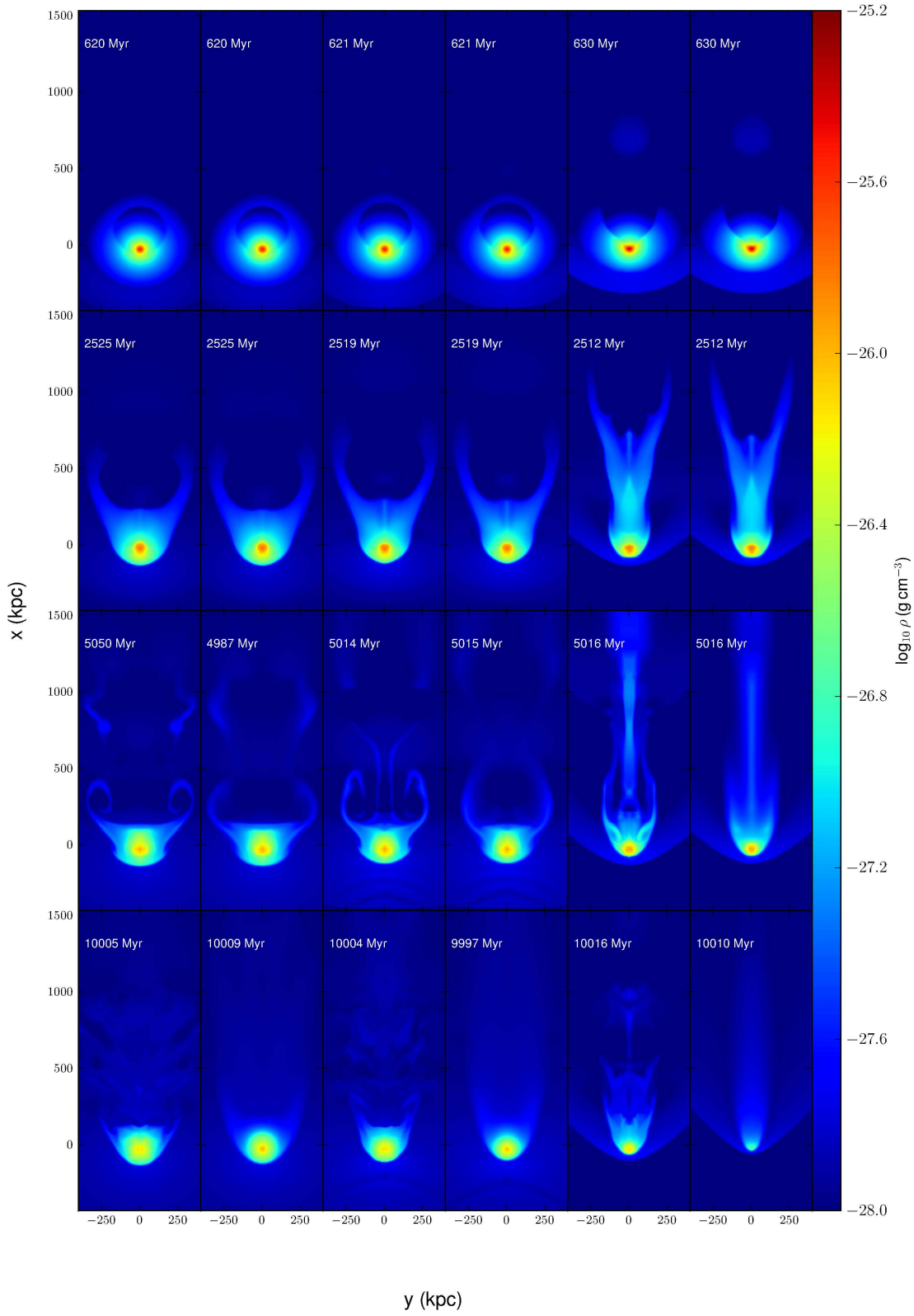

Figure 3.3: The mass density in the $z = 0$ plane. The first two columns contain results for simulations at a Mach number of 0.9, the second two results for a Mach number of 1.1 and the last two results for a Mach number of 1.9. The left column in each pair shows results for the inviscid simulations, while the right column in each pair gives results for models that incorporate the k-ϵ model.

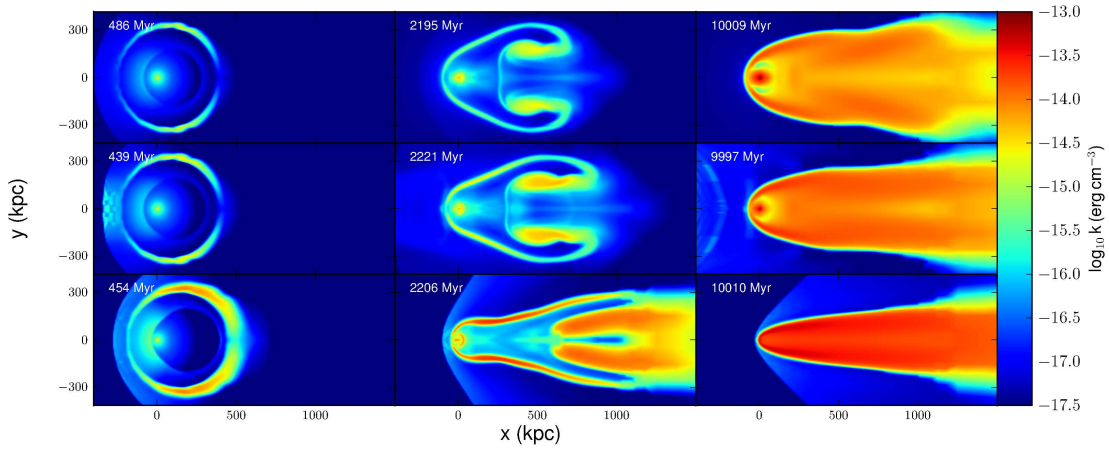

Figure 3.4: The distribution in the $z = 0$ plane of turbulent energy, k, for simulations incorporating the k-ϵ model. Rows correspond to, from the top, Mach numbers of 0.9, 1.1 and 1.9. The three times are: during instantaneous stripping, after instantaneous stripping and at the end of the simulation.

divergent at later times when the Kelvin-Helmholtz instability is most important. The largest difference between the inviscid and k-ϵ simulations are seen in the Mach 1.9 run. The results for runs incorporating the k-ϵ model look smoother in general as the density given is a local mean density.

Figure 3.4 shows the distribution of turbulent energy for each k-ϵ run. The turbulence is initially produced at the interface between the galaxy and the ICM. There is also turbulence in the tail after instantaneous stripping, as seen in the central column of panels. This is initially generated during instantaneous stripping and is advected downstream. At later times the turbulence generated at the galaxy-ICM interface has managed to propagate into and fill the tail. Some of the turbulence in the tail also moves back towards the galaxy. The general trend of increased turbulence at higher Mach numbers is apparent. This is shown quantitatively in Figure 3.5. At sonic and marginally supersonic Mach numbers the turbulent energy rises gradually with time after an initial delay of $\sim 2\,\mathrm{Gyr}$

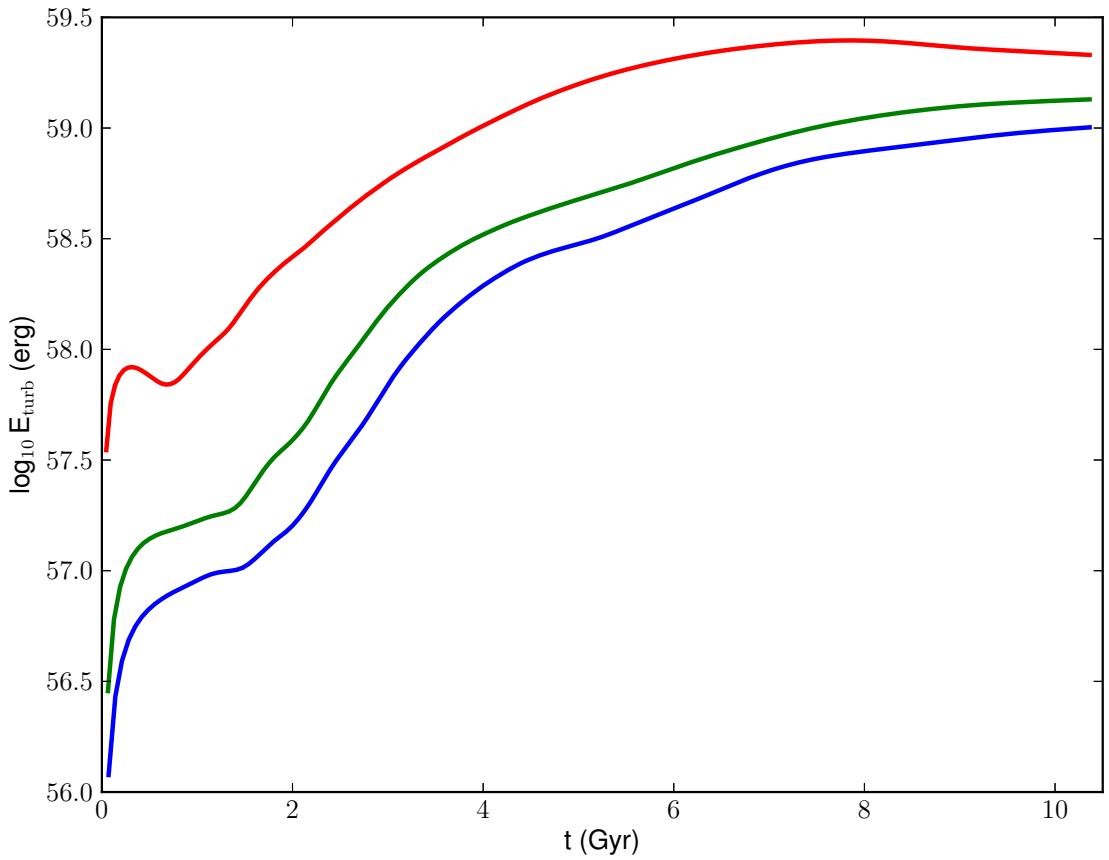

Figure 3.5: The total turbulent energy, $E_{\rm turb}$, across the entire grid. The blue, green and red lines give results for the simulations with Mach numbers of 0.9, 1.1 and 1.9 respectively. The turbulent energy obtained by integrating ρk across the entire volume.

while instantaneous stripping is occurring. The total turbulent energy peaks at $\sim 8\,$Gyr in the highest Mach number simulation as turbulence begins to be advected from the grid. The typical value of the turbulent diffusivity in the shearing layers is $\mu_T \sim 3 \times 10^{28}\,{\rm cm^2 s^{-1}}$ (as defined by Equation 2.8).

Figure 3.6 shows each of the different ways the mass of the galaxy is tracked, as described in Section 3.1.4. In the first $\sim 2\,$Gyr gas is removed where gravity is weak enough to be overcome by ram pressure, and $M_{g,bound,gal}$ (red) and $M_{\rm g,r200}$ decreases. $M_{\rm g,unmixed}$ (green) remains relatively constant during this pe-

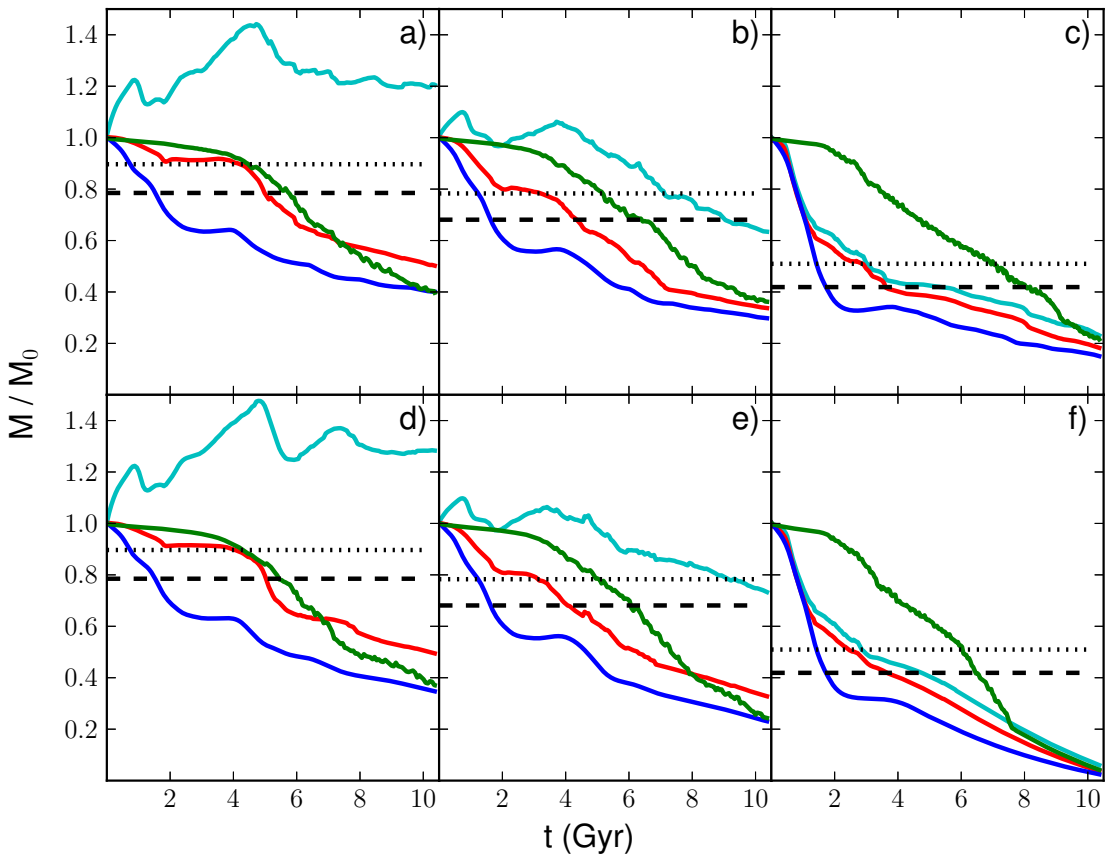

Figure 3.6: Gaseous component of the galaxy mass as a function of time for all six simulations. Results for inviscid runs are shown in a-c, and results for runs incorporating the k-ϵ model in d-f. Columns correspond to, from the left, Mach numbers of 0.9, 1.1 and 1.9. The blue line shows $M_{\mathrm{g,r200}}$, the green line shows $M_{\mathrm{g,unmixed}}$, the red line shows $M_{\mathrm{g,bound,gal}}$ and the cyan line shows $M_{\mathrm{g,bound}}$. The black dashed line is the analytical prediction from equation (3.6) with $\alpha = 2$. The black dotted line gives the result for the same equation but for $\alpha = 3$.

riod, showing that the ram pressure is not mixing the gases, but rather pushing it from the galaxy, as might be expected. This occurs on a time-scale equal to the sound crossing time (1.8 Gyr). It should be noted that in the transonic cases much of the ICM component of $M_{\mathrm{g,bound}}$ is in front of the galaxy and is still part of the flow. For example, in the Mach 0.9 case (shown in Figure 3.7), the wind speed is equal to the escape velocity at $\sim$170 kpc, so gas within this radius is

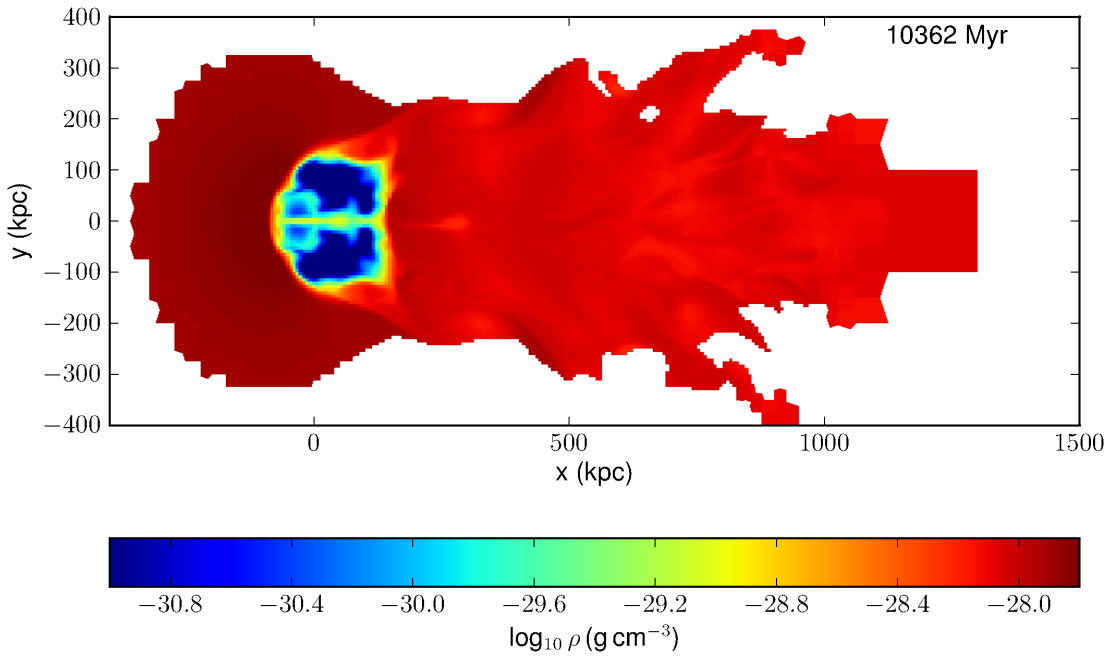

Figure 3.7: The distribution of gas that started the simulation as ICM and is bound to the dark matter potential, for the 0.9 Mach number model incorporating the k-ϵ model. In the blue area the gas bound to the galaxy is mostly gas that was associated with the galaxy initially.

technically bound but is being constantly pushed downstream due to the flow of the wind behind it. After this the galaxy enters a transitional period where little to no mass is stripped from the galaxy, particularly at lower Mach numbers. The galaxy then begins to be stripped by the Kelvin-Helmholtz instability until the end of simulation and the mass associated with the galaxy decreases.

The general shape of the curves is the same in all cases (with the exception of $M_{\mathrm{g,bound}}$, as noted above). The lengths of the instantaneous stripping and transitional periods appear independent of Mach number, with the transitional period being more pronounced at lower Mach numbers. In general stripping is stronger at higher Mach numbers. In all cases the galaxy loses more mass than predicted due to instantaneous stripping alone. This means that Kelvin-Helmholtz stripping is

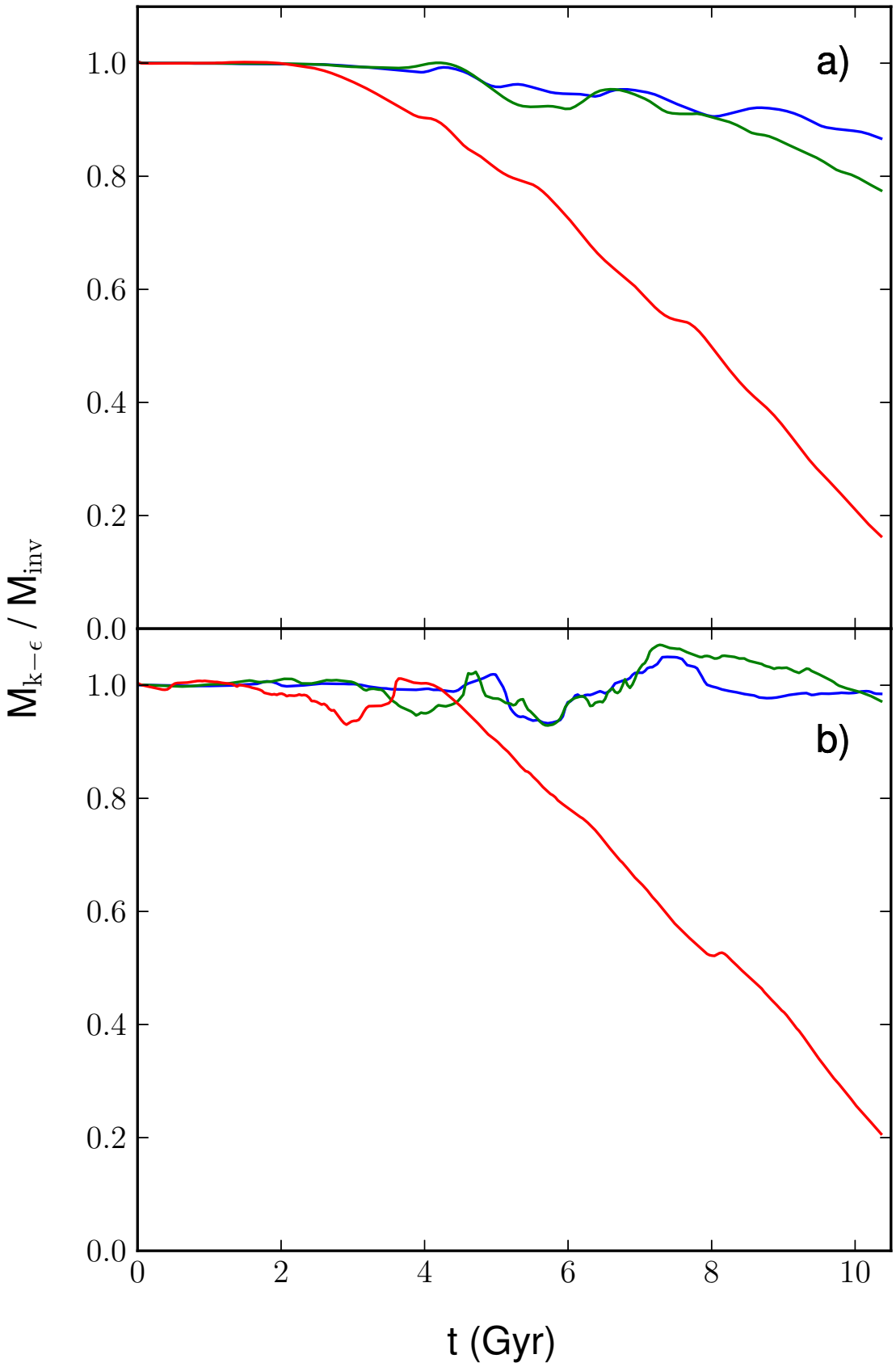

Figure 3.8: Ratio of the mass of the galaxy in k-ϵ runs over the corresponding inviscid run. The top panel shows $M_{\mathrm{g,r200}}$, while the bottom panel $M_{\mathrm{g,bound,gal}}$. The blue, green and red lines correspond to Mach numbers of 0.9, 1.1 and 1.9 respectively.

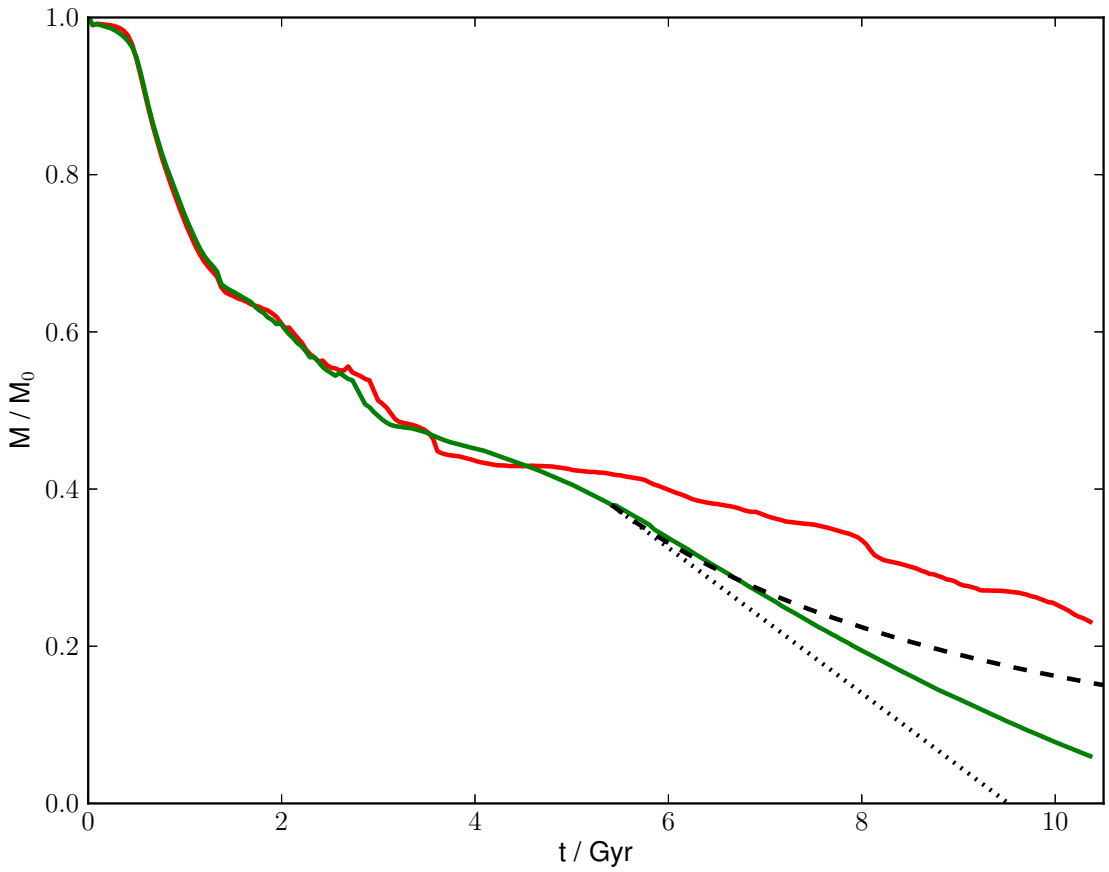

Figure 3.9: $M_{\rm g,bound}$ as a function of time for a Mach number of 1.9. Shown in green is the run incorporating the k-ϵ model and in red is the inviscid run. The black dotted line shows the prediction from equation (3.7), assuming a constant radius. The black dashed line shows the same equation but allowing the radius to change over time.

significant on the 10 Gyr time-scales investigated. The simulations incorporating the k-ϵ model differ the most from the corresponding inviscid simulation at the highest Mach number (Figure 3.6c and 3.6f), particularly in the late-time Kelvin-Helmholtz stripping phase, when the turbulence is fully developed.

Figure 3.8 shows the difference in mass stripping between the inviscid and the k-ϵ simulations in more detail. While there is little difference in $M_{\rm g,bound,gal}$ at the transonic Mach numbers (but some difference in $M_{\rm g,r200}$), at supersonic Mach numbers there is significantly more stripping when the k-ϵ model is used. For

the Mach 1.9 case, $M_{\rm g,r200}$ and $M_{\rm g,bound,gal}$ are both only 20% of the mass in the inviscid model at late times.

Figure 3.9 shows the simple analytical predictions of equation (3.7) for a Mach number of 1.9. The galaxy undergoes a transitional period between the instantaneous and Kelvin-Helmholtz phases. Thus the time at which the results should follow the analytic prediction is unclear. For any chosen starting point after $\sim 5\,$Gyr both curves fit the simulation well initially and slowly diverge away. This suggests that although the simulation strips at a rate which is similar to the analytical prediction, the formula is an over simplification of the time dependence of the radius.

Table 3.1.3 notes predicted values for the convective velocity, $U_{\rm c}$, for each simulation. However, it is not possible for us to easily compare simulation results presented here to this value because these simulations provide us with the mean local velocity instead, and this changes across the mixing layer from the undisturbed galactic halo gas to the unmixed ICM gas flowing past. In addition, Papamoschou & Bunyajitradulya (1997) show that predictions for the convective Mach number and the convective velocity need correcting if the mixing is not "symmetric". For these reasons the opening angle of the mixing layer is focused on instead. The predicted opening angles for the Mach 0.9 model and the post-shock-adjusted predictions for the Mach 1.1 and 1.9 models yield $\theta'(\pi_{\rm c}) \approx 10^\circ$. This compares with the observed angle of about 10°-15° estimated from Fig. 3.5, and is also consistent with the results of Canto & Raga (1991) (see also the end of section 4.2 in Pittard *et al.* 2009). This level of agreement is perfectly acceptable given that those simulations differ in some notable respect to those presented here. For instance, in this work i) the mixing layer is not flat but instead curves

around the galaxy; ii) the ICM gas does not stream past the galaxy at a steady velocity (it is nearly stationary close to the stagnation point of the flow upstream of the galaxy and accelerates around the galaxy); iii) the gas experiences gravitational forces from the galaxy. These differences affect the opening angle of the mixing layer by less than a factor of two.

3.3.2 Comparison to previous works

McCarthy *et al.* (2008) investigated ram pressure stripping of a hot galactic halo with the SPH code `GADGET-2`. The bound mass of the simulations presented here after instantaneous stripping lies above what one would expect from equation (3.6) using the $\alpha \sim 2$ value that they determined from their results, particularly at lower Mach numbers, which they did not investigate. The method they used for calculating bound mass is fundamentally different from the one used here (due to the differences in SPH and grid-based codes) and they discussed this in appendix A of their paper. They found that implementing the same bound mass calculation as used here increases the amount of mass bound after instantaneous stripping suggesting that this could be the reason for the discrepancy between the results. The results are more consistent with $\alpha = 3$, as shown in Figure 3.6. They noted that instantaneous stripping occurs on time-scales comparable to the sound crossing time of the galaxy, which is what is found here. They did not however see any mass loss after the instantaneous stripping period, in contrast to these results.

Bekki (2009) included a disc in the galaxy in addition to a halo and used the SPH code `GRAPE-SPH`. He only conducted two-body tests (i.e. no wind tunnel

tests) so a direct comparison with these results is not possible. However he remarked that his results are broadly consistent with those of McCarthy *et al.* (2008). He also does not see any continual stripping after the initial mass loss.

Most recently Shin & Ruszkowski (2013) used the grid-based code `FLASH3` to study ram pressure stripping of elliptical galaxies. They measured the mass of their galaxy by measuring the mass within radial zones and so their results are most comparable with the $M_{\mathrm{g,r200}}$ calculations. They look specifically at subsonic galaxy speeds (Mach number of 0.25) so these results are not necessarily directly comparable but the same broad pattern is seen: quick, instantaneous stripping, followed by a plateau and then continual stripping to the end of simulation.

3.4 Conclusion

This chapter presents a study of the effects of ram pressure stripping on the halo of a massive galaxy using three dimensional hydrodynamic simulations incorporating the k-ϵ sub-grid turbulence description. The Mach number of the interaction is varied to investigate its effect.

In all cases the Kelvin-Helmholtz instability contributes significantly to the stripping of material from the galaxy. This is captured both with and without use of the k-ϵ model at transonic Mach numbers. During instantaneous stripping the simulations incorporating the k-ϵ model produces the same results as simulations in which it is not used. However at higher Mach numbers (i.e. 1.9) Kelvin-Helmholtz stripping is only properly captured when the k-ϵ model is used.

This means that the stripping of gas from hot gaseous haloes has been underestimated in previous simulations particularly those in which the galaxy Mach

number is about two or more. Since it is currently not feasible to accurately model fully developed turbulence in this problem, the incorporation of a sub-grid turbulence model, such as the k-ϵ model, is highly desirable.

Chapter 4

Galactic disks and the limits of the k - epsilon model

4.1 Introduction

Rotationally supported disks, such as those seen in spiral galaxies, are a common feature in astrophysics, the long term stability of which is important for the evolutionary characteristics of these objects. Galaxies in clusters are known to undergo ram pressure stripping (Gunn & Gott 1972; Roediger 2009), a process that removes gas from the galaxy due to the relative motion between it and the intra-cluster medium (ICM). The removal of gas can have the effect of quenching star formation and reddening the galaxy. This is observed in the differences between cluster and isolated galaxies that do not undergo this process (Goto *et al.* 2003; Gómez *et al.* 2003; Balogh *et al.* 2004). Direct observations have shown the large effect ram pressure stripping can have on a galaxy's gas content (Vollmer *et al.* 2012), star formation (Abramson & Kenney 2014; Jáchym *et al.* 2014)

and morphology (Paolillo *et al.* 2002; Abramson *et al.* 2011), even dramatically influencing the most massive galaxy clusters (Ebeling *et al.* 2014).

As shown in Chapter 3 the use of a subgrid turbulence model is desirable when studying the ablation of objects, such as ram pressure stripping. There is a potential problem however, as the differential rotation in the galaxy produces a shear within the disk. Shear forces are the drivers of turbulence and are represented in the k-ϵ model in the turbulent production term (Equation 2.10). Due to the complexities of the model it is unclear what effect this turbulence model has on the galaxy. This forms the basis of investigation for this chapter.

4.2 Hydrostatic equilibrium

In order for the galaxy to be stable it must satisfy the conditions for hydrostatic equilibrium. Galaxies are typically rotational supported radially and pressure supported vertically. This gives the conditions:

$$\frac{1}{\rho}\frac{\partial p}{\partial R} + \frac{\partial \Phi}{\partial R} = \frac{V^2}{R}, \tag{4.1}$$

and

$$\frac{1}{\rho}\frac{\partial p}{\partial z} + \frac{\partial \Phi}{\partial z} = 0. \tag{4.2}$$

In order to satisfy Equation 4.2 either the temperature or the density distribution must be given. This leads to two general approaches to satisfying these equations, discussed next.

4.2.1 Explicit temperature distribution

The first approach is to specify the temperature distribution of the galaxy and calculate the density structure required to satisfy Equation 4.2. Assuming an equation of state $p = c^2\rho$, and that the galaxy is initially isothermal, Equation 4.2 is solved by:

$$\rho(R,z) = \rho_0(R)\exp\left(\int_0^{\mathrm{z}} \frac{\mathrm{g_z(R,z')}}{\mathrm{c_s^2}}\mathrm{dz'}\right). \tag{4.3}$$

Given the mid-plane density, ρ_0, the rest of the density distribution can be calculated via numerical integration. In order to find a suitable mid-plane density, typically a surface density profile is specified as this is easily observable in real galaxies. An exponential profile is commonly used:

$$\Sigma(R) = \Sigma_0\exp(-\mathrm{R}/\mathrm{R_d}), \tag{4.4}$$

where Σ_0 is the surface density at the galactic centre and is chosen to give the required total gas mass. The central density is then chosen such that after integration of Equation 4.3 the surface density matches that specified in Equation 4.4. In practice this is done by a process of iteration, choosing an arbitrary central density, calculating the resulting surface density then adjusting the central density appropriately.

As the grid resolution is limited, only an approximation can be made to the ideal hydrostatic structure. As shown in Figure 4.1 the vertical structure is not represented well in the centre of the galaxy, as the galaxy becomes only a few cells thick. The consequence of this is a relaxation into a slightly different equilibrium where the centre of the galaxy is thickened. As this is no worse an approximation

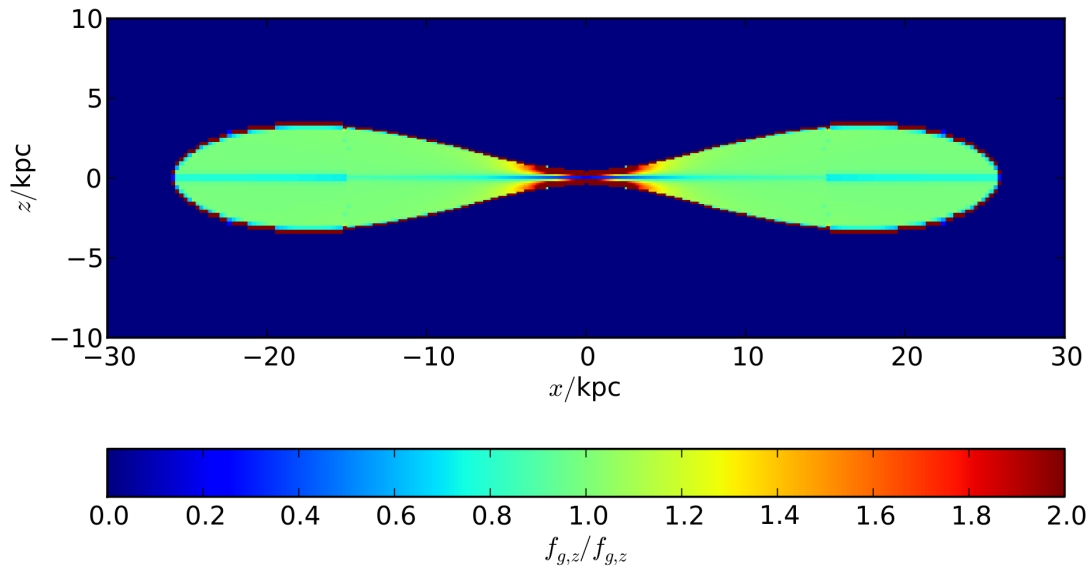

Figure 4.1: The ratio of the force due to the pressure gradient to the gravitational force in the z direction at $t = 0\,\mathrm{Myr}$

to a real galaxy than the ideal equilibrium, this is not necessarily an issue.

4.2.2 Explicit density distribution

The second approach is to specify the density distribution. A simple, common choice is the exponential disk:

$$\rho(R,z) = \frac{M_{gas}}{2\pi a_{gas}^2 b_{gas}} \exp\left(\frac{-\mathrm{R}}{\mathrm{a_{gas}}}\right) \exp\left(\frac{-\mathrm{z}}{\mathrm{b_{gas}}}\right), \tag{4.5}$$

where M_{gas} is the total gas mass and a_{gas} and b_{gas} define scale lengths in the radial and vertical directions respectively. The problem with this distribution is the sharp peak in density is somewhat unphysical and difficult to reproduce on a finite grid. This can be fixed by slighting modifying the density distribution to a

softened exponential disk (e.g. Roediger & Brüggen (2006)):

$$\rho(R,z) = \frac{M_{gas}}{2\pi a_{gas}^2 b_{gas}} 0.5^2 \mathrm{sech}\left(\frac{\mathrm{R}}{\mathrm{a_{gas}}}\right) \mathrm{sech}\left(\frac{|\mathrm{z}|}{\mathrm{b_{gas}}}\right). \tag{4.6}$$

It should be noted that the softening reduces the total integrated mass and it is no longer equal to M_{gas}. Equation 4.3 can be rearranged to give

$$\frac{\partial p}{\partial z} = g\rho, \tag{4.7}$$

which can be integrated numerically to obtain the pressure distribution. Note that some gravitational fields diverge at $z = 0$ meaning $p(z = 0)$ cannot be used as a boundary condition. Instead the ambient medium can be used to set the external pressure boundary. This is perhaps more reasonable as it is easier to obtain estimates for the temperature and density of the ICM than that in the centre of a galaxy.

4.2.3 Velocity distribution

Once the density and the temperature distributions have been determined, the velocity structure can be calculated quite simply from Equation 4.1, as all other parameters are now known.

4.3 Turbulence in cylindrical coordinates

In the k-ϵ model the effect of turbulence on the fluid is governed by the turbulent stress tensor, $\boldsymbol{\tau}$. The turbulent stress tensor can be written as:

$$\tau_{ij} = \mu_T 2S_{ij} - \frac{2}{3}\delta_{ij}(\rho k + \mu_T \nabla \cdot \boldsymbol{u}), \tag{4.8}$$

where S_{ij} is the rate of strain tensor and can be written in general as:

$$S_{ij} = \frac{1}{2}\left(\hat{\boldsymbol{i}} \cdot \frac{\partial \boldsymbol{u}}{\partial x_j} + \hat{\boldsymbol{j}} \cdot \frac{\partial \boldsymbol{u}}{\partial x_i}\right). \tag{4.9}$$

In cylindrical coordinates:

$$\begin{aligned} \partial x_0 &= \partial r, \\ \partial x_1 &= r\partial\theta, \\ \partial x_2 &= \partial z, \end{aligned} \tag{4.10}$$

and

$$\boldsymbol{u} = u_r\hat{\boldsymbol{r}} + u_\theta\hat{\boldsymbol{\theta}} + u_z\hat{\boldsymbol{z}}. \tag{4.11}$$

Using these equations with Equation 4.9 the rate of strain tensor can be represented in cylindrical coordinates. For example, the normal strain in the θ

direction:

$$\begin{aligned} S_{\theta\theta} &= \hat{\boldsymbol{\theta}} \cdot \frac{1}{r}\frac{\partial \boldsymbol{u}}{\partial \theta} \\ &= \hat{\boldsymbol{\theta}} \cdot \frac{1}{r}\left(\frac{\partial (u_r \hat{\boldsymbol{r}})}{\partial \theta} + \frac{\partial (u_\theta \hat{\boldsymbol{\theta}})}{\partial \theta} + \frac{\partial (u_z \hat{\boldsymbol{z}})}{\partial \theta}\right) \\ &= \hat{\boldsymbol{\theta}} \cdot \frac{1}{r}\left(\hat{\boldsymbol{r}}\frac{\partial u_r}{\partial \theta} + u_r \frac{\partial \hat{\boldsymbol{r}}}{\partial \theta} + \hat{\boldsymbol{\theta}}\frac{\partial u_\theta}{\partial \theta} + u_\theta \frac{\partial \hat{\boldsymbol{\theta}}}{\partial \theta} + \hat{\boldsymbol{z}}\frac{\partial u_z}{\partial \theta} + u_z \frac{\partial \hat{\boldsymbol{z}}}{\partial \theta}\right) \\ &= \hat{\boldsymbol{\theta}} \cdot \frac{1}{r}\left(\hat{\boldsymbol{r}}\frac{\partial u_r}{\partial \theta} + u_r \hat{\boldsymbol{\theta}} + \hat{\boldsymbol{\theta}}\frac{\partial u_\theta}{\partial \theta} - u_\theta \hat{\boldsymbol{r}} + \hat{\boldsymbol{z}}\frac{\partial u_z}{\partial \theta}\right) \\ &= \frac{1}{r}\frac{\partial u_\theta}{\partial \theta} + \frac{u_r}{r}, \end{aligned} \tag{4.12}$$

using the fact that $\frac{\partial \hat{\boldsymbol{r}}}{\partial \theta} = \hat{\boldsymbol{\theta}}$, $\frac{\partial \hat{\boldsymbol{\theta}}}{\partial \theta} = -\hat{\boldsymbol{r}}$ and $\frac{\partial \hat{\boldsymbol{z}}}{\partial \theta} = 0$. Following the same procedure for all the components of $\boldsymbol{S}$, and eliminating some terms due to the disk's axisymmetry ($\frac{\partial \boldsymbol{u}}{\partial \theta} = 0$) and circular velocity ($u_z = u_r = 0$) the rate of strain tensor becomes:

$$\boldsymbol{S} = \frac{1}{2}\begin{bmatrix} 0 & \frac{1}{r}\frac{\partial u_\theta}{\partial r} + \frac{u_r}{r} & 0 \\ \frac{1}{r}\frac{\partial u_\theta}{\partial r} + \frac{u_r}{r} & 0 & \frac{\partial u_\theta}{\partial z} \\ 0 & \frac{\partial u_\theta}{\partial z} & 0 \end{bmatrix}. \tag{4.13}$$

For certain types of disk $\frac{\partial u_\theta}{\partial z} = 0$. However this term is left in here as this is not true in the general case. The divergence of the velocity field is

$$\nabla \cdot \boldsymbol{u} = \frac{1}{r}\frac{\partial (r u_r)}{\partial r} + \frac{1}{r}\frac{\partial u_\theta}{\partial \theta} + \frac{\partial u_z}{\partial z}. \tag{4.14}$$

For circular rotation, $u_r = u_z = \frac{\partial u_\theta}{\partial \theta} = 0$, and therefore,

$$\nabla \cdot \boldsymbol{u} = 0. \tag{4.15}$$

Combining Equations 4.8, 4.13 and 4.15 the turbulent stress tensor becomes:

$$\boldsymbol{\tau} = \begin{bmatrix} -\frac{2}{3}\rho k & \mu_T\left(\frac{\partial u_\theta}{\partial r} + \frac{u_\theta}{r}\right) & 0 \\ \mu_T\left(\frac{\partial u_\theta}{\partial r} + \frac{u_\theta}{r}\right) & -\frac{2}{3}\rho k & \mu_T\left(\frac{\partial u_\theta}{\partial z}\right) \\ 0 & \mu_T\left(\frac{\partial u_\theta}{\partial z}\right) & -\frac{2}{3}\rho k \end{bmatrix}. \tag{4.16}$$

The turbulent stress tensor influences the momentum of the fluid through its divergence, as shown in Equation 2.2. This equation represents 3 independent equations, one for each spatial dimension. For example, for the z dimension:

$$\frac{\partial \rho u_z}{\partial t} + \nabla \cdot (\rho u_z \boldsymbol{u}) + \frac{\partial P}{\partial z} - \nabla \cdot \boldsymbol{\tau}_z = \rho g_z, \tag{4.17}$$

where $\boldsymbol{\tau}_z = (\tau_{zr}, \tau_{z\theta}, \tau_{zz})$. Using Equation 4.16 the divergence of $\boldsymbol{\tau}_z$ becomes

$$\begin{aligned} \nabla \cdot \boldsymbol{\tau}_z &= \frac{1}{r}\frac{\partial}{\partial r}\left[r \cdot 0\right] + \frac{1}{r}\frac{\partial}{\partial \theta}\left[\mu_T \frac{\partial u_\theta}{\partial z}\right] + \frac{\partial}{\partial z}\left[-\frac{2}{3}\rho k\right] \\ &= -\frac{2}{3}\frac{\partial \rho k}{\partial z} \end{aligned} \tag{4.18}$$

The z momentum equation can then be written:

$$\frac{\partial \rho u_z}{\partial t} + \nabla \cdot (\rho u_z \boldsymbol{u}) + \frac{\partial (P + \frac{2}{3}\rho k)}{\partial z} = \rho g_z. \tag{4.19}$$

It is clear that the turbulent energy acts as a positive pressure. If $2/3\rho k$ is a significant fraction of the thermal pressure it could disrupt the hydrostatic equilibrium.

Table 4.1: Disk galaxy model parameters

Variable	Value
M_{star}	$10^{11}\,\mathrm{M}_{\odot}$
a_{star}	4.0 kpc
b_{star}	0.25 kpc
M_{bulge}	$10^{10}\,\mathrm{M}_{\odot}$
r_{bulge}	0.4 kpc
M_{gas}	$10^{10}\,\mathrm{M}_{\odot}$
a_{gas}	7.0 kpc
b_{gas}	0.4 kpc
M_{200}	$10^{12}\,\mathrm{M}_{\odot}$
c_{200}	12

4.4 Initial conditions

A massive disk galaxy is modelled. The galaxy is comprised of a gaseous disk and a static gravitational field, with dark matter and stellar components. The gravitational field is built from three analytical components representing the dark matter halo, stellar disk and stellar bulge. Roediger & Brüggen (2006) is followed for these profiles, with the exception of the dark matter halo.

Roediger & Brüggen (2006) use the dark matter distribution from Burkert (1995):

$$\rho(r)_{dm,MB} = \frac{\rho_d r_0^3}{(r + r_0)(r^2 + r_0^2)}, \tag{4.20}$$

where ρ_d is the central density and r_0 defines a radial length scale. Instead, a NFW distribution (Navarro *et al.* 1996) is used for the dark matter:

$$\rho(r)_{dm,NFW} = \frac{\rho_s}{(r/r_s)(1 + r/r_s)^2}. \tag{4.21}$$

The characteristic density of the dark matter halo is

$$\rho_s = \frac{M_s}{4\pi r_s^3}, \tag{4.22}$$

where

$$M_s = \frac{M_{200}}{\ln(1+\mathrm{c}_{200}) - \mathrm{c}_{200}/(1+\mathrm{c}_{200})}, \tag{4.23}$$

and $c_{200} = r_{200}/r_s$ is the concentration parameter. We take $c_{200} = 12$ and $M_{200} = 10^{12}\,\mathrm{M}_\odot$. The Burkert profile is designed to reproduce the rotation curves of dwarf galaxies, specifically those with core masses from 10^6 to $10^{10}\,\mathrm{M}_\odot$(Mori & Burkert 2000), whereas the dark matter haloes of massive disk galaxies are typically of the order of 10^{11} to $10^{12}\,\mathrm{M}_\odot$. The gravitational force can be calculated from the density distribution as

$$\frac{\partial\Phi}{\partial r} = g(r) = -\frac{GM(r)}{r^2}, \tag{4.24}$$

where $M(r)$ is the integrated mass:

$$M(r) = \int_0^r 4\pi r'^2 \rho(r')dr'. \tag{4.25}$$

For the NFW dark matter distribution, this gives:

$$g_{dm}(r) = \frac{GM_s}{r^2}\left[\frac{r/r_s}{1+r/r_s} - \ln(1+\mathrm{r}/\mathrm{r_s})\right]. \tag{4.26}$$

This can be decomposed into R and z components in order to calculate hydrostatic equilibrium.

The stellar disk is modelled as a Plummer-Kuzmin disk (Miyamoto & Nagai 1975), with a gravitational potential:

$$\Phi_{s,disk}(R,z) = \frac{-GM_{star}}{\{R^2 + [a_{star} + (z^2 + b_{star}^2)^{1/2}]^2\}^{1/2}}, \tag{4.27}$$

with the mass of the stellar disk $M_{star} = 4 \times 10^{10}\,\mathrm{M}_\odot$, and shape parameters

$a = 3.5\,\mathrm{kpc}$ and $b = 0.2\,\mathrm{kpc}$.

The stellar bulge is a spherically symmetric Hernquist bulge (Hernquist 1993):

$$\Phi_{s,bulge}(r) = \frac{-GM_{bulge}}{r + r_{bulge}}, \tag{4.28}$$

with mass of the bulge, $M_{bulge} = 10^{10}\,\mathrm{M}_\odot$ and scale radius, $r_{bulge} = 0.4\,\mathrm{kpc}$.

The density and temperature distributions of the galaxies are determined using the method described in Section 4.2.2 using $M_{gas} = 10^{10}\,\mathrm{M}_\odot$, $a_{gas} = 7.0\,\mathrm{kpc}$ and $b_{gas} = 0.4\,\mathrm{kpc}$. The galaxy parameters are summarised in Table 4.1. The ambient medium has a density of $10^{-28}\,\mathrm{g\,cm^{-3}}$ and a temperature of $10^7\,\mathrm{K}$.

4.5 Simulations

4.5.1 Isolation - with and without k-ϵ

First, the galaxy is evolved both with and without the k-ϵ model. In the k-ϵ the initial values of k and ϵ are set uniformly across the grid to $10^5\,\mathrm{cm^2\,s^{-2}}$ and to $6.91 \times 10^{-6}\,\mathrm{cm^2\,s^{-3}}$ respectively. The exact values of k and ϵ are not too important as the k-ϵ model is relatively insensitive to the initial conditions for k and ϵ (see e.g. Section 5.4.3 of Wilcox (2006)).

The evolution of the density distribution is shown in Figure 4.2. The inviscid disk has a slight readjustment in its hydrodynamic equilibrium in the first $\sim$ 500 Myr and then remains stable for the next several Gyr. The k-ϵ model however, has a huge impact on the disk which expands continuously, predominately in the z-direction over the entire 7.5 Gyr simulation.

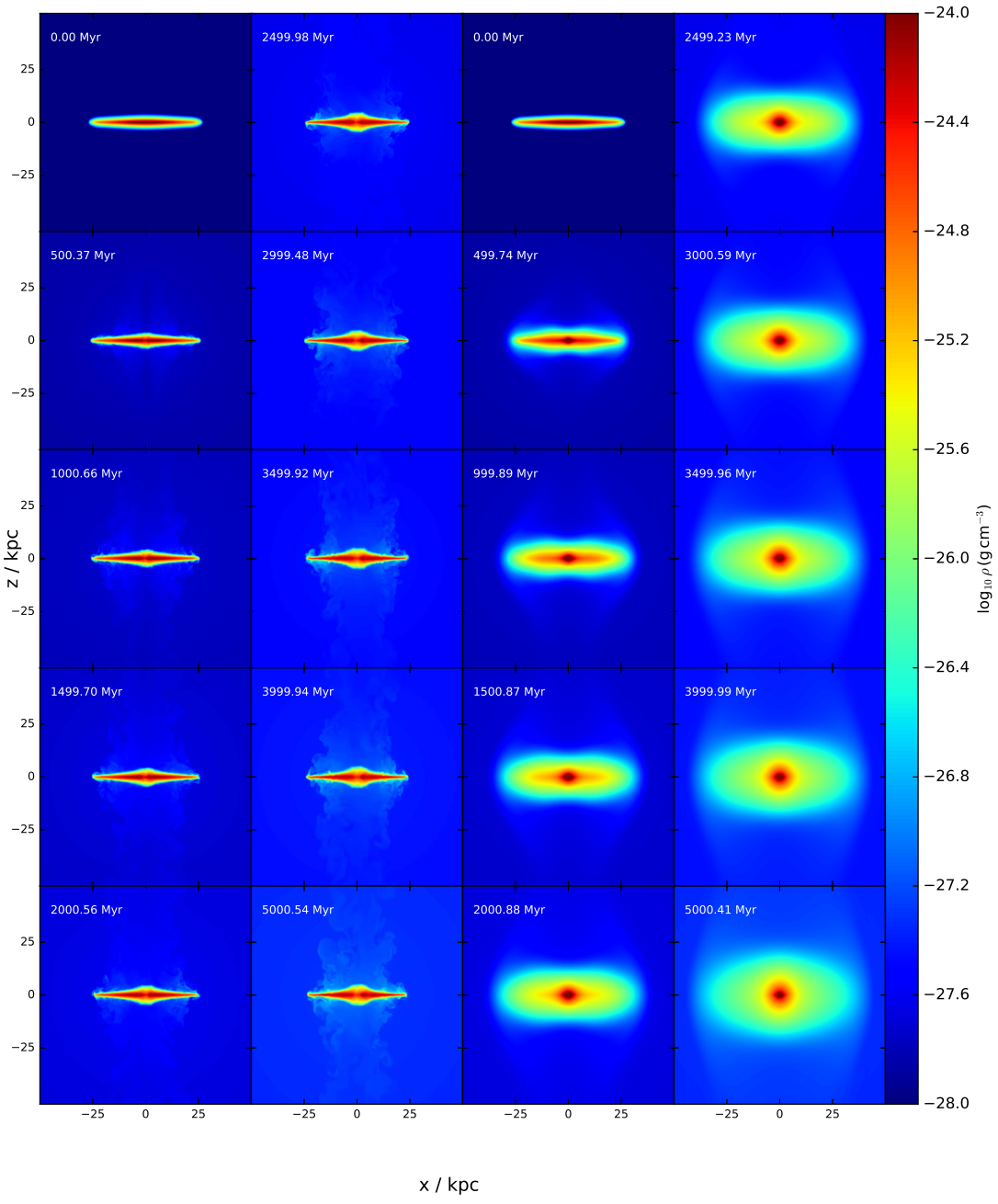

Figure 4.2: Gas density as shown in a slice though $y = 0$, for the galaxy in isolation. The left two columns shows the inviscid run and the right two columns shows the run using the k-ϵ model.

4.5.2 k-ϵ tests

There are a number of possible explanations for the behaviour of the k-ϵ model under these conditions. This section outlines these possibilities and presents simulations to test them.

4.5.2.1 Uniform ρk

In the k-ϵ simulation the initial turbulent energy per mass (k) is set uniformly, meaning that the turbulent energy per volume (ρk) is much higher in the central regions of the disk. As this value acts somewhat like a pressure (see Equation 4.19) this could potentially upset the hydrodynamic equilibrium and cause expansion of the disk. The k and ϵ values are initialised such that the turbulent energy per volume (ρk) is uniform across the grid, keeping the value of k the same at the origin.

Figure 4.3 shows the turbulent energy per volume for both cases. While the values are quite different initially, the turbulence generated quickly dominates and is the same in both cases. This is reflected in the density distribution shown in Figure 4.4 where the same expansive behaviour is seen in both cases. The ambient medium still retains a high value when a uniform $k\rho$ is used, however, as it is the gradient of the turbulent energy that is important, this has no impact on the evolution of the simulation.

4.5.2.2 No turbulent heating

In the k-ϵ model the turbulent energy is dissipated into the internal energy of the fluid. This turbulent heating of the fluid could potentially cause inflation of

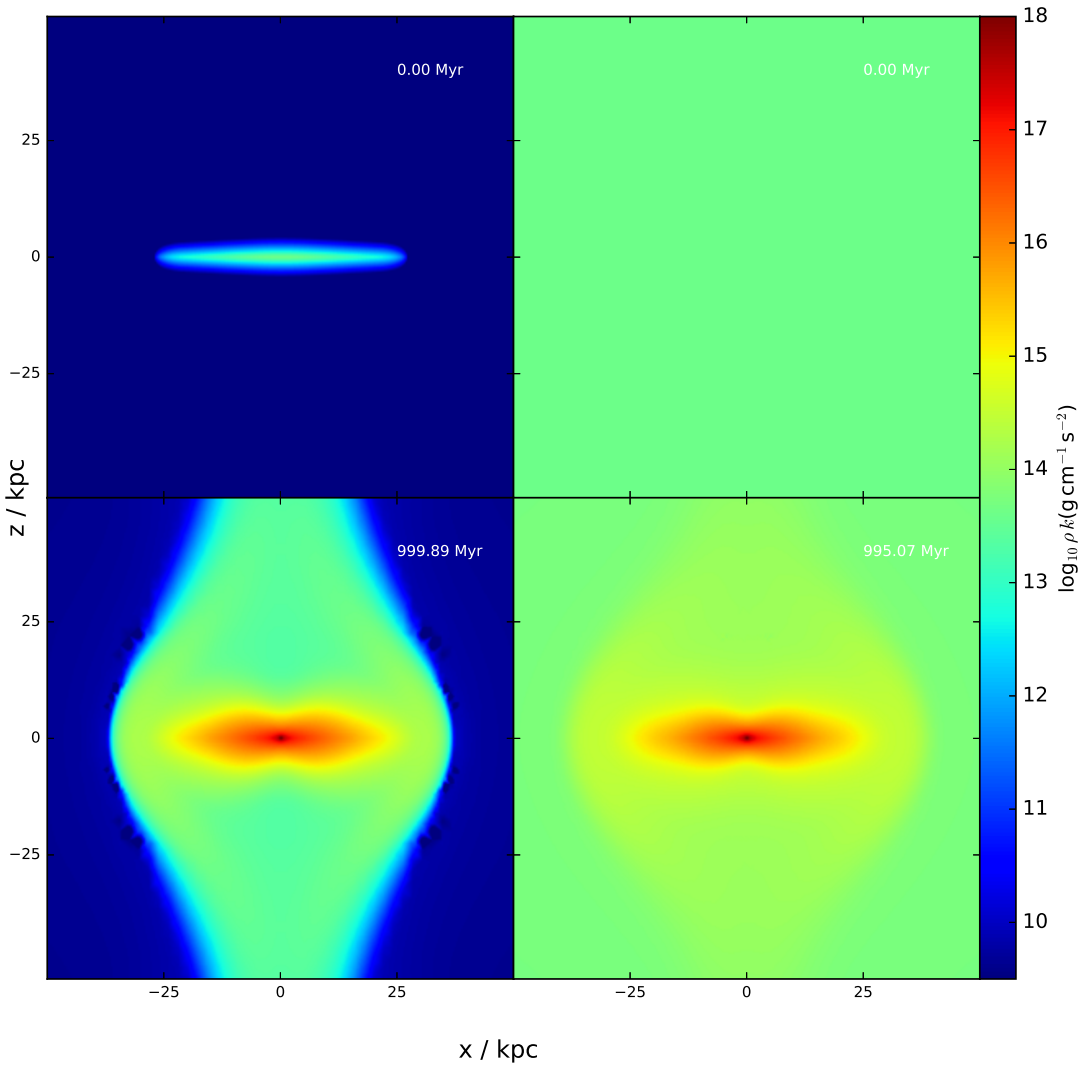

Figure 4.3: ρk shown in a slice though $y = 0$. The left column shows the unmodified original k-ϵ results (as shown in Figure 4.2), the right column shows the simulation with initially uniform turbulent energy per unit volume (ρk). Shown at the start of the simulation (top) and at $t =\sim 1\,\mathrm{Gyr}$ (bottom).

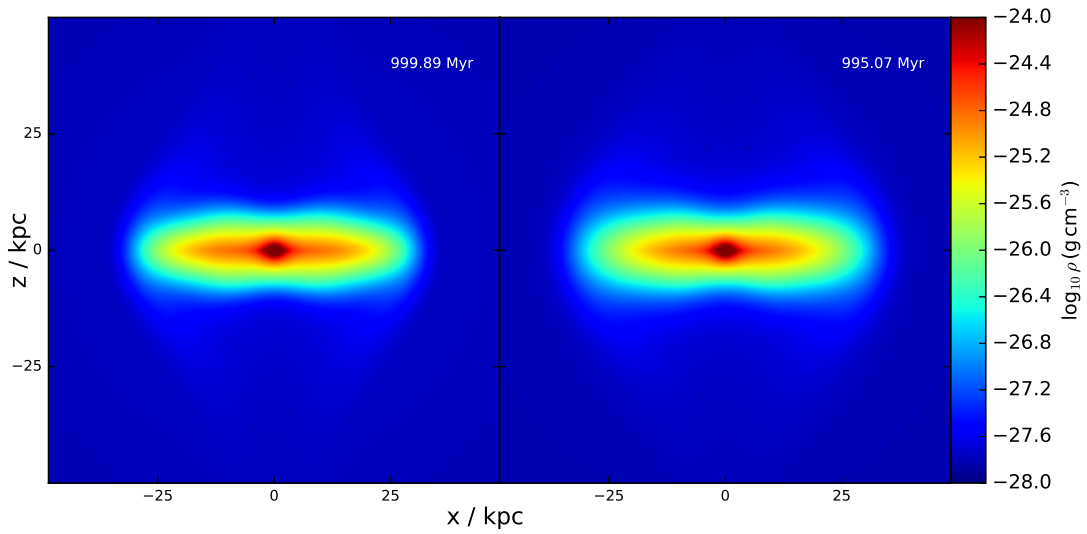

Figure 4.4: Gas density shown in a slice though $y = 0$ at $t = \sim 1\,\mathrm{Gyr}$. The left panel shows the unmodified original k-ϵ results (as shown in Figure 4.2), the right panel shows the simulation with initially uniform turbulent energy per unit volume (ρk).

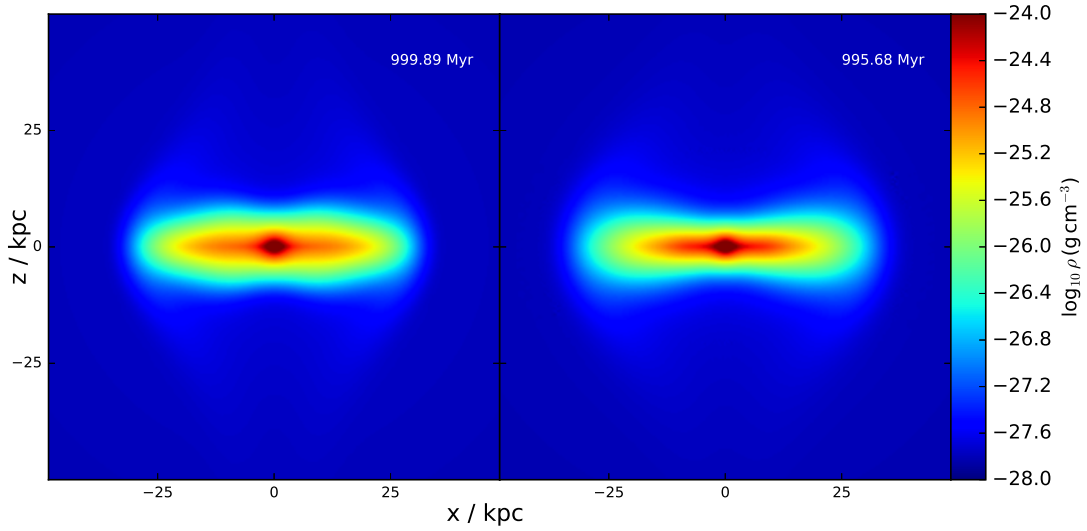

Figure 4.5: As Figure 4.4 but the right panel shows the simulation without turbulent heating.

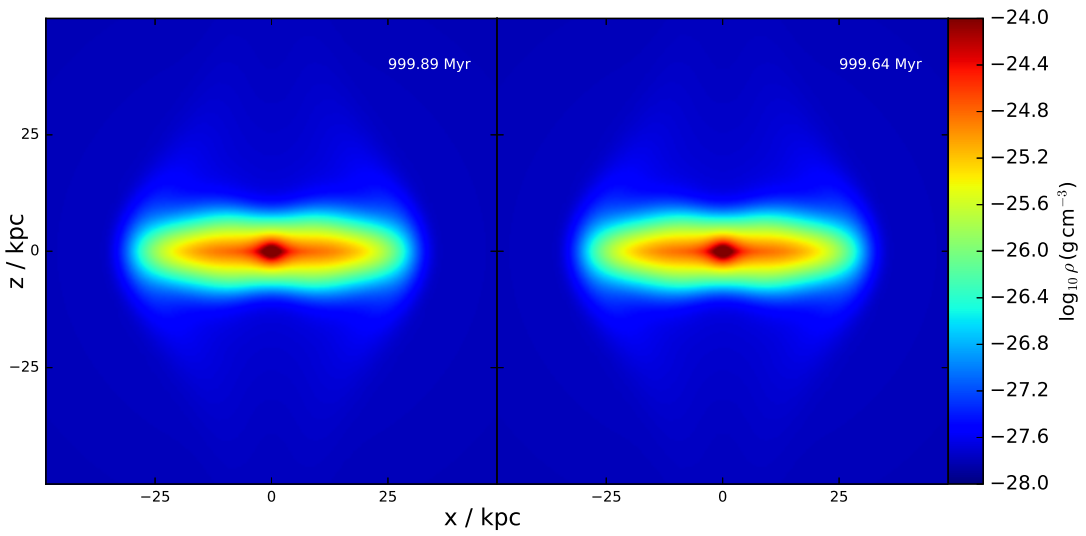

Figure 4.6: As Figure 4.4 but the right panel shows the simulation without off-diagonal terms in the turbulent stress tensor.

the disk. The equation that governs energy conservation, Equation 2.3, has the the turbulent heating term, $\rho\epsilon$, removed. This is as if the turbulent energy is efficiently radiated away instead of being used to heat the galaxy. While there is not necessarily any physical justification for this behaviour it should be able to show whether turbulent heating is responsible for the expansion of the disk.

Figure 4.5 shows the impact on the density distribution when turbulent heating is removed. Without turbulent heating the gas is slightly cooler and this is reflected in the slight reduction in the extent of the expansion, particularly in the centre of the galaxy, although some other factor that is causing the galaxy to expand is still dominating.

4.5.2.3 Eliminating off-diagonal terms in the turbulent stress tensor

It has been noted previously (e.g. Gauthier & Bonnet (1990); Scannapieco & Brüggen (2010)) that in the presence of shocks the off-diagonal strain terms

Table 4.2: Dwarf disk galaxy model parameters

Variable	Value
M_{star}	$3 \times 10^8\,\mathrm{M}_\odot$
a_{star}	0.7 kpc
b_{star}	0.2 kpc
M_{bulge}	0
M_{gas}	$2 \times 10^8\,\mathrm{M}_\odot$
a_{gas}	0.7 kpc
b_{gas}	0.2 kpc
M_{200}	$10^{10}\,\mathrm{M}_\odot$
c_{200}	12

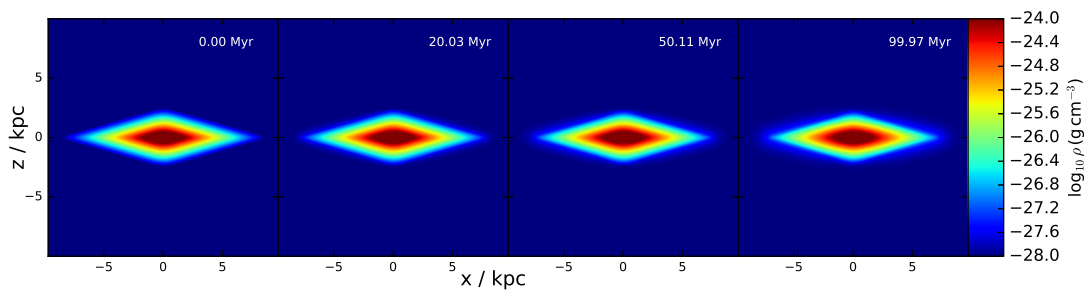

Figure 4.7: Gas density as shown in a slice though $y = 0$, for the dwarf disk galaxy in isolation.

$(\partial u_i/\partial x_j + \partial u_j/\partial x_i$, where $i \neq j)$ can become unphysically large. Figure 4.6 shows a comparison of the galaxy with and without off-diagonal terms after $\sim 1\,\mathrm{Gyr}$. There is no perceivable difference.

4.5.2.4 Dwarf disk galaxy

The use of a turbulence model is fairly rare in astrophysical simulations. The only previous application of a turbulence model to a rotating disk comes from Scannapieco & Brüggen (2010) where they do not see any such expansive effects. Their investigation differs to the one in this chapter in three important ways. They neglect off-diagonal strain terms, they use a k-L model (modelling the turbulent length scale as opposed to the turbulent dissipation rate) and they

model a dwarf galaxy as opposed to a massive galaxy. As shown in Section 4.5.2.3 the off-diagonal strain terms have no impact on the expansive behaviour. In order to differentiate between the effects of the turbulence model and the area of parameter space, a galaxy with the same parameters as theirs is simulated in isolation using the k-ϵ model. The parameters used are shown in Table 4.2.

Figure 4.7 shows the evolution of the dwarf galaxy under the k-ϵ model. It is completely stable for the 100 Myr simulated (Scannapieco & Brüggen (2010) show 60 Myr of evolution). This suggests that it is the area of parameter space, rather than the specific turbulence model that is the significant factor. The massive galaxy rotates at up to Mach 15 where as the dwarf galaxy rotates up to Mach 4 which could be the relevant difference. It is also possible that it is just the shorter timescale that is responsible, and if the dwarf galaxy were to be evolved for 1 Gyr or more it would become inflated by the generated turbulence. Either way, the dwarf galaxy provides a small region of parameter space where a turbulence model might be used.

4.5.3 Modified hydrostatic equilibrium

Another possibility is that the condition of hydrostatic equilibrium (Equation 4.2) does not account of the effects of turbulence. Using the modified momentum equation (Equation 4.19) results in the hydrostatic equation:

$$\frac{1}{\rho}\frac{\partial(p+\frac{2}{3}\rho k)}{\partial z}+\frac{\partial\Phi}{\partial z}=0. \tag{4.29}$$

This is not enough however, as k and ϵ both need to be put into equilibrium distributions. However, calculating this analytically is non-trivial. A more prag-

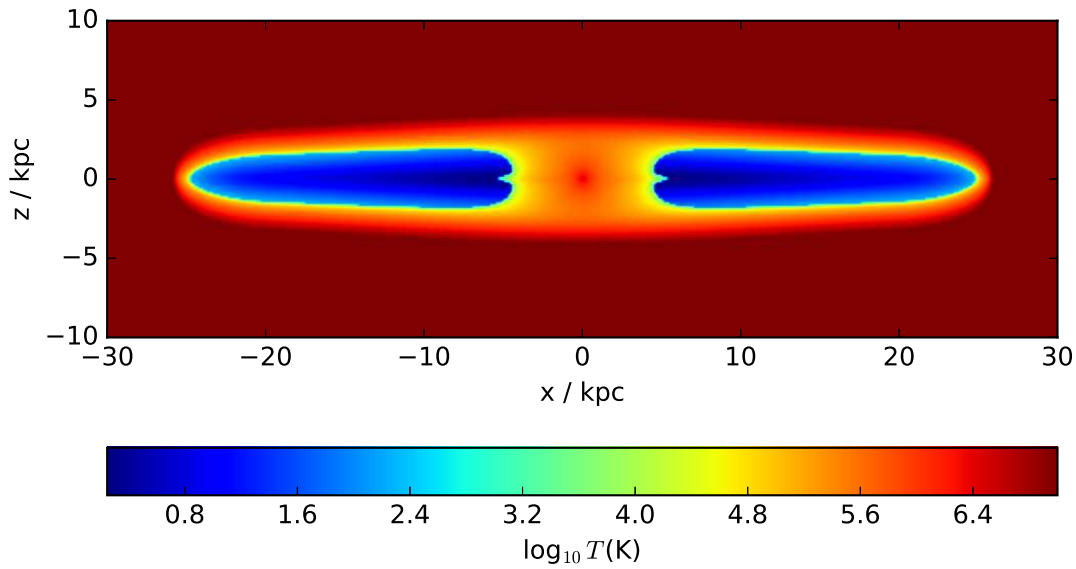

Figure 4.8: Initial temperature as shown in a slice though $y = 0$, for the massive disk galaxy using the modified hydrostatic equilibrium.

matic approach would be to use the k and ϵ distributions from the end of the previous simulations (seen in Figure 4.3). These distributions are almost certainly not correct given the difference in density distributions but should give some indication as to the viability of this approach given the amount of turbulence that is produced. Figure 4.8 shows the resulting initial temperature distribution. In order to counteract the turbulence the temperature has to drop to unphysical levels. This shows that the amount of turbulence generated is too high to be contained with reasonable alterations to the hydrostatic equilibrium and is likely a flaw in the turbulence model.

4.6 Alternate turbulence models

It has been recognised within the engineering literature that the standard k-ϵ has numerous short comings, including poor predictions for flows with strong separation, rotating/swirling flows and adverse pressure gradients (see e.g. Menter 1994; Pope 2000; Wilcox 2006). This has lead to many attempts to improve upon it, such as dynamic renormalization group (RNG) k-ϵ (Yakhot & Orszag 1986) and later the realizable k-ϵ model (Shih *et al.* 1995). Both these models aim to improve upon the standard k-ϵ model by improving, amongst other things, the prediction of rotating flows, which is very relevant to the simulations presented here.

Each different model performs better for particular flows and have different parameters to be calibrated. This is not such a problem in terrestrial applications, where the different models can be compared against each other and lab experiments (e.g. Gorman *et al.* 2016) in order to ensure the most accurate model is used. As astrophysical objects cannot be reproduced and observed in a controlled manner any similar investigation taken without great care is likely to result in overfitting the turbulence model to the few objects that can be observed.

4.7 Conclusions

This chapter presents the effects the k-ϵ sub-grid turbulence model has on a galactic disk, using high resolution, three dimensional simulations.

A massive disk galaxy that would otherwise be stable, expands significantly in the z-direction under the influence of the k-ϵ model. This is shown not due

to be due to turbulent heating (i.e. something that may be mitigated by cooling processes) and occurs independently of the initial turbulent energy but rather inherent properties of the turbulence generated by shear forces in the galaxies differential rotation. It is also too large to be contained by reasonable alterations to the pressure distribution, suggesting it is a flaw in the turbulence model.

The only previous instance of the use of a turbulence model with a disk galaxy (Scannapieco & Brüggen (2010)) is done with a much smaller (dwarf) galaxy. No erroneous behaviour is seen in their simulations, due to the lower Mach number of the rotation or the shorter timescales.

Turbulence models were generally developed to solve terrestrial problems so it is perhaps unsurprising that they fail in circumstances unique to astrophysics. If they are to be applied to such problems, a more systematic approach is needed, comparing multiple different turbulence models, such that there relative strengths and weaknesses may be compared and their failure points documented. However without a "one size fits all" turbulence model it is hard to have faith in their predictive power. Given its ubiquity the k-ϵ model is perhaps the closest thing to this, however as shown here, it is not without its problems.

Chapter 5

Ablation of stellar disks

5.1 Introduction

It is widely believed that massive stars can trigger the formation of lower mass stars in their surrounding regions, leading to frequent associations of massive stars, and young low mass stars. For instance, there are $\sim$ 2000 low-mass stars within 2pc of the centre of the Trapezium cluster (Hillenbrand & Hartmann 1998), and stars with circumstellar disks (O'dell *et al.* 1993; McCaughrean & O'dell 1996; Bally *et al.* 1998) within a few tenths of a parsec of the central star, θ^1 Ori C. As massive stars are often the source of strong winds and eventual supernova, these regions are potentially hostile to protoplanetary disks and the subsequent formation of planets, not only due to direct ablation but also the ionizing radiation created by massive stars.

When radiation dominates, the stellar disk is photoevaporated, giving rise to a photoevaporative flow which collides with the on coming wind (Henney & Arthur 1997). Objects under-going this interaction are typically referred to as

proplyds.

If the flow from the massive stars is stronger than any photoevaporative flow, it interacts directly with the circumstellar disk, allowing hydrodynamic ablation and mixing to occur. The mixing of supernova material into the disk has been suggested as a mechanism to introduce short-lived radionuclides into the early solar system (Goswami *et al.* 2005; Looney *et al.* 2006; Ouellette *et al.* 2005; Tachibana *et al.* 2006) and has been examined in a limited manner by Ouellette *et al.* (2005). However their simulations are two dimensional, and hence limited to a face-on orientation. Figure 5.1 shows their disk before and after the effect of the SNR. They find that only a small fraction ($\sim$ 1%) of the disk mass is removed, in contrast to the $\sim$ 13% expected from the analytical prediction of Chevalier (2000). They attribute this to the cushioning and deflecting effect of the bow shock in addition to the compression of the disk further into the gravitational well of the central star. However their simulations are limited to two dimensions and face-on impacts. While an inclined disk might be expected to be disadvantageous for ablation, the geometry of the bowshock that shields the disk is likely to be substantially different and the wind acts with the rotation of the disk on one side making the threshold for ablation lower.

This chapter aims to improve and expand on the 2D hydrodynamical calculations of Ouellette *et al.* (2007) in a number of ways. Firstly, by doing fully 3d simulations, which also allows the angle between the disk and the flow to be varied. Secondly, by considering a range of disk masses (1$\times$, 0.1$\times$ and 0.01$\times$ their canonical disk mass). Finally, time-dependent flow properties from a 1D simulation of the SNR are adopted. This provides more accurate flow conditions past the disk, compared to the analytical approximation used by Ouellette *et al.*

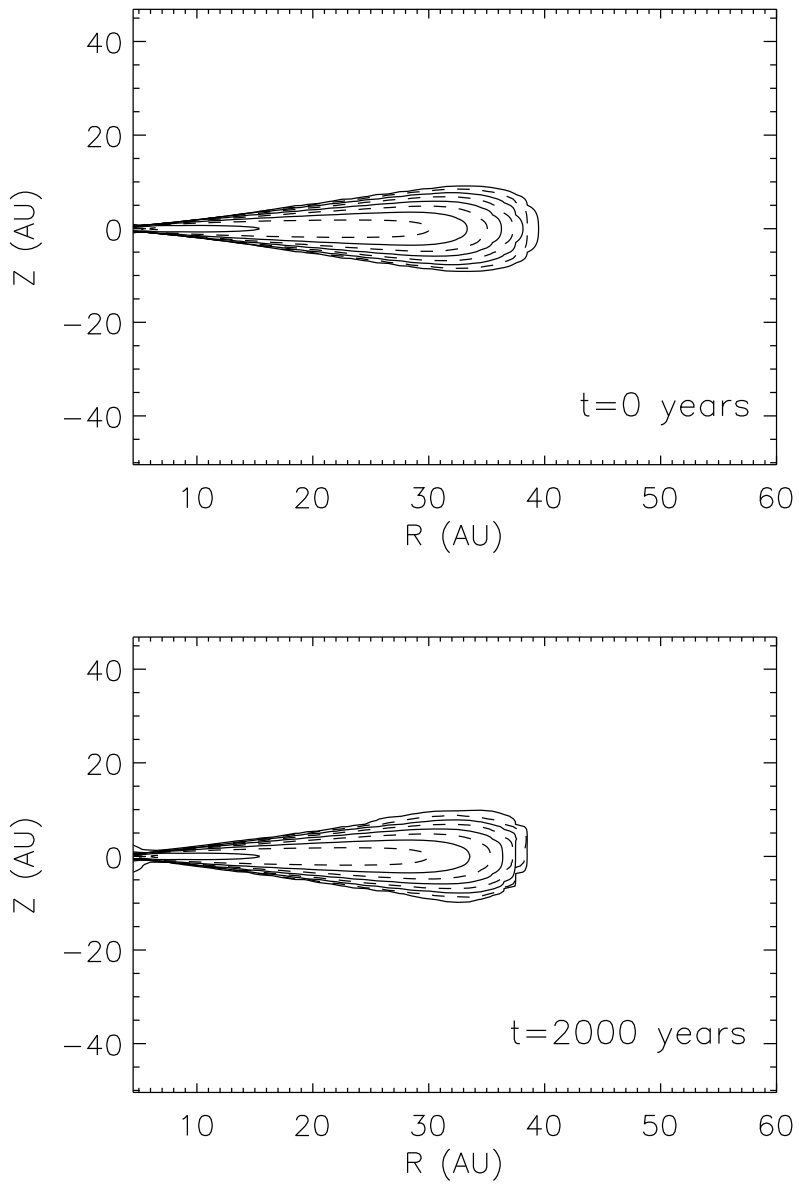

Figure 5.1: Density contours from the disk of Ouellette *et al.* (2005). The top panel shows the disk prior to impact by supernova ejecta. The bottom panel shows the disk 2000 yr after impact.

Table 5.1: SNR parameters

Variable	Value
M_{ej}	$20\ \mathrm{M}_{\odot}$
E_{ej}	$10^{44}\,\mathrm{J}$
ρ_{amb}	$2.34 \times 10^{-24}\,\mathrm{g\,cm^{-3}}$
T_{amb}	$10^{4}\,\mathrm{K}$

(2007), particularly in the early stages of the SNR's expansion. This chapter aims to better determine the nature of the interaction, the mass-stripping rate of the disk, and the injection rate of SLRs into the disk.

5.2 Models

5.2.1 Overview

A stellar disk is simulated in three dimensions, with mass injected onto the grid to simulate the impact of a SNR. The strength of the flow is dependent on the size and distance of the supernova and is time dependent. To calculate this precisely, a simple, one dimensional simulation of a SNR is performed. The evolution of the density, velocity and temperature are recorded at the desired distance from the supernova, which can then be used by the main simulation to control the properties of the wind. This is in many ways simpler than performing an analytical approximation (e.g. Matzner & McKee (1999)), and has the advantage of reproducing all the features of a realistic SNR, particularly in the early expansion.

5.2.2 The supernova remnant

The supernova has an ejecta mass of $20\ \mathrm{M}_{\odot}$ and an ejecta energy of $10^{51}\,\mathrm{erg}$ (following Ouellette *et al.* (2007) to represent a typical type II supernova). At

Table 5.2: Disk model parameters

Variable	Value(s)
R_0	$1\,\mathrm{au}$
T_0	$400\,\mathrm{K}$
ρ_0	$\begin{cases} 3.5\times10^{-13}\,\mathrm{g\,cm^{-3}} \\ 3.5\times10^{-12}\,\mathrm{g\,cm^{-3}} \\ 3.5\times10^{-11}\,\mathrm{g\,cm^{-3}} \end{cases}$
M_*	$1\ \mathrm{M}_\odot$

the start of the simulation the energy is initially thermal is confined to a radius of 2000 au. The ambient medium is set to a density of $2.34\times10^{-24}\,\mathrm{g\,cm^{-3}}$ and a temperature of $10^4\,\mathrm{K}$. The simulation parameters are noted in Table 5.1. For all simulations, the mean molecular weight, $\mu = 2.4$, and $\gamma = 5/3$. The supernova calculations were performed in spherical symmetry on a uniform 1 dimensional grid, extending to $r = 10^5\,\mathrm{au}$ with 3200 cells. The same calculations were done at half and quarter resolution with identical results.

Figure 5.2 shows how the fluid variables change over time at a point 0.3 pc from the origin of the SNR. 0.3 pc is chosen to aid comparison with Ouellette *et al.* (2007) and is consistent with observations of the Orion Trapezium Cluster. These values will determine the properties of the flow past the circumstellar disk in the 3d simulation. The strength of the flow is parametrised by the ram pressure, $P_{ram} = \rho\nu^2$, and is shown in Figure 5.3. Also shown is the ram pressure curve used by Ouellette *et al.* (2007), which is only a close approximation to the numerical results at late times. The interaction is strongest in the early stages, where the approximation is poor.

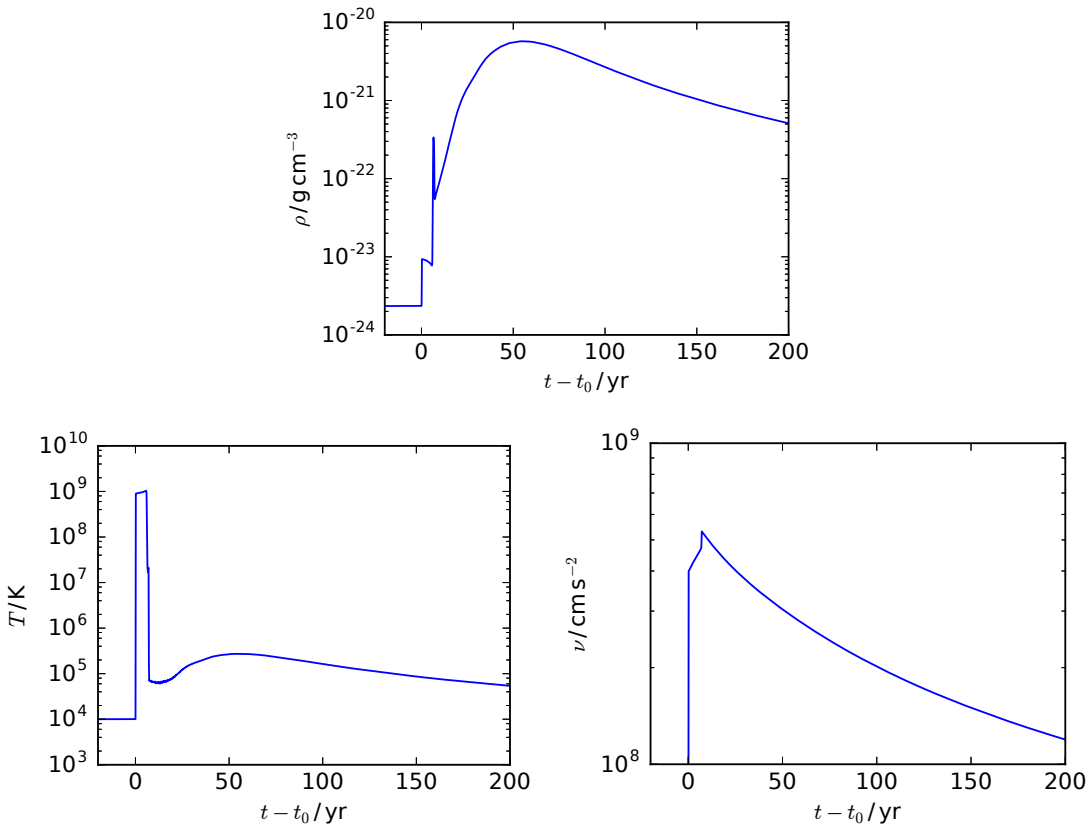

Figure 5.2: Density, temperature and velocity of the fluid 0.3 pc away from the supernova as described in Section 5.2.2. t_0 is the time at which the SNR shockwave first reaches a radius of 0.3 pc.

5.2.3 The circumstellar disk

The disk model is adapted from Gressel *et al.* (2013). The temperature is defined to be constant across z, and to be inversely proportional to cylindrical radius, R,

$$T(R) = T_0(R/R_0)^{-1}. \tag{5.1}$$

This gives the disk a constant opening angle. A constant opening angle is typically desirable as it allows the disk edge to align with cell boundaries in a spherical-

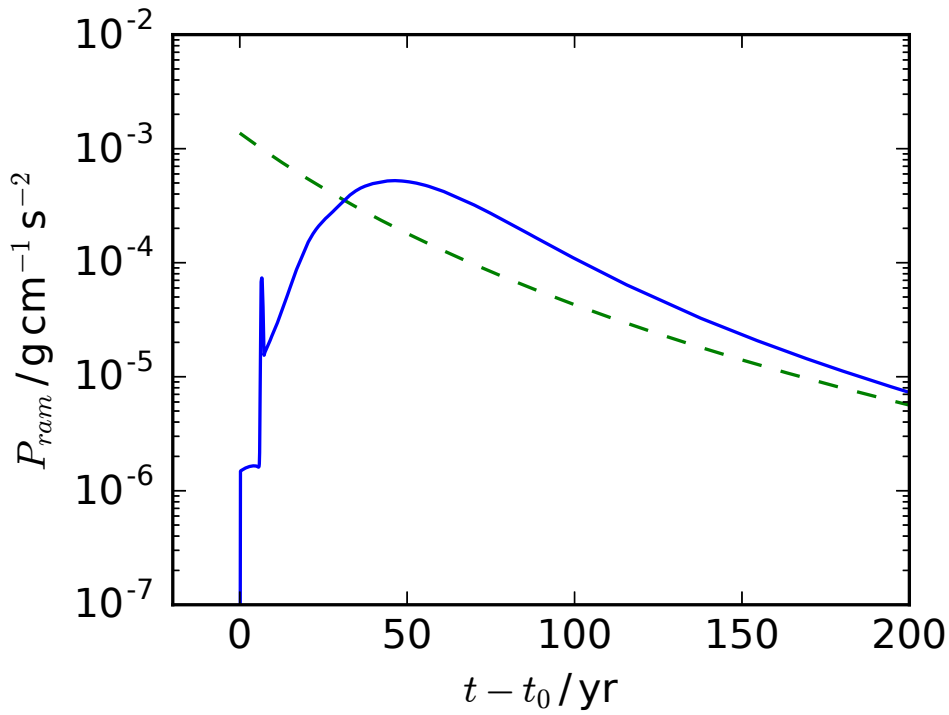

Figure 5.3: Ram pressure 0.3 pc away from the supernova as described in Section 5.2.2. t_0 is the time at which the SNR shockwave first reaches 0.3 pc. The dashed green line shows the ram pressure used by Ouellette *et al.* (2007) for comparison.

polar domain. While this is not a concern for these simulations, it aids comparison with works in the literature. Defining the midplane density as

$$\rho_{mid}(R) = \rho_0 (R/R_0)^{-3/2}, \tag{5.2}$$

and enforcing hydrostatic equilibrium vertically defines the three dimensional density structure, which can be derived as

$$\rho(\boldsymbol{r}) = \rho_{mid} \exp\left(\frac{GM_*}{c_s^2}\left[\frac{1}{r} - \frac{1}{R}\right]\right), \tag{5.3}$$

where c_s is the isothermal sound speed, and r is the distance to the centre of the disk. Finally, the angular velocity, Ω, is set to achieve radial equilibrium,

$$\Omega(\boldsymbol{r}) = \Omega_k(R)\sqrt{\frac{R}{r} - \frac{5}{2}\left(\frac{c_s}{\Omega_k(R)R}\right)^2}, \tag{5.4}$$

where $\Omega_k(R) = \sqrt{GM_*}R^{-3/2}$ is the Keplerian angular velocity. The free disk parameters are chosen such that the disk resembles that described in Ouellette *et al.* (2005). As they observe no significant ablation of their disk, lower disk mass simulations are also performed, which are likely to be more susceptible to ablation. The values are summarised in Table 5.2. The disk is truncated at an inner radius of 4 au and an outer radius of 40 au. The temperature of the disk ranges from 100 K to 10 K from the inner to outer disk boundaries. The outer rotation period is ~ 250 yr and the inner rotation period is ~ 10 yr. The initial ambient medium (ρ_{amb} and T_{amb}) is set to the same as that of the supernova simulation for consistency (see Table 5.1). The disk was evolved in isolation and found to be stable for several outer rotation periods.

It should be noted that much bigger disks (with radii up to ~ 1000 au see e.g. Bally *et al.* (2015)) have been observed. Such disks have a much larger surface area and the outer regions are less strongly held by the gravitational field, meaning they will lose mass to ablation more readily. However, a 40 au disk is used here to aid comparison with previous work. Without good statistics of the disk radius at formation it is also hard to say what is more typical and in any case it likely depends on unknown quantities such as the conditions under which the cluster formed. Having said this, since material at larger radius is easier to strip, disks with the same central density and stellar mass should strip

Table 5.3: Simulation regions and flow directions for each inclination angle.

Inclination	Injection Region	Grid size / au { X, Y, Z }	Flow direction
		$(-256, +128)$	
$0°$	$X > 96$	$(-256, +256)$	$-X$
		$(-256, +256)$	
		$(-256, +128)$	
$45°$	$X > 96$ or $Y < -96$	$(-128, +256)$	$-X, +Y$
		$(-256, +256)$	
		$(-256, +256)$	
$90°$	$Y < -96$	$(-128, +256)$	$+Y$
		$(-256, +256)$	

Table 5.4: Summary of the simulations. The disk angle (i) is defined as the difference in angle between the angular momentum vector of the disk and the vector of the flow direction, making $0°$ face-on and $90°$ edge-on. M_J is the mass of Jupiter.

Simulation	ρ_0 / g cm^{-3}	M_{disk} / M_J	i	Dynamic flow?
const00high	3.5×10^{-11}	8.22	$0°$	n
const00med	3.5×10^{-12}	0.822	$0°$	n
const00low	3.5×10^{-13}	0.0822	$0°$	n
const45low	3.5×10^{-13}	0.0822	$45°$	n
const90low	3.5×10^{-13}	0.0822	$90°$	n
dyn00low	3.5×10^{-13}	0.0822	$0°$	y
dyn45low	3.5×10^{-13}	0.0822	$45°$	y
dyn90low	3.5×10^{-13}	0.0822	$90°$	y

down to the same mass and radius regardless of their initial radius. With this in mind, some insight into the behaviour of larger disks can also be gleaned from our simulations.

5.3 The simulations

All simulations are performed on a three dimensional Cartesian grid, with the disk situated at the origin, and the plane of rotation aligned with the X-Y plane. For each simulation a "flow injection region" is defined where the values of the grid cells are set to the current SNR flow properties at the beginning of each time

step. This region is placed 96 au from the origin. The simulation region extends to ± 256 au in all directions, except in the cases where this would create a large flow injection region. The parameters of the different flow injection regions and grid sizes are listed in Table 5.3. For all simulations the lowest grid level has a resolution of 8 au, with 4 additional grid levels giving an effective resolution of 0.5 au.

There are two reasons the disk is kept in the same orientation and the wind direction is changed (as opposed to vice versa). Firstly, if the plane of rotation is not aligned to the direction of the grid, instabilities can develop and cause the disk to fragment with no outside influence (e.g., Davis (1984); Hahn *et al.* (2010); Hopkins (2015)). Secondly, the grid is split among processors by dividing the domain along one of the grid directions. Placing the disk such that the divides split the disk across processors helps to distribute the computational load more evenly and allows the simulations to run more efficiently.

A set of eight simulations are performed. Table 5.4 details the differences between them. Some simulations are done with a constant flow, as this is the most straight forward to compare against analytical approximations. The parameters of the constant flow are defined by the peak ram pressure point of the SNR (see Figures 5.2 and 5.3) and occurs 55.8 yrs after the disk is first hit by the SNR. The peak is taken as it represents the worst case scenario for the survival of the disk. Specifically this is a density of $5.74 \times 10^{-21}\,\mathrm{g\,cm^{-3}}$, a velocity of $2.87 \times 10^{8}\,\mathrm{cm\,s^{-1}}$ and a temperature of $2.72 \times 10^{5}\,\mathrm{K}$. The corresponding ram pressure is $4.74 \times 10^{-4}\,\mathrm{g\,cm^{-1}\,s^{-2}}$. In contrast the flow in the dynamic simulations follows the temperature, density and velocity of the calculated SNR, shown in Figure 5.2.

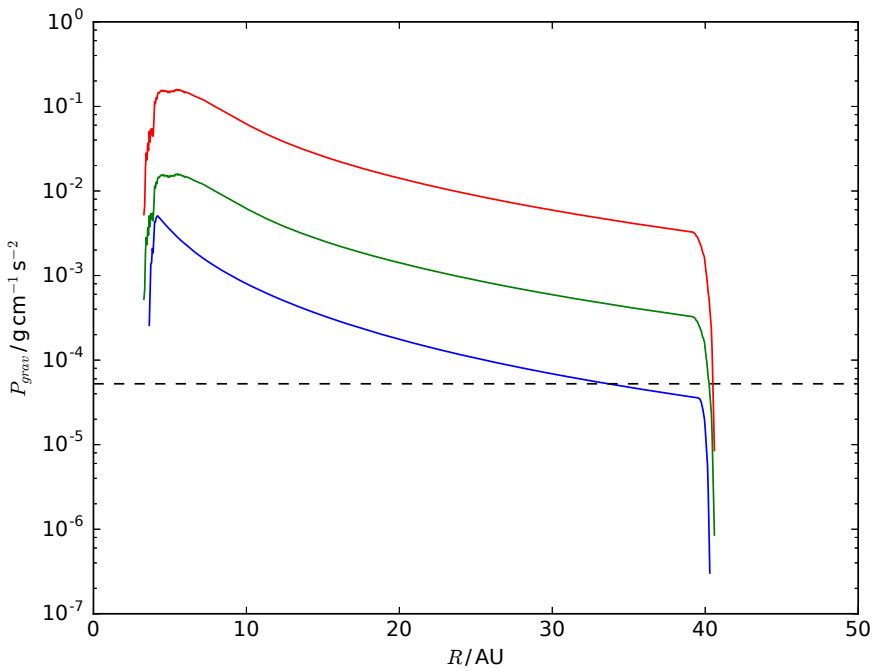

Figure 5.4: Gravitational pressure in the disk as a function of radius, as defined by Equation 5.5. The blue, green and red lines correspond to the low, medium and high values of ρ_0 (see Table 5.4 for details). The dashed horizontal line shows the peak ram pressure of the SNR at 0.3 pc.

5.4 Analytical Approximations

Material in the disk will be disrupted if the ram pressure of the wind exceeds the gravitational force per unit area, P_{grav}. This can be estimated as (Chevalier 2000):

$$P_{grav} = \frac{GM_*\sigma}{R^2}, \tag{5.5}$$

where σ is the surface density of the disk. Figure 5.4 shows the gravitational pressure as a function of radius for the three disk masses considered. By integrating surface density from the centre of the disk to the point at which the gravitational pressure drops below the peak ram pressure of the SNR, an estimate

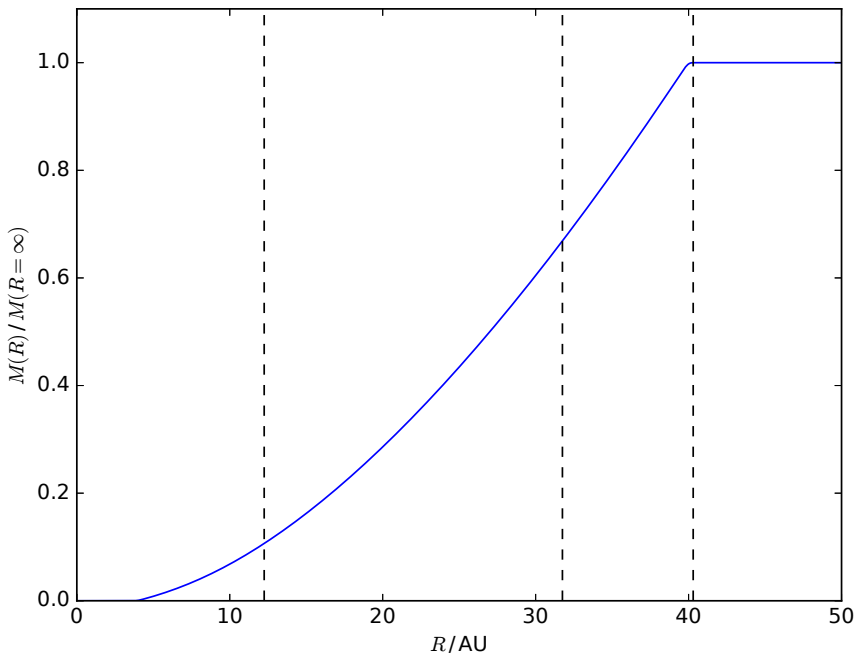

Figure 5.5: The fractional integrated mass of the disk as a function of disk radius. Note this is the same for all values of ρ_0 for the density distribution given by Equation 5.3. The dashed vertical lines shows the radius outside which the gravitational pressure of the disk is less than the peak ram pressure of the SNR for each value of ρ_0. From left to right the dashed lines are shown for low, medium and high disk mass cases.

for the extent of the instantaneous stripping can be obtained.

Figure 5.5 shows the cumulative integrated mass for the disk. If all the material at a gravitational pressure less than the peak ram pressure of the supernova is stripped, then the low mass disk is left with 10.7% of its initial mass, the medium density disk retains 65.1% and the high mass disk retains 99.95%.

In their investigation of the effects of inclination on the ablation of disk galaxies, Roediger & Brüggen (2006) provide an argument for why stripping should be independent of inclination angle for small angles. Assuming the gas disk to be infinitely thin, the force due to ram pressure on a surface element dA is

$\rho_{wind}\nu_{wind}^2\cos(i)$. The ram pressure is effectively reduced by a factor of $\cos(i)$. As the radial gravitational force is balanced with the centrifugal force only the force perpendicular to the plane of the disk contributes. This is also reduced by a factor of $\cos(i)$. This means that the criteria for material to be stripped from the disk is independent of inclination angle. For highly inclined disks, the assumption of an infinitely thin disk will break down. While galactic disks are in a very different area of parameter space to stellar disks, these arguments are equally valid for either case.

5.5 Results

Figures 5.6-5.8 show snapshots of the evolution of the disk with two dimensional slices though the three dimensional grid. Figure 5.6 shows the evolution of disks of different masses subject to a constant flow. As expected the more massive disks are more resilient to stripping. The low and medium mass disks are significantly deformed by the flow. For the low mass disk this breaks up the disk and forms a turbulent tail. However, in the medium mass case the deformed disk remains bound.

Figures 5.7 and 5.8 show the effect of inclination angle for the constant flow and dynamic flow cases respectively. For inclined disks the stripping is asymmetrical. For disk inclinations of 45° the leading edge fragments and strips from the disk first, as the bow shock partially shields the trailing edge of the disk. As the disk continues to evolve the trailing edge is stripped and the disk becomes more symmetrical again. As the 45° disk evolves, the disk is heavily stripped and eventually destroyed. At an inclination of 90° the side of the disk rotating in

the direction of the flow is stripped more heavily at first than the side rotating against the flow. Mass is stripped from the 90° disk much more slowly than for disks with lower inclinations, due mainly to the lower cross-sectional area of the disk to the flow.

The morphology of the constant wind and dynamic wind cases is broadly similar in all cases. The main distinguishing feature is that as the pressure of the dynamic wind starts to decrease, the tail becomes much wider.

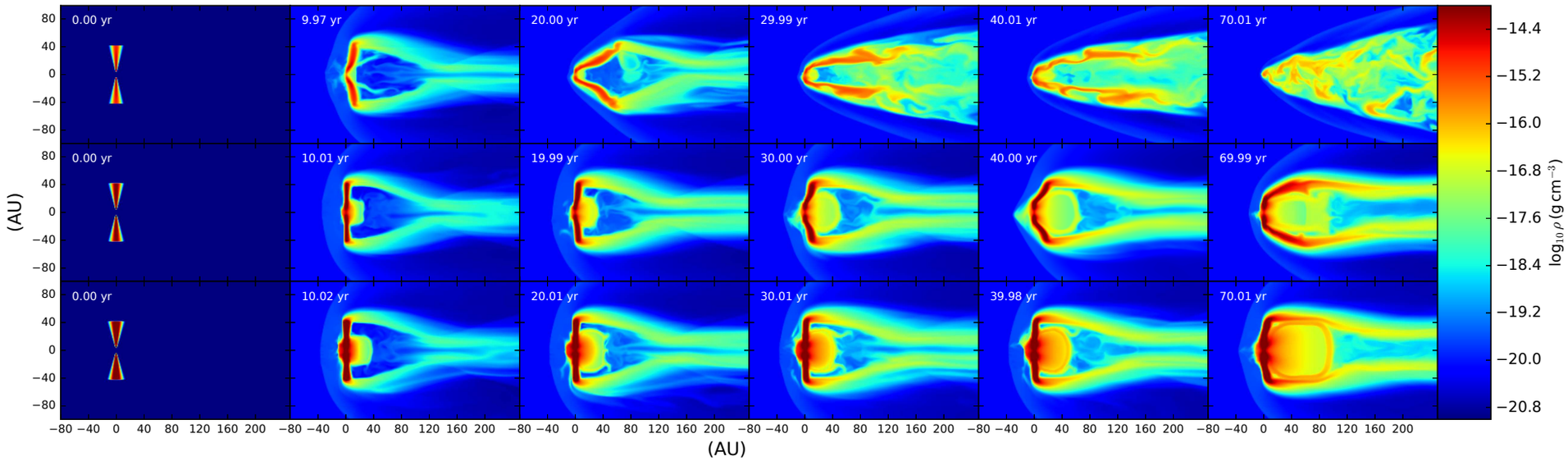

Figure 5.6: Slices through the X-Z plane at Y= 0 for the simulations of varying disk mass. The simulations from top to bottom are **const00low**, **const00med** and **const00high**. The flow is constant and from left to right.

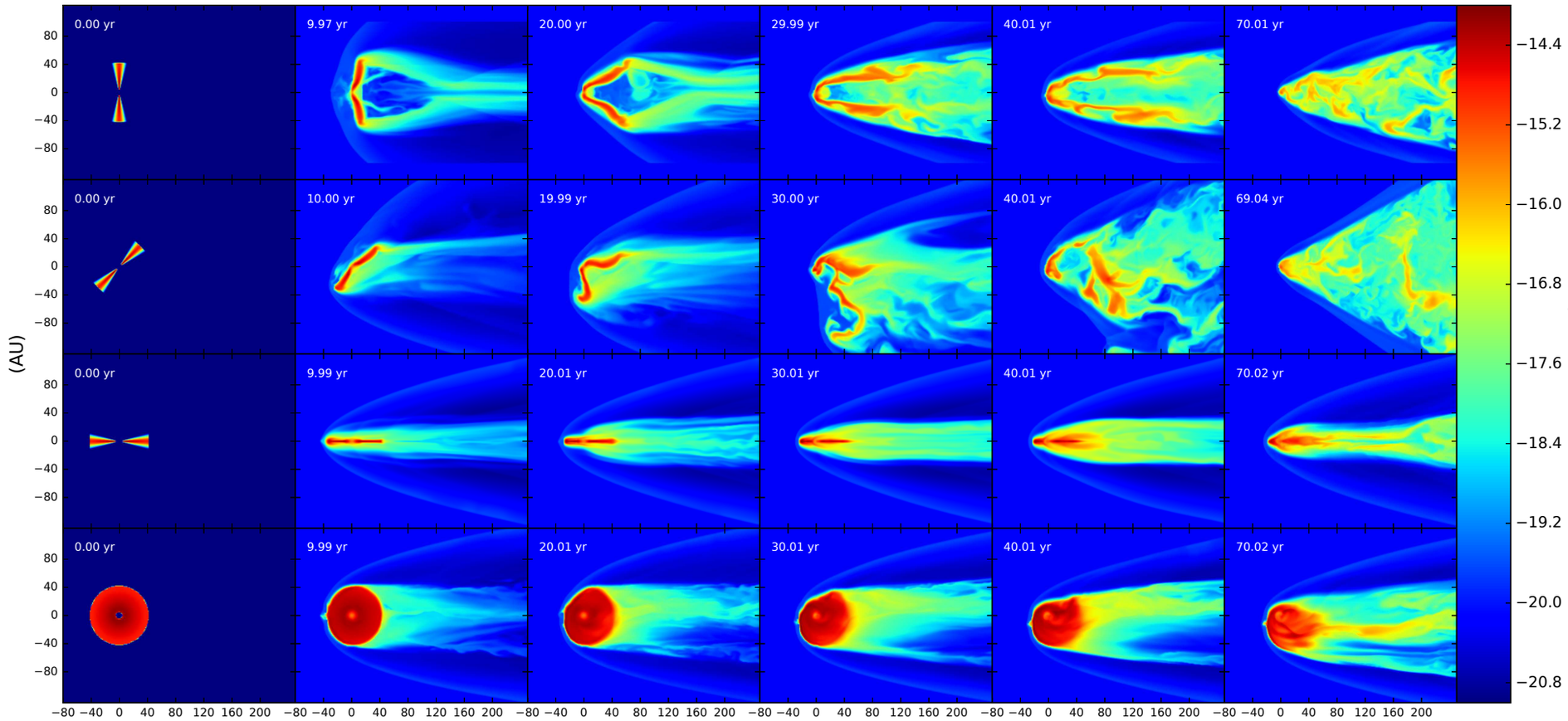

Figure 5.7: Slices through the X-Z plane at Y= 0 for the constant flow simulations. From top to bottom: **const00low**, **const45low** and **const90low**. The bottom row also shows a slice though the X-Y plane at Z= 0 for **const90low** (the disk rotates clockwise in these images). Note that although the simulations are performed by changing the angle of the flow, the images here are rotated such that the flow in each image is from left to right in the plane of the slice.

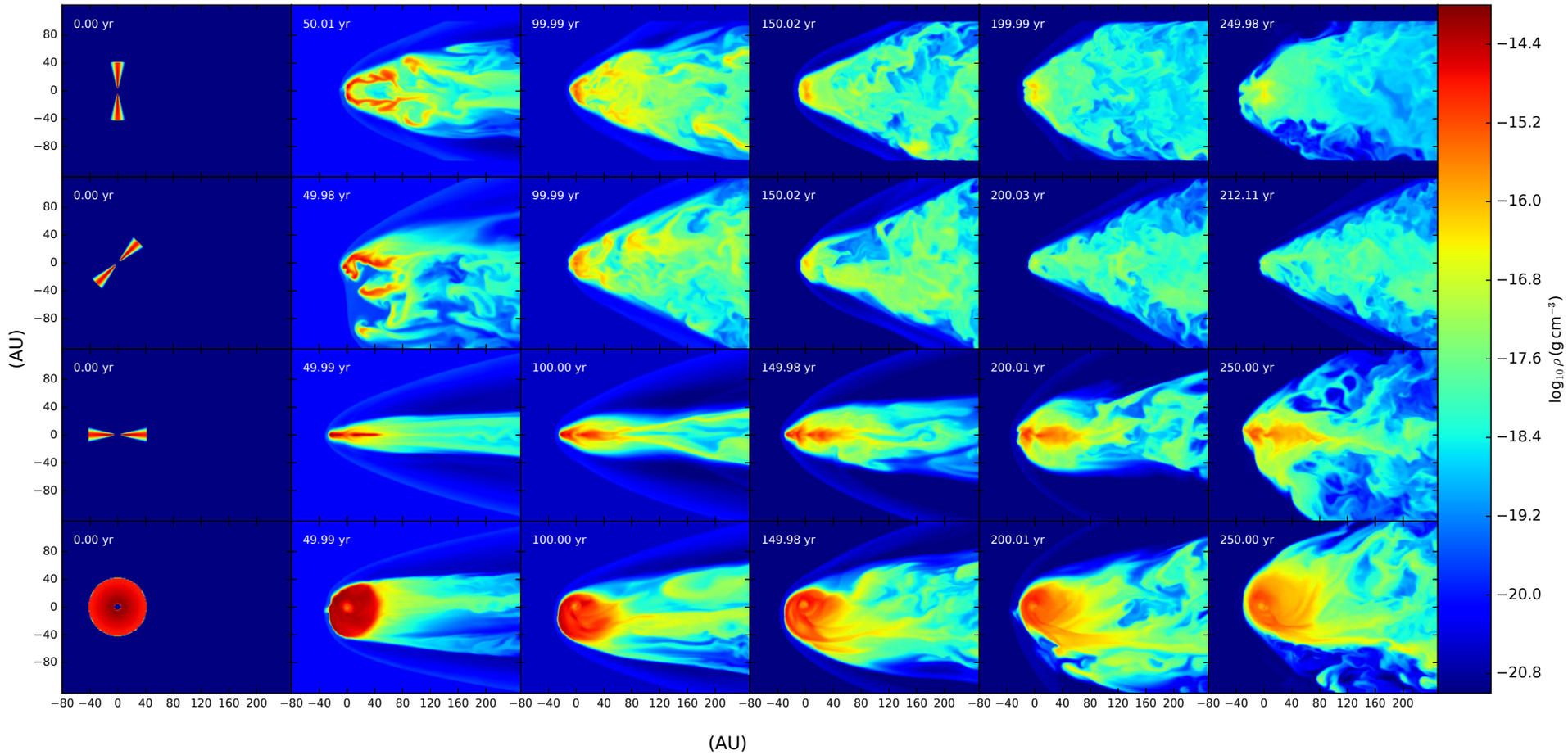

Figure 5.8: As Figure 5.7 but for the dynamical flow simulations, **dyn00low**, **dyn45low** and **dyn90low**.

The amount of mass bound to the star's gravitational well is shown as a function of time in Figures 5.9-5.11. Simulations with a constant flow exhibit an initial rapid ("instantaneous") stripping down to the level where the ram pressure is balanced by the gravitational pressure (where the disk mass plateaus), followed by a slower continual stripping caused primarily by the Kelvin-Helmholtz instability. Figure 5.9 shows this for the three different disk masses simulated, together with the analytical approximations. For the low mass disk, the analytical prediction fits the position of the plateau very well. The medium mass disk begins to plateau but the continual stripping starts to dominate before it does so, pulling the mass below the analytical approximation. The high mass disk loses virtually no mass due to instantaneous stripping and effectively starts in the continuous stripping phase. At the end of the simulation both the medium and high mass disks are losing mass at a rate of $\sim 10^{-6}$ $\mathrm{M}_{\odot}\,\mathrm{yr}^{-1}$. During continuous stripping (between $t = 40\,\mathrm{yr}$ and $t = 70\,\mathrm{yr}$), the mass-loss rate of the low mass disk is $\sim 10^{-7}$ $\mathrm{M}_{\odot}\,\mathrm{yr}^{-1}$.

As the inclination angle of the disk is increased, the stripping is generally slower (Figures 5.10 and 5.11). However, the difference between inclination angles of 0° and 45° is relatively small. Not only do they both plateau at about the same level, but they do so at about the same time (see Figures 5.10 and 5.11). This is because the flow in this instance is strong enough to deform the disk such that the initial inclination angle is no longer relevant. At high inclination angles a different behaviour is observed, and the disk survives significantly longer at an inclination of 90°. The same general trend can be seen in Figure 5.11 for the dynamic flow. Interestingly, for the face-on flow, the mass plateaus before the peak ram pressure has been reached, indicating that the history of the flow is important in shaping

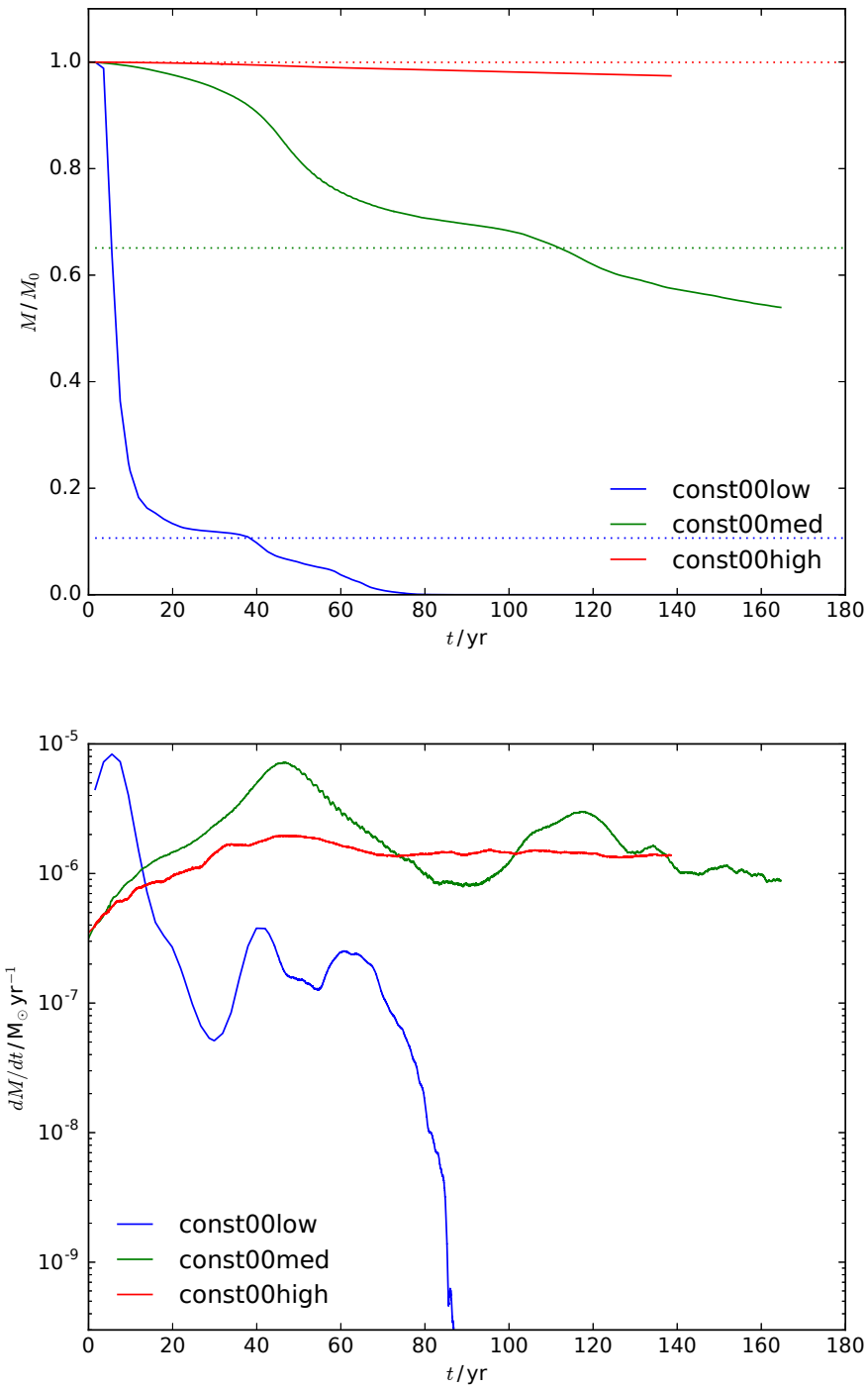

Figure 5.9: The upper panel shows the mass of the disk as a function of time for constant face-on flows, showing the three different disk masses simulated. The dashed lines show the corresponding analytical predictions from Section 5.4. The lower panel shows the mass-loss rates for the same three simulations.

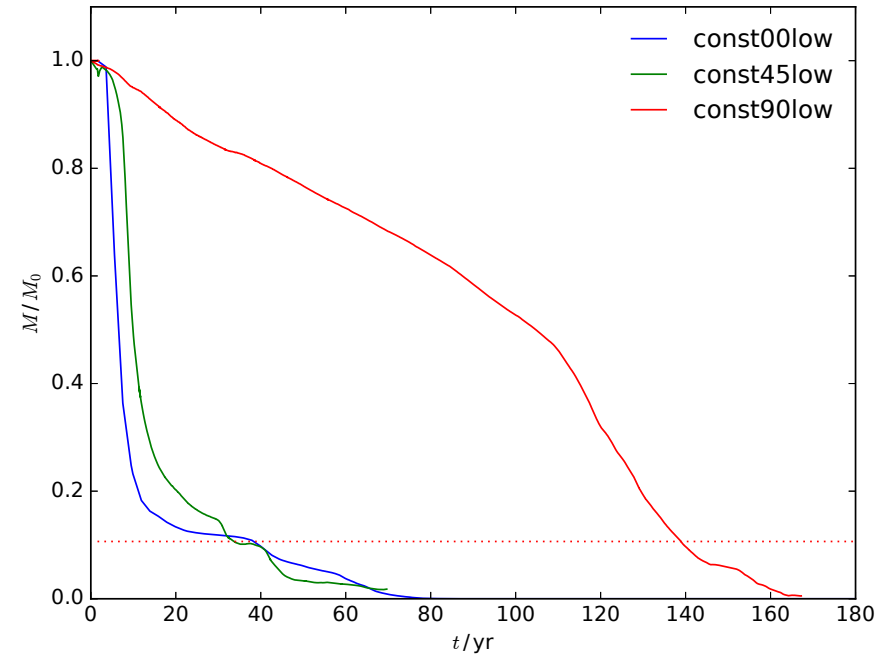

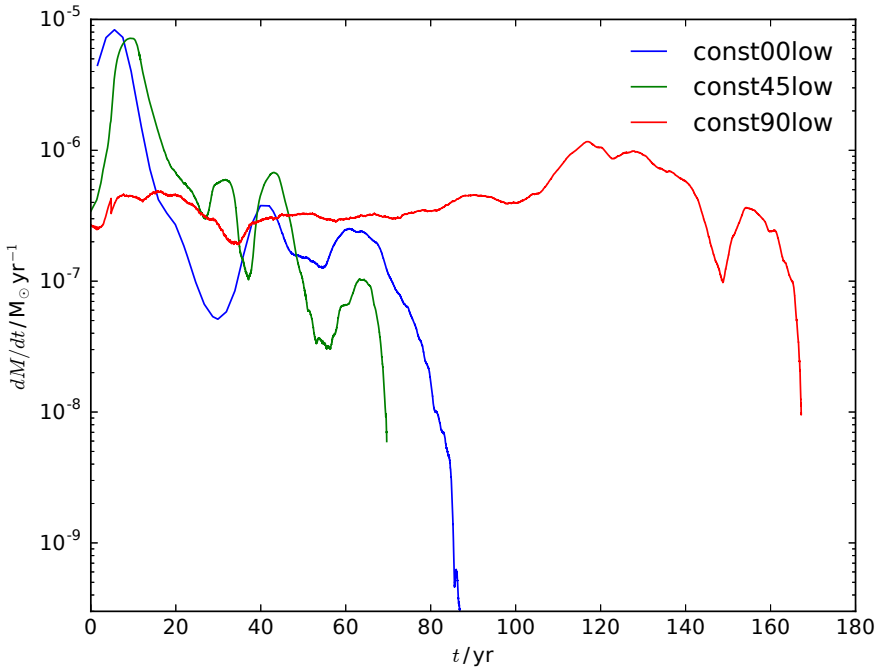

Figure 5.10: As Figure 5.9 but for the different inclinations of the low mass disk in a constant flow. The black dashed line shows the analytical predictions from Section 5.4.

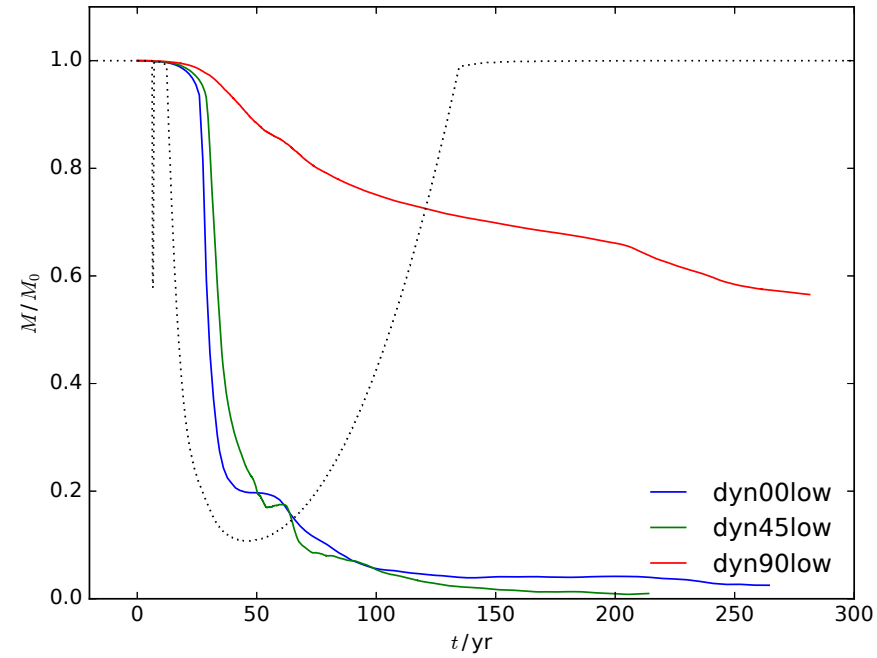

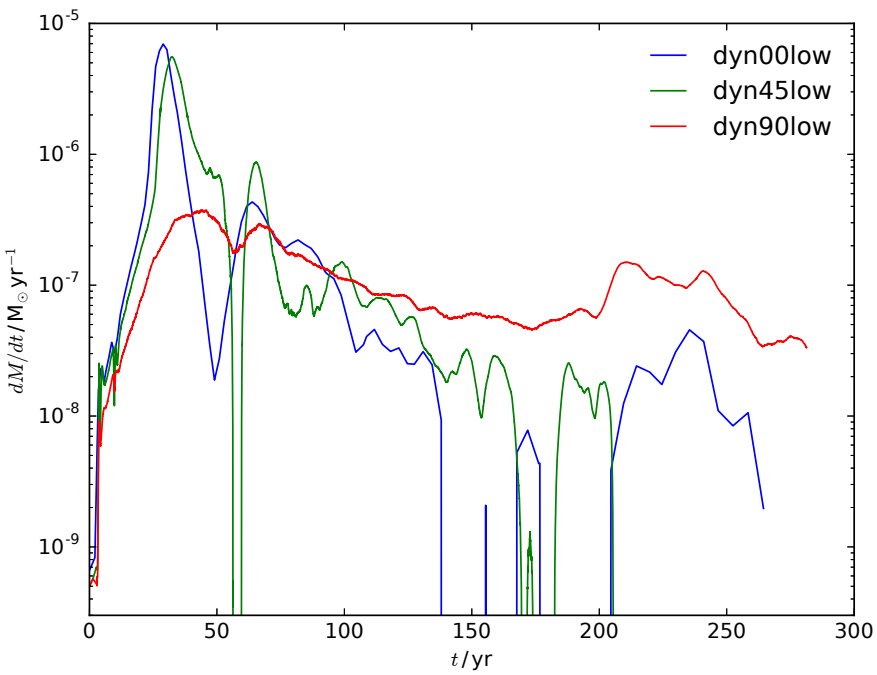

Figure 5.11: As Figure 5.10 but for dynamic supernova flow. The dashed black line represents the fraction of the initial disk mass that is vulnerable to stripping as the ram pressure evolves.

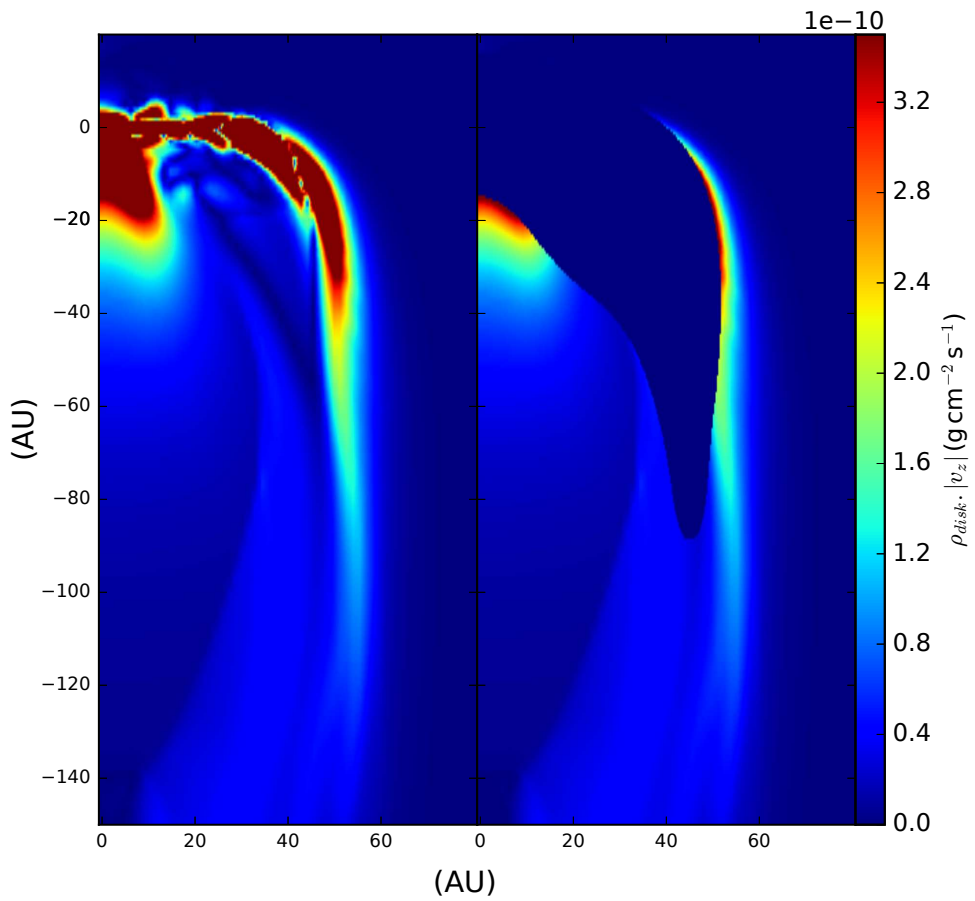

Figure 5.12: Absolute value of the mass flux in the X-Z plane for **const00high** at $t = 140\,\mathrm{yr}$. The left plane shows the total contribution to the mass flux from the disk material. The right plane shows only disk material which is gravitationally unbound from the central star.

the disk and determining whether it is susceptible to ablation. The low mass disk only survives the dynamic flow when placed edge-on to the flow, retaining nearly 60% of its mass in this case (Figure 5.11).

Figure 5.12 shows the z-direction mass flux of the disk material at the end of simulation **const00high**. To show the regions where the disk is losing mass the unbound material is shown in the right panel. Mass is lost from two main regions: along the sides of the deformed disk and also though the central hole. While the

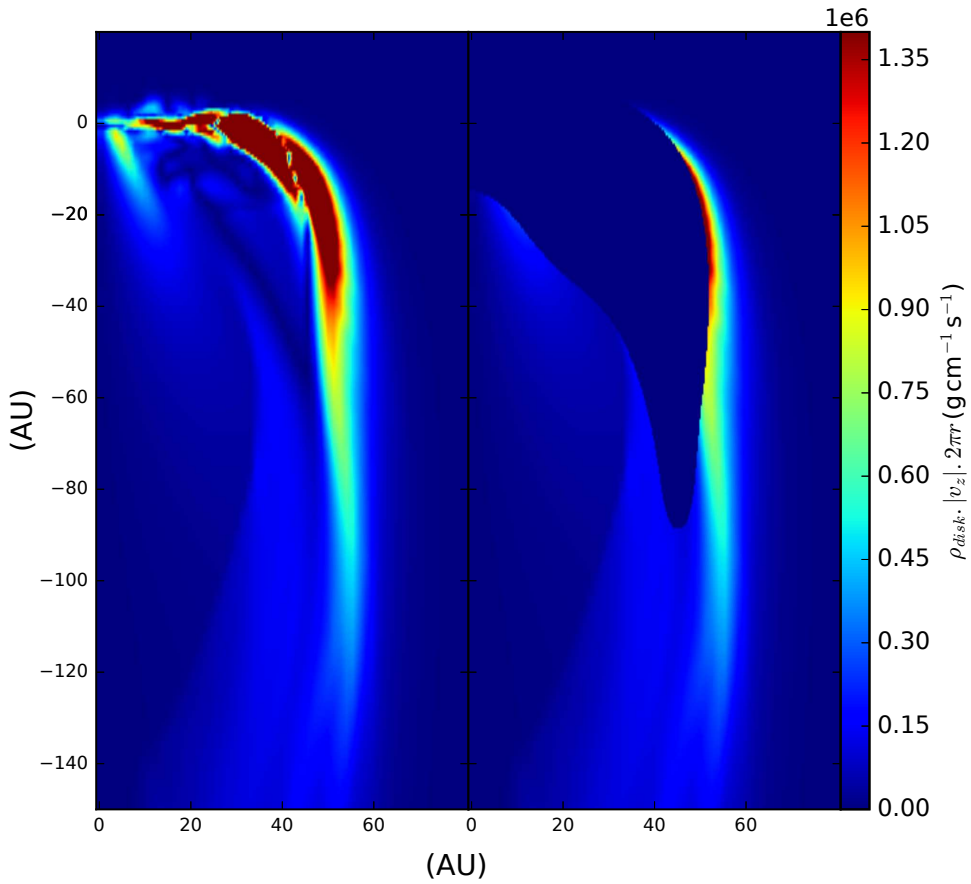

Figure 5.13: As Figure 5.12, but showing the mass flux multiplied by a factor of $2\pi r$.

mass flux in both these areas is similar the central region spans a much smaller area. Figure 5.13 shows the same mass flux as Figure 5.12 now multiplied by a factor of $2\pi r$ to account for the differing contributions to the total mass flux. It is clear that the majority of the mass is lost from the edge of the disk. Ablation from the centre of the disk accounts for approximately 30% of the mass being ablated at this point in the disk's evolution.

Figure 5.14 shows the amount of material from the SNR that becomes bound to the disk, tracked using an advected scalar. The disks in simulations **const00med**, **const00high** and **dyn90low** are the only disks to survive to the end of simula-

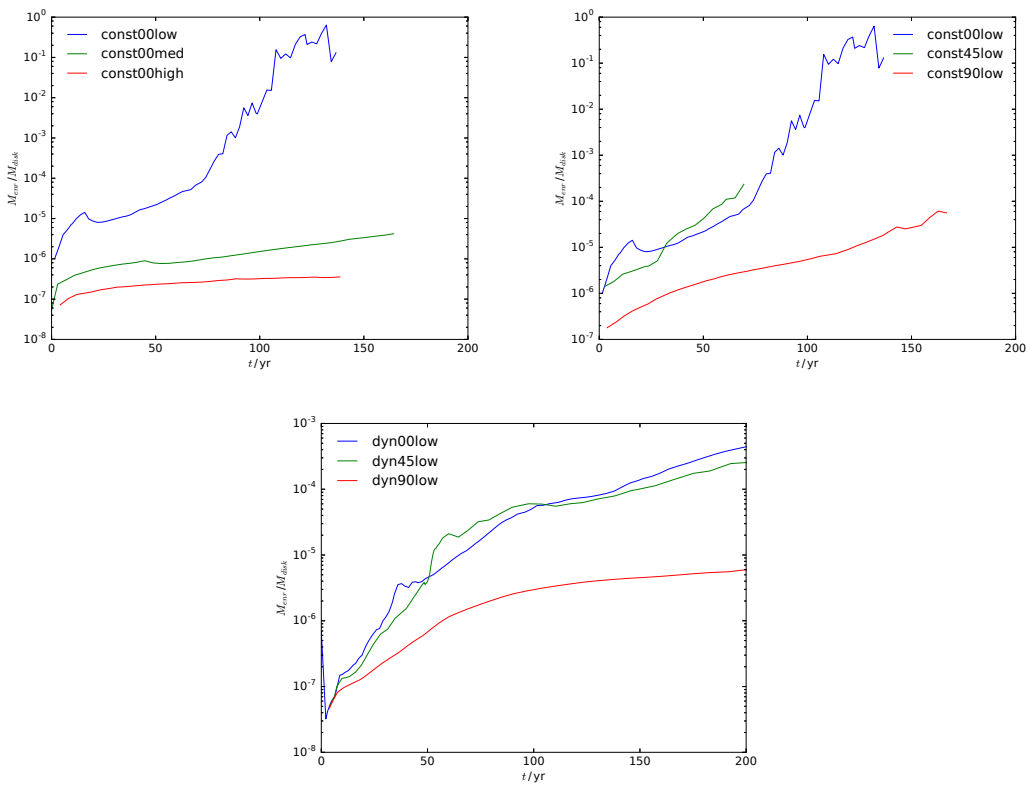

Figure 5.14: Fraction of mass bound to the gravitational field that originated from the SNR as a function of time.

tion and the only ones that could be considered to be enriched by SNR material, although all simulations are shown for completeness. The mass of SNR material in the disk is $\sim 10^{-9}$ $M_\odot$ for face-on disks and $\sim 10^{-10}$ $M_\odot$ for the edge-on disk. The mass is deposited on the surface of the disk as the shock stalls, and little mixing into the disk interior occurs (though in reality, turbulent motions within the disk, which are not resolved in our simulations, may do so). For the edge-on disk the SNR material enters an orbit around the edge of the disk.

5.6 Discussion

5.6.1 Comparison to previous works

The main point of comparison is with Ouellette *et al.* (2005). Our face-on high density disk can be considered equivalent to their canonical disk. Good agreement is obtained in that virtually no stripping is seen in either case. However they see less than 0.1% mass lost over 2000 yr whereas we see $\sim 2.5\%$ lost over 140 yr. This difference can be attributed to the fact that our high density disk is only simulated for the constant ram pressure flow where the long term ablation is much stronger, whereas Ouellette *et al.* (2005) used a time varying flow. Our simulations also differ in that we observe consistency with the analytical predictions of Chevalier (2000), whereas they state that the bow shock shields the disk causing it to be able to survive higher levels of ram pressure.

Li *et al.* (2014) study the effect of triggered star formation, allowing a disk to form and evolve under the effects of a wind. Their simulations are in a very different region of parameter space to ours: the ram pressure of their wind is ~ 7 orders of magnitude lower, so they are observing the interaction on a timescale of Myrs and their disk after formation has a radius of $\sim$ 1000au, with a resolution of 23au. However, they do note that at the end of their simulation the disk radius is much less than that predicted using the method of Chevalier (2000).

As there have been no studies specifically of the ablation of inclined stellar disks, the only comparison that can be made is with galactic disks. Roediger & Brüggen (2006) and Jáchym *et al.* (2009) both specifically investigated the effect of inclination on the ram pressure stripping of galactic disks. We observe the same general dependence on inclination angle, where stripping is similar for low

inclination angles and is only strongly impeded for close to edge-on orientations. We also observe the same asymmetry when disks are not face on. Jáchym *et al.* (2009) argues that the parallel side is stripped more easily as the wind works in the direction of rotation to push the material off the disk, whereas the material on the anti-parallel side must first be slowed to zero velocity and re-accelerated in the opposite direction if it is to be stripped on that side on the disk (otherwise it will continue to orbit round to the other side of the galaxy where it may then be stripped more easily). Roediger & Brüggen (2006) note that after an outer rotation period the disc becomes symmetrical again, as the entire disk has experienced the side with stronger stripping.

For galactic disks the stripping occurs over a relatively long period of time, with the disk experiencing several rotation periods while being ablated. However, the nature of the stripping depends on how the galaxy is orbiting within the cluster. A galaxy on a circular orbit will experience constant ram pressure throughout its lifetime, whereas a galaxy falling radially will experience a shorter peak of ram pressure. Roediger & Brüggen (2007) calculate the dynamic ram pressure for several different orbital paths a galaxy might take. Defining a significant ram pressure as one that would be expected to strip at least half of the disk mass if maintained constantly (this corresponds to what Roediger & Brüggen (2007) refer to as a "medium" ram pressure and is $\sim 10^{-11}\,\mathrm{g\,cm^{-1}\,s^{-2}}$ in their case), the galactic disk experiences significant ram pressure for approximately 0.75 to 2 times the outer rotation period during each orbit.

For the supernova and stellar disk interaction examined here the ram pressure is only significant for $\sim 1/3$ of the outer rotation period. This means it is possible for the stellar disk to maintain asymmetry after the point where stripping is

significant, although it is not clear where the boundary lies, either in terms of ram pressure or rotation periods, in order for this to occur. Also note that this effect requires the flow to impact the disk edge-on or near edge-on for extended periods, whereas a galaxy is likely to experience stripping from a number of different angles at different points in its orbit.

5.6.2 Internal stripping

Our simulations show that a significant amount of mass is lost though the central hole of the disk during the continuous stripping phase. Theoretical considerations show that large planets can cause gaps to form in the disk (Takeuchi *et al.* 1996) and observations of protoplanetary disks have since detected the presence of such gaps (Calvet *et al.* 2002; Andrews *et al.* 2016). If these gaps are large and deep enough they could provide additional channels for ablation to take place.

Similarly, in disk galaxy simulations cooling causes the disk to fragment and allows the wind to flow though areas of low density within the galaxy (Tonnesen & Bryan 2009). This causes the instantaneous stripping to proceed faster but to the same extent compared to the adiabatic, non-fragmented disk. The differences in long term stripping were not investigated but it is likely to be accelerated in the same way by the additional surface area, and will almost certainly effect the morphology of the flow.

5.6.3 Continuous stripping

A number of different authors (Nulsen 1982; Hartquist *et al.* 1986; Arthur & Lizano 1997) have provided estimates for the mass-loss rate of a pressure sup-

ported globule under the effect of a wind. All their estimates are based on the mass-loss rate of the globule being, due to conservation of momentum, approximately equal to the mass flow rate though the cross-sectional area of the object being ablated, i.e., $\dot{M} = \pi r^2 \rho_{wind} \nu_{wind}$. Calculating this value for the constant wind used for the simulations in this chapter gives $\dot{M} = 3 \times 10^{-8}$ $\mathrm{M}_\odot\,\mathrm{yr}^{-1}$ which is around 100 times lower than the value seen in the simulations ($\sim 10^{-6}$ $\mathrm{M}_\odot\,\mathrm{yr}^{-1}$). The flaw in this argument when applied to disks is that each parcel of gas already contains a large amount of momentum due to its rotation. For protoplanetary disks the pressure support is relatively weak so the velocity of the gas is close to Keplerian and thus the escape velocity. This means that the oncoming wind only need to transfer a relatively small portion of its amount to the gas in the disk so that it becomes unbound. In practice this interaction is fairly complex, particularly for non-face-on orientations and there has been no simple analytical formulae proposed, but it is clear that it is not well described by those for simpler, non-rotating objects.

Photoevaporation by a nearby massive star can also play a role in disk dispersal, and is thought to be the cause of the proplyd objects in the Orion nebula (Henney & Arthur 1997). Störzer & Hollenbach (1999) model the effect of an external source of ultraviolet radiation on circumstellar disks, finding good agreement with their models and observations of the Orion proplyds. They provide a crude fit to their results for the mass-loss rate:

$$\dot{M} \approx 10^{-7}\,\mathrm{M}_\odot \mathrm{yr}^{-1} \left(\frac{r_{disk}}{100\mathrm{au}} \right)^{1-1.5}, \tag{5.6}$$

at a distance of 0.2pc from a θ^1 Ori C-like star. Richling & Yorke (2000) perform

a similar analysis and find agreement with the above equation. Calculating this value for a disk of $r_{disk} = 40\,\mathrm{au}$ gives $\dot{M} = 3 \times 10^{-8}\ \mathrm{M_\odot\,yr^{-1}}$. This is ~ 100x less than the continuous stripping rate from the SNR interaction at a distance of 0.3 pc for models **const00med** and **const00high**. Thus supernova induced stripping can far exceed the photoevaporative mass-loss rate and clearly dominates during the interaction of the disk with the SNR.

Another possible source of ablation for stellar disks is the wind from a nearby massive star. This can last much longer than the SNR. For massive stars ($M \gtrsim 25\ \mathrm{M_\odot}$) The strongest wind occurs during the Wolf-Rayet (WR) phase which lasts $\sim 0.3\,\mathrm{Myr}$. For an isotropic wind, the ram pressure at a distance, r is

$$P_{ram} = \frac{\dot{M}}{4\pi r^2 \nu}, \tag{5.7}$$

where $\dot{M}$ is the mass-loss rate of the star and ν is the velocity of the stellar wind. Typical values for the star's wind during the WR phase are $\dot{M} = 10^{-5}\ \mathrm{M_\odot\,yr^{-1}}$ and $2 \times 10^{-8}\,\mathrm{cm\,s^{-1}}$, giving a ram pressure of $1.2 \times 10^{-8}\,\mathrm{g\,cm^{-1}\,s^{-2}}$. This is several orders of magnitude lower than appears in any of the three disk masses simulated (see Figure 5.4) so no direct stripping is possible. While there may be some long term, continuous stripping, it will be much weaker than that seen in any simulation presented in this work.

5.6.4 Planet formation

As planet formation occurs on timescales much longer than the SNR interaction simulated in this work, the disk is likely to re-establish equilibrium before planets begin to form. As far as planet formation is concerned, the interaction is therefore

equivalent to replacing the disk with one of smaller mass.

5.6.5 Enrichment via supernova

Overall very little mass from the SNR flow becomes bound to the disk: $\sim 10^{-9}$ $M_\odot$ for face-on disks that survive the stripping and $\sim 10^{-10}$ $M_\odot$ for the edge-on disk. This is about 10 times less than seen by Ouellette *et al.* (2007). Some of the difference may be due to the differences in the dimensionality of the simulations (3D in our case, 2D in theirs). However, most of it is likely due to differences in the radiative cooling (which is included in their simulations, while ours are adiabatic). Thus the hot supernova ejecta is more able to cool down and mix with the disk in their simulations. The broad conclusion is the same, however: that the enrichment of protoplanetary disks via supernova ejecta by pure hydrodynamic mixing is too inefficient to explain the abundance of SLRs in the early solar system. The highest ejecta contamination seen in our simulations is 5×10^{-6} (which falls short of the 10^{-4} needed using SLR production values from Woosley & Weaver (1995)). Interestingly, this is for our low mass, edge-on case. Low mass disks obviously benefit more from the same amount of ejecta material, but are also generally destroyed more easily. However, we believe that the fact that edge-on disks survive significantly longer than face-on disks allows such disks to intercept more of the SN ejecta, and thus have the highest injection efficiency. So, at least for the particular parameters chosen here, a low mass edge-on disk can be enriched more than a high mass face-on disk. While the disks here do not meet the enrichment requirements deduced from observations, it may be possible that a much larger disk (and hence larger surface area for collection) placed further

away from the supernova (such that its outer parts do not get instantaneously stripped) could be more efficient at absorbing material from a SNR. This is left for the subject of future investigation.

It should be noted that these disks are less massive than the minimum-mass solar nebula solar ($\sim 10 M_J$ versus $8.22 M_J$ for the highest mass disk) and as such should not be interpreted as a simulation of the early solar system. The disk masses were chosen to facilitate comparison with Ouellette *et al.* (2005), and lower mass disks are required to probe the interesting effects of ablation. However, as more massive disks are less effected by ablation we can say with some confidence that the amount of gas in the early solar system would have been unaffected by a supernova occurring 0.3 pc away. This does not exclude the possibility of an extremely close supernova, although the reduced probability of such a close event must be considered. It is disk density, rather than total integrated mass, that determines how a disk responds to an ablating wind, therefore a supernova occurring during an earlier point in the solar system's evolution, while it was less condensed, could have had a larger impact in shaping the solar environment.

5.7 Conclusion

Presented in this chapter are three dimensional simulations of the stripping of stellar disks due to the influence of a nearby SNR, using a physically motivated dynamic flow. We have also investigated the effect of varying the inclination angle and disk mass.

Good agreement is found with the analytical predictions of Chevalier (2000). However, this only accounts for part of the stripping as Kelvin-Helmholtz insta-

bilities can cause additional material to be ablated. In the initial, instantaneous stripping phase, a flow at the peak ram pressure can strip 90% of a low mass disk ($M_d \sim 0.1 M_J$) and 30% of a medium mass disk ($M_d \sim 1.0 M_J$) on timescales of 10-100 yrs (less than one outer rotation period). High mass disks ($M_d \sim 10 M_J$) are largely unaffected by instantaneous stripping.

During continuous, longer-term, ablation disks lose mass at a rate of $\sim 10^{-6}$ $M_\odot\,yr^{-1}$. This value decreases with time as the SNR passes and the flow weakens, but is several orders of magnitude greater than the mass-loss rate due to photoevaporation or stellar wind ablation and will therefore dominate the disk's mass-loss rate during this time.

We find that the inclination angle only has a large effect on the evolution when the disk is close to edge on (similarly to previous findings from simulations of disk galaxies). When the ram pressure is large compared to the gravitational pressure in the disk, low inclination angle disks are deformed to the point that their evolution converges to that of a face-on (zero degree inclination) disk. In contrast, our edge-on disks show a much steadier rate of mass-loss (instantaneous stripping is much reduced due to the lower cross-section) and can survive significantly longer than their face-on counterparts. Amongst the low-mass disks simulated, only the edge-on disk survived interaction with the SNR (retaining almost 60% of its mass).

The stripping of inclined disks can be quite asymmetrical, and the direction of the stripped tail may not line up with the direction of the flow (also like disk galaxies). However, unlike disk galaxies, the flow may die down before the asymmetries have disappeared. For the SNR parameters chosen the interaction is very short, lasting only a couple of hundred years. This means that stellar disks are

unlikely to be observed during this period, but seeing an asymmetric disk may be evidence that it underwent this type of ablation in its past. For disks more distant from the supernova the interaction will likely be longer. There are a number of other processes (e.g. photoevaporation and a wind from a nearby massive star) that produce much weaker stripping than a SNR, but which nonetheless could cause significant stripping on much longer timescales. The exact extent of stripping due to these processes is at this point unknown.

Amongst all the disks, the highest ejecta contamination fraction is 5×10^{-6}, which is much lower than that required to explain the presence of SLRs in the early solar system. The highest contamination is seen in a low mass edge-on disk, suggesting the ideal case for enrichment is a low mass edge-on disk (that would be destroyed if placed face-on) rather than a face-on disk like one might assume.

Chapter 6

Conclusions

This thesis has presented three dimensional numerical simulations of the ablation of galaxies and stellar disks, and how a sub-grid turbulence model may be used to improve the accuracy of results. A summary of the findings of this research is provided in this chapter followed by a discussion on possible future avenues of research and some concluding remarks.

6.1 Summary

Chapter 3 presents simulations of the ram pressure stripping of the hot gaseous halo of a massive galaxy. The long term stripping is mediated by KHIs which are poorly resolved by previous work, particularly those using SPH. This invites the use of a sub-grid turbulence model which allows the effect of turbulent instabilities like the KHI to be accounted for even if they are not resolved on the grid scale.

The interaction occurs in two phases. First the "instantaneous" stripping phase where material is removed in areas where the pressure force exceeds the

gravitational force. The extent of this stripping is well predicted by the analytical formula of Gunn & Gott (1972). This is the general consensus of other works in the literature. This phase is unaffected by the presence of the turbulence model. The second phase of "continuous" stripping is significantly stronger when the turbulence model is used, and is closer to what you would expect from mass flux and momentum conservation arguments. This difference is most pronounced at higher Mach numbers. At Mach numbers of 0.9 and 1.1 there is little to no difference when using the turbulence model, but at a Mach number of 1.9 the galaxy is left with $\sim$ 5 times less material at the end of the simulation, representing a very different future for the star formation in the galaxy.

Chapter 3 extended the use of a sub-grid turbulence model from previous applications to shock-cloud interactions, to a more complex and less idealised system. The logical next step is to examine whether it can be applied to a system that is more complex still, such as the interaction of a wind with a disk. This is the focus of Chapter 4. A disk is of particular interest due to its differential rotation, which gives the fluid a non-zero strain even before it is perturbed by any external shock or wind. This is shown to have an adverse and unphysical effect on the galaxy, causing it to expand along its z-axis until it is almost spherical, exposing a fundamental flaw in the turbulence model.

Chapter 5 presents simulations of the interaction of a stellar disk with a nearby supernova. By performing a simple one dimensional calculation of the evolution of the supernova remnant realistic values can be obtained for the density, velocity and temperature of the resulting flow as a function of time. The time dependent flow can then be injected into the stellar disk simulation. A simulation where the flow has constant density, velocity and temperature is also computed as a

point of comparison. For time independent flow good agreement is found with the analytical predictions of Chevalier (2000) (which follows a similar logic to Gunn & Gott (1972) in the galactic case). However, these are valid only for the instantaneous stripping, whereas in reality there is continuous mass loss in all disks, even those that would not be expected to lose any mass via the predictions of Chevalier (2000). Disks lose mass at a rate of order 10^{-6} $M_{\odot}\,yr^{-1}$ which is faster than other potential mass loss processes, e.g., photoevaporation, accretion, or stellar winds and it is much higher than would be expected from the typical momentum conservation arguments due to the initial rotation of the disk. However, the ablation due to the SNR passage occurs over much shorter timescales. Despite this, for disks with a mass of less than $\sim 1.0\,M_J$ that experience this interaction it is likely to dominant the total integrated mass loss. It should be noted that the ease of ablation is highly dependent on the radius of the disk. The disks simulated in Chapter 5 have a radius of 40 au. A disk with a bigger radius will lose a larger fraction of its mass when hit by the same supernova remnant.

When the disk is inclined to the flow the mass loss is predictably reduced. However it is only at large inclination angles that a significant reduction is seen. Face-on (0°) and 45° disks experience roughly the same mass loss curves. This is consistent with simulations of galactic disks, where similar behaviour is seen. Under the dynamic flow, an edge-on (90°) disk survives the passing of the supernova flow where as more moderately inclined disks (45°) would not. When the disk is oriented edge-on to the flow stripping is asymmetrical due to the rotation of the disk. This is seen to some extent in galactic disk stripping, however the symmetry is restored after the disk has completed a full rotation. As the SNR passages lasts less time than the rotation period of the disk it can result in a

lasting asymmetry to the disk.

The mixing of SNR material into the disk is also investigated, as this has been proposed as a mechanism for injecting SLRs into the early solar system. Amongst all the stellar disks, the highest ejecta contamination fraction is 5×10^{-6}, too low to explain the presence of SLR in the early solar system. This is in general agreement with other works, and shows that contamination must occur either earlier in the disks lifetime (when it was larger or a molecular cloud) or though another method, such as being carried by dust grains. The highest contamination is see in a low mass edge-on disk, suggesting the ideal case for enrichment is a low mass edge-on disk (that would be destroyed if placed face-on) rather than a face-on disk like one might assume.

6.2 Future Work

Like all interesting areas of science, there is still much to be understood on the topic of ablation.

The sophistication of galactic simulations has increased substantially in recent years, with the inclusion of stellar feedback models, dynamic simulation of the cluster instead of static potentials, and realistic orbital trajectories instead of wind tunnel tests (e.g. Steinhauser *et al.* (2016); Martizzi *et al.* (2016)). Despite the improvements in the models, there is still no consensus on the exact role ram pressure stripping plays in galactic evolution. A broad parameter study (galaxy mass, orbital trajectory, cluster size, etc.) is needed in order to produce good relationships between the mass lost from the galaxy and the star formation rate in that galaxy. This, in combination with cosmological simulations, and

galaxy statistics from observations of our current universe, is needed to place ram pressure stripping into the wider picture of galaxy formation and evolution.

In order to perform a good parameter study many simulations are required to be performed. It is therefore beneficial to keep the cost of each simulation down to a minimum. Sub-grid modelling is a great tool for this, and is already being leveraged for things like star formation and feedback. Turbulence modelling can also be beneficial as I have shown in Chapter 3 and is of particular interest when simulating ablation processes as it can lower the resolution needed (Pittard *et al.* 2009).

While turbulence modelling has its advantages it is not without its hazards. It is well established within the engineering literature but a greater body of work needs to be built up within an astrophysical context to understand the limits of the model. As show in Chapter 4 it can behave quite poorly under certain circumstances. A systematic review of different turbulence models is needed so that such models may be used with an understanding of their failure points and confidence can be had in the results.

The state of stellar disk ablation simulations is perhaps less advanced than their galactic counter parts. As shown in Chapter 5 there are a number of similarities (and differences) between simulations of ablation of both disk types and a greater level of cross-citation would likely be of benefit to both groups. There is still much room for improvement of models, the inclusion of radiative transfer for example, which is of particular importance to the dynamics of stellar disks. Also the effects of long term ablation from a sustained wind (such as from a nearby massive star) is still unknown and would be a valuable piece of information to the overall picture of stellar disk evolution.

The origin of SLR is still unknown, but it seems clear that is cannot occur by hydrodynamic mixing during the protoplanetary disk phase. Mediation via dust grains seems plausible, as they penetrate much more easily that gas phase material, although it is uncertain how much material is likely to condense onto grains within a SNR. A SNR simultaneously contaminating a molecular cloud and triggering it to form stars and disks gives higher levels of contamination, although the formation time of the star-disk systems is comparable to the half-lifes of the SLRs. Another possibility is contamination during the early stages of disk formation, while it is still many 100s of au in radius. A parameter study of disk radius and contamination rates would be useful in assessing this as a possibility.

6.3 Final Remarks

Stripping is a process that occurs across a wide scale of objects in astrophysics. This thesis has presented advancements in the models of both galactic ram pressure stripping and stellar disk ablation which will aid future simulations in building a complete picture of the evolution of these objects.

References

Abadi, M.G., Moore, B. & Bower, R.G. (1999). Ram pressure stripping of spiral galaxies in clusters. MNRAS, **308**, 947–954. 8

Abramson, A. & Kenney, J.D.P. (2014). Hubble Space Telescope Imaging of Decoupled Dust Clouds in the Ram Pressure Stripped Virgo Spirals NGC 4402 and NGC 4522. ApJ, **147**, 63. 65

Abramson, A., Kenney, J.D.P., Crowl, H.H., Chung, A., van Gorkom, J.H., Vollmer, B. & Schiminovich, D. (2011). Caught in the Act: Strong, Active Ram Pressure Stripping in Virgo Cluster Spiral NGC 4330. ApJ, **141**, 164. 6, 66

Agertz, O., Moore, B., Stadel, J., Potter, D., Miniati, F., Read, J., Mayer, L., Gawryszczak, A., Kravtsov, A., Nordlund, Å., Pearce, F., Quilis, V., Rudd, D., Springel, V., Stone, J., Tasker, E., Teyssier, R., Wadsley, J. & Walder, R. (2007). Fundamental differences between SPH and grid methods. MNRAS, **380**, 963–978. 8, 41

Alibert, Y., Mordasini, C., Benz, W. & Winisdoerffer, C. (2005). Models of giant planet formation with migration and disc evolution. A&A, **434**, 343–353. 11

Andrews, S.M., Wilner, D.J., Zhu, Z., Birnstiel, T., Carpenter, J.M., Pérez, L.M., Bai, X.N., Öberg, K.I., Hughes, A.M., Isella, A. & Ricci, L. (2016). Ringed Substructure and a Gap at 1 au in the Nearest Protoplanetary Disk. ApJL, **820**, L40. 113

Armitage, P.J., Clarke, C.J. & Palla, F. (2003). Dispersion in the lifetime and accretion rate of T Tauri discs. MNRAS, **342**, 1139–1146. 13

Arthur, S.J. & Lizano, S. (1997). On the Relative Importance of Photoevaporative and Hydrodynamic Effects in the Ablation of Self-gravitating Globules in Compact H II Regions. ApJ, **484**, 810–819. 113

Aspden, A., Nikiforakis, N., Dalziel, S. & Bell, J.B. (2008). Analysis of Implicit LES Methods. *Communications in Applied Mathematics and Computational Science*, **3**, 103–126. 48

Bally, J., Sutherland, R.S., Devine, D. & Johnstone, D. (1998). Externally Illuminated Young Stellar Environments in the Orion Nebula: Hubble Space Telescope Planetary Camera and Ultraviolet Observations. ApJ, **116**, 293–321. 13, 87

Bally, J., Mann, R.K., Eisner, J., Andrews, S.M., Di Francesco, J., Hughes, M., Johnstone, D., Matthews, B., Ricci, L. & Williams, J.P. (2015). ALMA Observations of the Largest Proto-Planetary Disk in the Orion Nebula, 114-426: A CO Silhouette. ApJ, **808**, 69. 94

Balog, Z., Rieke, G.H., Su, K.Y.L., Muzerolle, J. & Young, E.T. (2006). Spitzer MIPS 24 μm Detection of Photoevaporating Protoplanetary Disks. ApJL, **650**, L83–L86. 15

Balogh, M.L., Baldry, I.K., Nichol, R., Miller, C., Bower, R. & Glazebrook, K. (2004). The Bimodal Galaxy Color Distribution: Dependence on Luminosity and Environment. ApJL, **615**, L101–L104. 65

Bekki, K. (2009). Ram-pressure stripping of halo gas in disc galaxies: implications for galactic star formation in different environments. MNRAS, **399**, 2221–2230. 9, 61

Bertoldi, F. & Jenkins, E.B. (1992). Dense clumps of ionized gas near Pi Scorpii, as revealed by the fine-structure excitation of N II. ApJ, **388**, 495–512. 15

Blanton, M.R., Hogg, D.W., Bahcall, N.A., Baldry, I.K., Brinkmann, J., Csabai, I., Eisenstein, D., Fukugita, M., Gunn, J.E., Ivezić, Ž., Lamb, D.Q., Lupton, R.H., Loveday, J., Munn, J.A., Nichol, R.C., Okamura, S., Schlegel, D.J., Shimasaku, K., Strauss, M.A., Vogeley, M.S. & Weinberg, D.H. (2003). The Broadband Optical Properties of Galaxies with Redshifts 0.02 <z <0.22. ApJ, **594**, 186–207. 3

Brown, G.L. & Roshko, A. (1974). On density effects and large structure in turbulent mixing layers. *Journal of Fluid Mechanics*, **64**, 775–816. 51

Burkert, A. (1995). The Structure of Dark Matter Halos in Dwarf Galaxies. ApJL, **447**, L25. 73

Cada, M. & Torrilhon, M. (2009). New Limiter Functions For High-Order Finite-Volume-Methods. In Handlovicova, A and Frolkovic, P and Mikula, K

and Sevcovic, D, ed., *Algoritmy 2009: 18Th Conference On Scientific Computing*, 61–70, 18th Conference on Scientific Computing, Podbanske, SLOVAKIA, MAR 15-20, 2008-2009. 40

Calvet, N., D'Alessio, P., Hartmann, L., Wilner, D., Walsh, A. & Sitko, M. (2002). Evidence for a Developing Gap in a 10 Myr Old Protoplanetary Disk. ApJ, **568**, 1008–1016. 113

Canto, J. & Raga, A.C. (1991). Mixing layers in stellar outflows. ApJ, **372**, 646–658. 60

Carilli, C.L. & Taylor, G.B. (2002). Cluster Magnetic Fields. ARA&A, **40**, 319–348. 42

Chevalier, R.A. (2000). Young Circumstellar Disks near Evolved Massive Stars and Supernovae. ApJL, **538**, L151–L154. 15, 17, 88, 97, 111, 117, 123

Chou, P. (1945). On velocity correlations and the solutions of the equations of turbulent fluctuation. *Quarterly of Applied Mathematics*, **3**, 38–54. 25

Clarke, C.J. & Pringle, J.E. (1993). Accretion disc response to a stellar fly-by. MNRAS, **261**, 190–202. 13

Colella, P. & Woodward, P.R. (1984). The Piecewise Parabolic Method (PPM) for Gas-Dynamical Simulations. *Journal of Computational Physics*, **54**, 174–201. 40

Crowl, H.H., Kenney, J.D.P., van Gorkom, J.H. & Vollmer, B. (2005). Dense Cloud Ablation and Ram Pressure Stripping of the Virgo Spiral NGC 4402. ApJ, **130**, 65–72. 6, 7

Davidson, P.A. (2004). *Turbulence : an introduction for scientists and engineers*. Oxford University Press. 25

Davis, S.F. (1984). A rotationally biased upwind difference scheme for the Euler equations. *Journal of Computational Physics*, **56**, 65–92. 96

de Geus, E.J. (1992). Interactions of stars and interstellar matter in Scorpio Centaurus. A&A, **262**, 258–270. 15

de Vaucouleurs, G. (1959). Classification and Morphology of External Galaxies. *Handbuch der Physik*, **53**, 275. 2

Dressler, A. (1980). Galaxy morphology in rich clusters - Implications for the formation and evolution of galaxies. ApJ, **236**, 351–365. 3

Durisen, R.H., Boss, A.P., Mayer, L., Nelson, A.F., Quinn, T. & Rice, W.K.M. (2007). Gravitational Instabilities in Gaseous Protoplanetary Disks and Implications for Giant Planet Formation. *Protostars and Planets V*, 607–622. 11

Ebeling, H., Stephenson, L.N. & Edge, A.C. (2014). Jellyfish: Evidence of Extreme Ram-pressure Stripping in Massive Galaxy Clusters. ApJL, **781**, L40. 66

Fairweather, M. & Ranson, K. (2006). Prediction of underexpanded jets using compressibility-corrected, two-equation turbulence models. *Progress in computational fluid dynamics*, **6**, 122–128. 43

Falle, S.A.E.G. (1994). The Effect of Turbulence on the Largescale Structure of Radio Jets. MNRAS, **269**, 607. 25, 26

Fryxell, B., Olson, K., Ricker, P., Timmes, F.X., Zingale, M., Lamb, D.Q., MacNeice, P., Rosner, R., Truran, J.W. & Tufo, H. (2000). FLASH: An Adaptive Mesh Hydrodynamics Code for Modeling Astrophysical Thermonuclear Flashes. ApJS, **131**, 273–334. 40

Garcia, P.J.V. (2011). *Physical Processes in Circumstellar Disks around Young Stars*. University of Chicago Press. 11, 15

Gauthier, S. & Bonnet, M. (1990). A k-ϵ model for turbulent mixing in shock-tube flows induced by Rayleigh-Taylor instability. *Physics of Fluids*, **2**, 1685–1694. 80

Gómez, P.L., Nichol, R.C., Miller, C.J., Balogh, M.L., Goto, T., Zabludoff, A.I., Romer, A.K., Bernardi, M., Sheth, R., Hopkins, A.M., Castander, F.J., Connolly, A.J., Schneider, D.P., Brinkmann, J., Lamb, D.Q., SubbaRao, M. & York, D.G. (2003). Galaxy Star Formation as a Function of Environment in the Early Data Release of the Sloan Digital Sky Survey. ApJ, **584**, 210–227. 3, 5, 65

Goodson, M.D., Luebbers, I., Heitsch, F. & Frazer, C.C. (2016). Chemical enrichment of the pre-solar cloud by supernova dust grains. MNRAS, **462**, 2777–2791. 18

Gorman, J.M., Sparrow, E.M., Abraham, J.P. & Minkowycz, W.J. (2016). Evaluation of the efficacy of turbulence models for swirling flows and the effect of turbulence intensity on heat transfer. *Numerical Heat Transfer Part B - Fundamentals*, **70**, 485–502. 84

Goswami, J.N., Marhas, K.K., Chaussidon, M., Gounelle, M. & Meyer, B.S. (2005). Origin of Short-lived Radionuclides in the Early Solar System. In A.N. Krot, E.R.D. Scott & B. Reipurth, eds., *Chondrites and the Protoplanetary Disk*, vol. 341 of *Astronomical Society of the Pacific Conference Series*, 485. 88

Goto, T., Yamauchi, C., Fujita, Y., Okamura, S., Sekiguchi, M., Smail, I., Bernardi, M. & Gomez, P.L. (2003). The morphology-density relation in the Sloan Digital Sky Survey. MNRAS, **346**, 601–614. 3, 4, 65

Gounelle, M., Shu, F.H., Shang, H., Glassgold, A.E., Rehm, K.E. & Lee, T. (2006). The Irradiation Origin of Beryllium Radioisotopes and Other Short-lived Radionuclides. ApJ, **640**, 1163–1170. 16

Gressel, O., Nelson, R.P., Turner, N.J. & Ziegler, U. (2013). Global Hydromagnetic Simulations of a Planet Embedded in a Dead Zone: Gap Opening, Gas Accretion, and Formation of a Protoplanetary Jet. ApJ, **779**, 59. 92

Guillot, T. & Hueso, R. (2006). The composition of Jupiter: sign of a (relatively) late formation in a chemically evolved protosolar disc. MNRAS, **367**, L47–L51. 11

Gunn, J.E. & Gott, J.R., III (1972). On the Infall of Matter Into Clusters of Galaxies and Some Effects on Their Evolution. ApJ, **176**, 1. 4, 9, 50, 65, 122, 123

Hahn, O., Teyssier, R. & Carollo, C.M. (2010). The large-scale orientations of disc galaxies. MNRAS, **405**, 274–290. 96

Hanjalic, K. (1994). Advanced Turbulence Closure Models - A View Of Current Status And Future-Prospects. *International Journal Of Heat And Fluid Flow*, **15**, 178–203. 25

Hartmann, L., Calvet, N., Gullbring, E. & D'Alessio, P. (1998). Accretion and the Evolution of T Tauri Disks. ApJ, **495**, 385–400. 11

Hartquist, T.W., Dyson, J.E., Pettini, M. & Smith, L.J. (1986). Mass-loaded astronomical flows. I - General principles and their application to RCW 58. MNRAS, **221**, 715–726. 113

Haynes, M.P., Giovanelli, R. & Chincarini, G.L. (1984). The Influence of Envirionment on the H I Content of Galaxies. ARA&A, **22**, 445–470. 2

Henney, W.J. & Arthur, S.J. (1997). Two-Wind Interaction Models of the Proplyds in the Orion Nebula. In B. Reipurth & C. Bertout, eds., *Herbig-Haro Flows and the Birth of Stars*, vol. 182 of *IAU Symposium*, 561–570. 14, 87, 114

Henney, W.J. & O'Dell, C.R. (1999). A Keck High-Resolution Spectroscopic Study of the Orion Nebula Proplyds. ApJ, **118**, 2350–2368. 14

Hernández, J., Hartmann, L., Megeath, T., Gutermuth, R., Muzerolle, J., Calvet, N., Vivas, A.K., Briceño, C., Allen, L., Stauffer, J., Young, E. & Fazio, G. (2007). A Spitzer Space Telescope Study of Disks in the Young σ Orionis Cluster. ApJ, **662**, 1067–1081. 10

Hernquist, L. (1993). N-body realizations of compound galaxies. ApJS, **86**, 389–400. 75

Hester, J.J. & Desch, S.J. (2005). Understanding Our Origins: Star Formation in HII Region Environments. In A.N. Krot, E.R.D. Scott & B. Reipurth, eds., *Chondrites and the Protoplanetary Disk*, vol. 341 of *Astronomical Society of the Pacific Conference Series*, 107. 15

Hillenbrand, L.A. & Hartmann, L.W. (1998). A Preliminary Study of the Orion Nebula Cluster Structure and Dynamics. ApJ, **492**, 540–553. 13, 87

Hillenbrand, L.A., Strom, S.E., Calvet, N., Merrill, K.M., Gatley, I., Makidon, R.B., Meyer, M.R. & Skrutskie, M.F. (1998). Circumstellar Disks in the Orion Nebula Cluster. ApJ, **116**, 1816–1841. 15

Hollenbach, D.J., Yorke, H.W. & Johnstone, D. (2000). Disk Dispersal around Young Stars. *Protostars and Planets IV*, 401. 12

Holmberg, E. (1958). A photographic photometry of extragalactic nebulae. *Meddelanden fran Lunds Astronomiska Observatorium Serie II*, **136**, 1. 2

Hopkins, P.F. (2015). A new class of accurate, mesh-free hydrodynamic simulation methods. MNRAS, **450**, 53–110. 96

Hubble, E.P. (1926). Extragalactic nebulae. ApJ, **64**. 2

Hubble, E.P. (1936). Astronomy. (Scientific Books: The Realm of the Nebulae; Theoretical Astrophysics). *Science*, **84**, 509–510. 2

Jáchym, P., Köppen, J., Palouš, J. & Combes, F. (2009). Ram pressure stripping of tilted galaxies. A&A, **500**, 693–703. 8, 111, 112

Jáchym, P., Combes, F., Cortese, L., Sun, M. & Kenney, J.D.P. (2014). Abundant Molecular Gas and Inefficient Star Formation in Intracluster Regions: Ram Pressure Stripped Tail of the Norma Galaxy ESO137-001. ApJ, **792**, 11. 65

Jacobsen, S.B. (2005). The Birth of the Solar System in a Molecular Cloud: Evidence from the Isotopic Pattern of Short-lived Nuclides in the Early Solar System. In A.N. Krot, E.R.D. Scott & B. Reipurth, eds., *Chondrites and the Protoplanetary Disk*, vol. 341 of *Astronomical Society of the Pacific Conference Series*, 548. 16

Johnstone, D., Hollenbach, D. & Bally, J. (1998). Photoevaporation of Disks and Clumps by Nearby Massive Stars: Application to Disk Destruction in the Orion Nebula. ApJ, **499**, 758–776. 18

Lada, C.J. & Lada, E.A. (2003). Embedded Clusters in Molecular Clouds. ARA&A, **41**, 57–115. 15

Lambrechts, M. & Johansen, A. (2012). Rapid growth of gas-giant cores by pebble accretion. A&A, **544**, A32. 11

Launder, B.E. & Sharma, B.I. (1974). Application of the energy-dissipation model of turbulence to the calculation of flow near a spinning disc. *Letters Heat Mass Transfer*, **1**, 131–137. 25

Lecoanet, D., McCourt, M., Quataert, E., Burns, K.J., Vasil, G.M., Oishi, J.S., Brown, B.P., Stone, J.M. & O'Leary, R.M. (2016). A validated non-linear Kelvin-Helmholtz benchmark for numerical hydrodynamics. MNRAS, **455**, 4274–4288. 20

Lee, B., Giavalisco, M., Williams, C.C., Guo, Y., Lotz, J., Van der Wel, A., Ferguson, H.C., Faber, S.M., Koekemoer, A., Grogin, N., Kocevski, D., Conselice, C.J., Wuyts, S., Dekel, A., Kartaltepe, J. & Bell, E.F. (2013). CANDELS: The Correlation between Galaxy Morphology and Star Formation Activity at z ˜ 2. ApJ, **774**, 47. 3

Lee, T., Shu, F.H., Shang, H., Glassgold, A.E. & Rehm, K.E. (1998). Protostellar Cosmic Rays and Extinct Radioactivities in Meteorites. ApJ, **506**, 898–912. 16

Li, S., Frank, A. & Blackman, E.G. (2014). Triggered star formation and its consequences. MNRAS, **444**, 2884–2892. 18, 111

Lissauer, J.J. (1987). Timescales for planetary accretion and the structure of the protoplanetary disk. Icarus, **69**, 249–265. 12

Lissauer, J.J. (1993). Planet formation. ARA&A, **31**, 129–174. 12

Lissauer, J.J. & Stevenson, D.J. (2007). Formation of Giant Planets. *Protostars and Planets V*, 591–606. 11

Looney, L.W., Tobin, J.J. & Fields, B.D. (2006). Radioactive Probes of the Supernova-contaminated Solar Nebula: Evidence that the Sun Was Born in a Cluster. ApJ, **652**, 1755–1762. 16, 88

Martizzi, D., Hahn, O., Wu, H.Y., Evrard, A.E., Teyssier, R. & Wechsler, R.H. (2016). RHAPSODY-G simulations - II. Baryonic growth and metal enrichment in massive galaxy clusters. MNRAS, **459**, 4408–4427. 124

Matzner, C.D. & McKee, C.F. (1999). The Expulsion of Stellar Envelopes in Core-Collapse Supernovae. ApJ, **510**, 379–403. 90

Mayer, L., Moore, B., Quinn, T., Governato, F. & Stadel, J. (2002). Tidal debris of dwarf spheroidals as a probe of structure formation models. MNRAS, **336**, 119–130. 8

Mayer, L., Mastropietro, C., Wadsley, J., Stadel, J. & Moore, B. (2006). Simultaneous ram pressure and tidal stripping; how dwarf spheroidals lost their gas. MNRAS, **369**, 1021–1038. 8

McCarthy, I.G., Bower, R.G., Balogh, M.L., Voit, G.M., Pearce, F.R., Theuns, T., Babul, A., Lacey, C.G. & Frenk, C.S. (2007). Modelling shock heating in cluster mergers - I. Moving beyond the spherical accretion model. MNRAS, **376**, 497–522. 46

McCarthy, I.G., Frenk, C.S., Font, A.S., Lacey, C.G., Bower, R.G., Mitchell, N.L., Balogh, M.L. & Theuns, T. (2008). Ram pressure stripping the hot gaseous haloes of galaxies in groups and clusters. MNRAS, **383**, 593–605. 9, 46, 50, 61, 62

McCaughrean, M.J. (2001). High spatial resolution multiwavelength observations of star and planet formation. In R.T. Schilizzi, ed., *Galaxies and their Constituents at the Highest Angular Resolutions*, vol. 205 of *IAU Symposium*, 236. 14

McCaughrean, M.J. & O'dell, C.R. (1996). Direct Imaging of Circumstellar Disks in the Orion Nebula. ApJ, **111**, 1977. 13, 87

Melnick, J. & Sargent, W.L.W. (1977). The radial distribution of morphological types of galaxies in X-ray clusters. ApJ, **215**, 401–407. 3

Menter, F.R. (1994). Two-equation eddy-viscosity turbulence models for engineering applications. *AIAA Journal*, **32**, 1598–1605. 84

Mignone, A., Bodo, G., Massaglia, S., Matsakos, T., Tesileanu, O., Zanni, C. & Ferrari, A. (2007). PLUTO: A Numerical Code for Computational Astrophysics. ApJS, **170**, 228–242. 40

Mignone, A., Zanni, C., Tzeferacos, P., van Straalen, B., Colella, P. & Bodo, G. (2012). The PLUTO Code for Adaptive Mesh Computations in Astrophysical Fluid Dynamics. ApJS, **198**, 7. 40

Miyamoto, M. & Nagai, R. (1975). Three-dimensional models for the distribution of mass in galaxies. PASJ, **27**, 533–543. 74

Mori, M. & Burkert, A. (2000). Gas Stripping of Dwarf Galaxies in Clusters of Galaxies. ApJ, **538**, 559–568. 8, 74

Navarro, J.F., Frenk, C.S. & White, S.D.M. (1996). The Structure of Cold Dark Matter Halos. ApJ, **462**, 563. 46, 73

Nulsen, P.E.J. (1982). Transport processes and the stripping of cluster galaxies. MNRAS, **198**, 1007–1016. 50, 113

O'dell, C.R. & Wen, Z. (1994). Postrefurbishment mission Hubble Space Telescope images of the core of the Orion Nebula: Proplyds, Herbig-Haro objects, and measurements of a circumstellar disk. ApJ, **436**, 194–202. 14

O'dell, C.R., Wen, Z. & Hu, X. (1993). Discovery of new objects in the Orion nebula on HST images - Shocks, compact sources, and protoplanetary disks. ApJ, **410**, 696–700. 13, 87

Ouellette, N., Desch, S.J., Hester, J.J. & Leshin, L.A. (2005). A Nearby Supernova Injected Short-lived Radionuclides into Our Protoplanetary Disk. In A.N. Krot, E.R.D. Scott & B. Reipurth, eds., *Chondrites and the Protoplanetary Disk*, vol. 341 of *Astronomical Society of the Pacific Conference Series*, 527. xvii, 88, 89, 94, 111, 117

Ouellette, N., Desch, S.J. & Hester, J.J. (2007). Interaction of Supernova Ejecta with Nearby Protoplanetary Disks. ApJ, **662**, 1268–1281. 17, 18, 88, 90, 91, 93, 116

Ouellette, N., Desch, S.J. & Hester, J.J. (2010). Injection of Supernova Dust in Nearby Protoplanetary Disks. ApJ, **711**, 597–612. 17

Pan, L., Desch, S.J., Scannapieco, E. & Timmes, F.X. (2012). Mixing of Clumpy Supernova Ejecta into Molecular Clouds. ApJ, **756**, 102. 17

Paolillo, M., Fabbiano, G., Peres, G. & Kim, D.W. (2002). Deep ROSAT HRI Observations of the NGC 1399/NGC 1404 Region: Morphology and Structure of the X-Ray Halo. ApJ, **565**, 883–907. 66

Papamoschou, D. & Bunyajitradulya, A. (1997). Evolution of large eddies in compressible shear layers. *Physics of Fluids*, **9**, 756–765. 60

Papamoschou, D. & Roshko, A. (1988). The compressible turbulent shear layer - An experimental study. *Journal of Fluid Mechanics*, **197**, 453–477. 51, 52

Pittard, J.M., Falle, S.A.E.G., Hartquist, T.W. & Dyson, J.E. (2009). The turbulent destruction of clouds - I. A k-ϵ treatment of turbulence in 2D models of adiabatic shock-cloud interactions. MNRAS, **394**, 1351–1378. 25, 60, 125

Pittard, J.M., Hartquist, T.W. & Falle, S.A.E.G. (2010). The turbulent destruction of clouds - II. Mach number dependence, mass-loss rates and tail formation. MNRAS, **405**, 821–838. 25

Pope, S.B. (2000). *Turbulent flows*. Oxford University Press. 25, 84

Quitté, G., Latkoczy, C., Halliday, A.N., Schönbächler, M. & Günther, D. (2005). Iron-60 in the Eucrite Parent Body and the Initial 60Fe/56Fe of the Solar System. In S. Mackwell & E. Stansbery, eds., *36th Annual Lunar and Planetary Science Conference*, vol. 36 of *Lunar and Planetary Science Conference*. 16

Ricci, L., Testi, L., Natta, A., Scholz, A., de Gregorio-Monsalvo, I. & Isella, A. (2014). Brown Dwarf Disks with ALMA. ApJ, **791**, 20. 9

Richert, A.J.W., Feigelson, E.D., Getman, K.V. & Kuhn, M.A. (2015). No Evidence for Protoplanetary Disk Destruction By OB Stars in the MYStIX Sample. ApJ, **811**, 10. 15

Richling, S. & Yorke, H.W. (1997). Photoevaporation of protostellar disks. II. The importance of UV dust properties and ionizing flux. A&A, **327**, 317–324. 13

Richling, S. & Yorke, H.W. (2000). Photoevaporation of Protostellar Disks. V. Circumstellar Disks under the Influence of Both Extreme-Ultraviolet and Far-Ultraviolet Radiation. ApJ, **539**, 258–272. 114

Roberts, M.S. & Haynes, M.P. (1994). Physical Parameters along the Hubble Sequence. ARA&A, **32**, 115–152. 3

Roediger, E. (2009). Ram pressure stripping of disk galaxies in galaxy clusters. *Astronomische Nachrichten*, **330**, 888. 65

Roediger, E. & Brüggen, M. (2006). Ram pressure stripping of disc galaxies: the role of the inclination angle. MNRAS, **369**, 567–580. 8, 69, 73, 98, 111, 112

Roediger, E. & Brüggen, M. (2007). Ram pressure stripping of disc galaxies orbiting in clusters - I. Mass and radius of the remaining gas disc. MNRAS, **380**, 1399–1408. 112

Scally, A. & Clarke, C. (2001). Destruction of protoplanetary discs in the Orion Nebula Cluster. MNRAS, **325**, 449–456. 13, 14

Scannapieco, E. & Brüggen, M. (2008). Subgrid Modeling of AGN-driven Turbulence in Galaxy Clusters. ApJ, **686**, 927–947. 25

Scannapieco, E. & Brüggen, M. (2010). Simulating supersonic turbulence in galaxy outflows. MNRAS, **405**, 1634–1653. 80, 81, 82, 85

Schmidt, W. & Federrath, C. (2011). A fluid-dynamical subgrid scale model for highly compressible astrophysical turbulence. A&A, **528**, A106. 25

Shih, T., Liou, W., Shabbir, A., Yang, Z. & Zhu, J. (1995). A new k-lunate eddy viscosity model for high reynolds number turbulent flows. *Computers and Fluids*, **24**, 227–238. 84

Shin, M.S. & Ruszkowski, M. (2013). Ram pressure stripping in elliptical galaxies - I. The impact of the interstellar medium turbulence. MNRAS, **428**, 804–814. 9, 49, 62

Slessor, M.D., Zhuang, M. & Dimotakis, P.E. (2000). Turbulent shear-layer mixing: growth-rate compressibility scaling. *Journal of Fluid Mechanics*, **414**, 35–45. 52

Soteriou, M.C. & Ghoniem, A.F. (1995). Effects of the free-stream density ratio on free and forced spatially developing shear layers. *Physics of Fluids*, **7**, 2036–2051. 51

Spitzer, L. (1956). *Physics of fully ionized gases*. Interscience Publishers. 42

Stapelfeldt, K., Sahai, R., Werner, M. & Trauger, J. (1997). An HST Imaging Search for Circumstellar Matter in Young Nebulous Clusters. In D. Soderblom, ed., *Planets Beyond the Solar System and the Next Generation of Space Missions*, vol. 119 of *Astronomical Society of the Pacific Conference Series*, 131. 15

Steinhauser, D., Schindler, S. & Springel, V. (2016). Simulations of ram-pressure stripping in galaxy-cluster interactions. A&A, **591**, A51. 124

Stone, J.M., Gardiner, T.A., Teuben, P., Hawley, J.F. & Simon, J.B. (2008). Athena: A New Code for Astrophysical MHD. ApJS, **178**, 137–177. 40

Störzer, H. & Hollenbach, D. (1999). Photodissociation Region Models of Photoevaporating Circumstellar Disks and Application to the Proplyds in Orion. ApJ, **515**, 669–684. 114

Tachibana, S., Huss, G.R., Kita, N.T., Shimoda, G. & Morishita, Y. (2006). ^{60}Fe in Chondrites: Debris from a Nearby Supernova in the Early Solar System? ApJL, **639**, L87–L90. 16, 88

Takeuchi, T., Miyama, S.M. & Lin, D.N.C. (1996). Gap Formation in Protoplanetary Disks. ApJ, **460**, 832. 113

Teyssier, R. (2002). Cosmological hydrodynamics with adaptive mesh refinement. A new high resolution code called RAMSES. A&A, **385**, 337–364. 40

Tonnesen, S. & Bryan, G.L. (2009). Gas Stripping in Simulated Galaxies with a Multiphase Interstellar Medium. ApJ, **694**, 789–804. 8, 113

Toro, E.F. (2009). *Riemann Solvers and Numerical Methods for Fluid Dynamics*. Springer, 3rd edn. 29

Vollmer, B., Wong, O.I., Braine, J., Chung, A. & Kenney, J.D.P. (2012). The influence of the cluster environment on the star formation efficiency of 12 Virgo spiral galaxies. A&A, **543**, A33. 65

Wang, K.S., van der Tak, F.F.S. & Hogerheijde, M.R. (2012). Kinematics of the inner thousand AU region around the young massive star AFGL 2591-VLA3: a massive disk candidate? A&A, **543**, A22. 9

Wilcox, D.C. (2006). *Turbulence Modeling for CFD*. DCW Industries. 25, 47, 75, 84

Williams, J.P. & Cieza, L.A. (2011). Protoplanetary Disks and Their Evolution. ARA&A, **49**, 67–117. 11

Woosley, S.E. & Weaver, T.A. (1995). The Evolution and Explosion of Massive Stars. II. Explosive Hydrodynamics and Nucleosynthesis. ApJS, **101**, 181. 16, 116

Yakhot, V. & Orszag, S.A. (1986). Renormalization group analysis of turbulence. i. basic theory. *Journal of Scientific Computing*, **1**, 3–51. 84

Yamaleev, N.K. & Carpenter, M.H. (2009). Third-order Energy Stable WENO scheme. *Journal Of Computational Physics*, **228**, 3025–3047. 40